



**Politecnico
di Torino**

Politecnico di Torino

Master of Science in Environmental and Land Engineering

A.y. 2023/2024

Graduation Session July 2024

Seismic response analysis of unstable rock masses through passive seismic monitoring and numerical modeling at laboratory and field scales

Supervisors:

Daniele Martinelli
Chiara Colombero

Candidate:

Cecilia Francardo

CONTENTS

1	INTRODUCTION.....	1
1.1	Overview of rockfall phenomena.....	1
1.2	<i>THEROCKLAB</i> PRIN initiative.....	2
2	THEORETICAL FRAMEWORK.....	6
2.1	Integrated rock mass monitoring.....	6
2.2	Eigenfrequency as a monitoring seismic parameter.....	9
2.3	Cross-correlation of ambient seismic noise.....	12
2.4	Driving mechanisms for rock mass resonant behavior	14
2.4.1	Fracture effect	15
2.4.2	Surface effect	15
2.4.3	Bulk effect	16
2.4.4	Water effect.....	17
2.4.5	Ice effect	18
2.4.6	Clay effect	18
2.5	Fundamentals of the finite element method (FEM)	19
2.5.1	Element discretization.....	19
2.5.2	Primary variable approximation.....	21
2.5.3	Element and global equations.....	22
2.5.4	Boundary conditions	22
2.5.5	Solving the global equations	23

2.5.6	Adopted FEM software tools	24
3	LABORATORY SCALE ACTIVITY	26
3.1	Geomechanical characterization of specimens	29
3.1.1	Principles of ultrasonic pulse velocity (UPV) testing.....	29
3.1.2	Procedures for UPV testing	30
3.1.3	Results of UPV testing	31
3.1.4	Calculation of elastic parameters	35
3.2	FEM eigenfrequency analysis at the laboratory scale	37
3.3	H/V spectral ratio simulation at the laboratory scale	45
3.4	Three-component (3C) seismic recordings at the laboratory scale	50
3.4.1	Description of the lab 3C seismic tests.....	50
3.4.2	Results of the lab 3C seismic tests	57
3.4.3	Insights and implications from the lab 3C seismic tests.....	67
3.5	Designing future specimens using FEM simulation	69
3.5.1	Objectives of the design process.....	69
3.5.2	Simulation results	73
4	FIELD SCALE ACTIVITY	84
4.1	The Acuto field laboratory.....	84
4.2	Analysis of the monitoring results.....	88
4.3	FEM eigenfrequency analysis at the AcutoFieldLab	104
5	CONCLUSION	107
6	LIST OF REFERENCES	112

LIST OF FIGURES

Figure 1.1 Locations of the natural field laboratories selected in the <i>THEROCKLAB</i> PRIN project.	5
Figure 2.1 Typical 2D finite elements (Potts and Zdravković 1999).	21
Figure 3.1 3D model of Specimen A generated using photogrammetric techniques. Units in meters.	28
Figure 3.2 3D model of Specimen B generated using photogrammetric techniques. Units in meters.	28
Figure 3.3 Determination of P-wave first arrival time for Specimen A.....	32
Figure 3.4 Determination of S-wave polarization inversion time for Specimen A.....	33
Figure 3.5 Determination of P-wave first arrival time for Specimen B.....	34
Figure 3.6 Determination of S-wave polarization inversion time for Specimen B. ...	35
Figure 3.7 First eigenmode displacement visualization in COMSOL Multiphysics for Specimen A.....	39
Figure 3.8 Second eigenmode displacement visualization in COMSOL Multiphysics for Specimen A.	40
Figure 3.9 Third eigenmode displacement visualization in COMSOL Multiphysics for Specimen A.....	40
Figure 3.10 First eigenmode displacement visualization in COMSOL Multiphysics for Specimen B.....	41
Figure 3.11 Second eigenmode displacement visualization in COMSOL Multiphysics for Specimen B.	41
Figure 3.12 Third eigenmode displacement visualization in COMSOL Multiphysics for Specimen B.....	42
Figure 3.13 First eigenmode displacement visualization in GTS NX for Specimen A.	42

Figure 3.14 Second eigenmode displacement visualization in GTS NX for Specimen A.	43
Figure 3.15 Third eigenmode displacement visualization in GTS NX for Specimen A.	43
Figure 3.16 First eigenmode displacement visualization in GTS NX for Specimen B.	44
Figure 3.17 Second eigenmode displacement visualization in GTS NX for Specimen B.	44
Figure 3.18 Third eigenmode displacement visualization in GTS NX for Specimen B.	45
Figure 3.19 Base acceleration inputs (X, Y, Z) for H/V simulation.	46
Figure 3.20 Frequency spectrum of base acceleration inputs (X, Y, Z) for H/V simulation.	47
Figure 3.21 H/V simulation for Specimen A obtained with COMSOL Multiphysics. .	48
Figure 3.22 H/V simulation for Specimen B obtained with COMSOL Multiphysics. .	49
Figure 3.23 Example of laboratory setup for 3C seismic recording tests.	52
Figure 3.24 H/V plot – Test 56.	58
Figure 3.25 H/V plot – Test 58.	59
Figure 3.26 H/V plot – Test 21.	60
Figure 3.27 Amplitude spectrum – Test 21.	61
Figure 3.28 Amplitude spectrum – Test 21 – zoom around 2000 Hz.	62
Figure 3.29 Amplitude spectrum – Test 21 – zoom around 4200 Hz.	63
Figure 3.30 Amplitude spectrum – Test 58 – zoom around 1965 Hz.	64
Figure 3.31 Amplitude spectrum – Test 49 – zoom around 1935 Hz.	65
Figure 3.32 Amplitude spectrum – Test 60 – zoom around 1965 Hz.	66
Figure 3.33 Amplitude spectrum – Test 66 – zoom around 2010 Hz.	67
Figure 3.34 Cut configurations for Specimen C and Specimen D.	71
Figure 3.35 Representation of Constraint Mode 1 and Constraint Mode 2.	72

Figure 3.36 f_1 value variations with cut length for Specimen C and Specimen D – Constraint Mode 1.	75
Figure 3.37 f_1 value variations with cut length for Specimen C and Specimen D – Constraint Mode 2.	76
Figure 3.38 Location of the three points considered to perform the H/V simulation with COMSOL Multiphysics for Specimen C4.	79
Figure 3.39 Eigenmode displacement visualization for Specimen C4.	80
Figure 3.40 H/V simulation for Specimen C4 (stable sector) obtained with COMSOL Multiphysics.	81
Figure 3.41 H/V simulation for Specimen C4 (unstable sector, midpoint) obtained with COMSOL Multiphysics.	82
Figure 3.42 H/V simulation for Specimen C4 (unstable sector, edge) obtained with COMSOL Multiphysics.	83
Figure 4.1 AcutoFieldLab geographic location.	85
Figure 4.2 AcutoFieldLab 3D point cloud and accelerometers' locations.	87
Figure 4.3 Station TUF10 – Power Spectral Density (PSD) curves for component E, N, and V.	89
Figure 4.4 Station TUF10 – Spectrograms (E, N, V).	90
Figure 4.5 Station TUF10 – Spectrograms (E, N, V) zoomed 55-95 Hz.	91
Figure 4.6 Station TUF10 – Spectrogram E zoomed 55-95 Hz and rock temperature/microstrain time series.	92
Figure 4.7 Station TUF10 – H/V spectrogram zoomed 60-90 Hz.	93
Figure 4.8 Polar plot and azimuth analysis for TUF10.	94
Figure 4.9 Station PRT10 – Power Spectral Density (PSD) curves for component E, N, and V.	95
Figure 4.10 Station PRT10 – Spectrograms (E, N, V).	96
Figure 4.11 Station PRT10 – Spectrograms (E, N, V) zoomed 55-95 Hz.	96
Figure 4.12 Station PRT10 – Spectrograms (E, N, V) zoomed 0-20 Hz.	97

Figure 4.13 Station PRT10 – Spectrogram E zoomed 10-15 Hz and rock temperature/microstrain time series.....	98
Figure 4.14 Station TUF10 – H/V spectrogram zoomed 60-90 Hz.	99
Figure 4.15 Polar plot and azimuth analysis for PRT10.	100
Figure 4.16 Cross-correlogram between PRT10 and TUF10 – 18-20 Hz window....	101
Figure 4.17 Rock temperature and microstrain time series, relative velocity change, and cross-correlation values between PRT10 and TUF10.	102
Figure 4.18 Rock temperature and microstrain time series, relative velocity change, and cross-correlation values between PRT10 and TUF10 (zoom 13/07/2022 to 18/07/2022).....	103
Figure 4.19 Overlap of rock temperature time series and relative velocity change values (zoom 13/07/2023 to 18/07/2023).....	103
Figure 4.20 Eigenfrequency analysis result for the entire rock wall.....	105
Figure 4.21 Eigenfrequency analysis result for the unstable block only.	106

LIST OF TABLES

Table 3.1 Dimensions of Specimen A and Specimen B.....	27
Table 3.2 Photogrammetric 3D model details for Specimen A and Specimen B.....	27
Table 3.3 Technical specifications of the Pundit Lab device for UPV testing.	30
Table 3.4 Pundit Lab configuration settings for UPV testing.	31
Table 3.5 Configuration settings for the <i>Data Logging</i> acquisition mode.	31
Table 3.6 UPV testing results for Specimen A and Specimen B.....	35
Table 3.7 Geomechanical characterization results for Specimen A and Specimen B.	36
Table 3.8 Eigenmode Analysis Comparison: GTS NX vs. COMSOL Multiphysics for Specimen A.....	38
Table 3.9 Eigenmode Analysis Comparison: GTS NX vs. COMSOL Multiphysics for Specimen B.....	38
Table 3.10 L_{max} , sampling frequency and Nyquist frequency for H/V simulation for Specimen A and Specimen B.	47
Table 3.11 Technical specifications of the Triaxial ICP Accelerometer.	50
Table 3.12 Summary of 3C seismic recordings.	53
Table 3.13 Dimensions of Specimen C and Specimen D.	70
Table 3.14 Cut lengths (in cm) for eigenfrequency simulations of Specimen C and Specimen D.....	71
Table 3.15 Eigenfrequency simulation results (Constraint Mode 1) for Specimen C and D using GTS NX.	73
Table 3.16 Eigenfrequency simulation results (Constraint Mode 2) for Specimen C and D using GTS NX.	73
Table 3.17 Percent error in eigenfrequency values between Specimen C and D as function of the cut length – Constraint Mode 1.	74

Table 3.18 Percent error in eigenfrequency values between Specimen C and D as function of the cut length – Constraint Mode 2.	75
Table 3.19 Percent error in eigenfrequency between GTS NX and COMSOL Multiphysics for Specimen C4.	78
Table 4.1 Technical specifications of the installed monitoring devices.....	86
Table 4.2 Characteristics of the installed accelerometers.....	87

ABSTRACT

The development of effective monitoring and early warning strategies for rock mass failure is a crucial aspect for managing the risks associated with unstable rock masses in regions prone to geological hazards, particularly in the context of climate change. The integration of multi-sensor monitoring systems with numerical modeling has the potential to investigate the rock mass behavior and the influence of external physical drivers (such as temperature and precipitation). Passive seismic techniques are distinguished by their capacity to obtain information on the internal structure of the rock mass and to effectively predict rapid rockfalls. By continuous tracking seismic parameters (resonance frequency and relative velocity change), it is possible to detect the effect of external factors, which lead to reversible variations, as well as the degradation of mechanical properties of the rock mass prior to failure, which cause a rapid irreversible variation.

The research was conducted at both laboratory and field scales, combining field monitoring, laboratory testing, and finite element (FEM) simulations. In the laboratory, triaxial seismic recordings were conducted to investigate the resonance behavior of rock samples with varying shapes. The results indicated that the detection of potential eigenfrequencies was challenging due to the minimal response of the samples and to the presence of systematic instrumental noise. The numerical simulations provided reference values which facilitated the interpretation of experimental results, confirming that the column-shaped sample exhibited a greater resonance response than the slab-shaped sample. Furthermore, FEM simulations were conducted on a variety of geometries to inform the design of jointed samples for future testing. The field data collected at the AcutoFieldLab were subjected to spectral analysis with the objective of identifying potential resonance frequencies and relative velocity changes. Although cross-correlation analysis was

deemed unsuitable as a field monitoring strategy in this particular case, a potential eigenfrequency of the unstable block was identified at approximately 75 Hz. This frequency exhibited a distinct oscillatory behavior in phase with temperature, indicating its potential as an indicator of instability and monitoring parameter.

1 INTRODUCTION

1.1 Overview of rockfall phenomena

Rockfalls are sudden events in which a mass of rock, ranging from individual boulders to large rock avalanches, detaches from steep slopes or cliffs and falls, rolls, or bounces downward. These events pose significant risks to people and infrastructure such as roads, railways, and buildings (Bajni, Camera, and Apuani 2021). In addition, they can significantly alter the behavior of high mountain catchments by generating sediments (Knoflach et al. 2021).

Predicting and managing the risk of rockfall events is extremely challenging. Rock slope instability leading to rockfall is considered a "Grand Challenge" in rock mechanics and rock engineering due to the difficulties in quantitatively describing and characterizing the rock mass in the detachment zone, as well as the uncertainties in current methods for simulating and predicting rockfall trajectories (Barla 2019).

Several factors contribute to the occurrence of rockfalls, including geomechanical aspects such as rock type, fracture patterns, and site-specific stresses, as well as meteorological conditions such as heavy rainfall, prolonged precipitation, and freeze-thaw cycles, all of which vary significantly over time and space (Bajni, Camera, and Apuani 2021). Moreover, the Alps and Apennine regions are increasingly vulnerable to such events due to natural geological processes, human activities and the accelerating effects of climate change (Bajni, Camera, and Apuani 2021; Stoffel et al. 2024).

Climate change can affect rockfall events in a variety of ways, both in the short and long term. More frequent and intense rainfall can cause slope instability by increasing water pressure in rock joints, thereby reducing shear strength (Bajni,

Camera, and Apuani 2021). Temperature fluctuations around the freezing point can trigger freeze-thaw cycles that weaken rock walls over time by progressively causing subcritical cracking and accelerating weathering (Bajni, Camera, and Apuani 2021). Rising temperatures also degrade the permafrost that stabilizes mountain slopes, leading to greater instability and more frequent rockfalls (Stoffel et al. 2024). Glacial retreat, another consequence of climate change, can further exacerbate rockfall events by exposing previously glaciated rock slopes, reducing their geotechnical and mechanical stability (Knoflach et al. 2021).

Given the complex interplay between geological, meteorological, and climatological factors that drive rockfall events and their profound impact on human safety and infrastructure, further research efforts are needed to understand these processes. Comprehensive investigations of rockfall dynamics, coupled with robust monitoring and mitigation strategies, are essential for effective risk management.

1.2 *THEROCKLAB* PRIN initiative

This thesis research project was carried out as part of a 24-month long PRIN (Progetto di Ricerca di Elevato Interesse Nazionale) initiative entitled *THERmo- and hydro-mechanical monitoring and modeling of jointed ROCKs: a national Site LABoratory network (THEROCKLAB)*, which started in October 2023. *THEROCKLAB* aims to implement various multi-sensor monitoring and modelling techniques to investigate the thermo- and hydro-mechanical processes acting on fractured rock masses as preparatory processes and triggering factors to failure, also suitable for early warning applications.

THEROCKLAB involves five unstable rock masses spread across the Alps and the Apennines, each serving as a field laboratory site strategically chosen to cover a range of geological and environmental conditions prone to failure. The data collected at these different sites will be processed and interpreted with the ultimate aim of

gaining a deeper understanding of the evolution of the mechanical properties of rock masses leading to their eventual collapse in relation with external meteorological and climatic conditions.

Four research units (POLITO, UNIBO, UNIROMA1, UNIMIB) are collaborating in the project, each contributing with its specific expertise and approach. The selected field sites (which are shown in Figure 1.1) are characterized by different altitudes, lithologies and external anthropic conditions. They are Madonna del Sasso (POLITO) on the shores of Orta Lake; San Leo (UNIBO), about 90 km from Florence; AcutoFieldLab (UNIROMA1), in the municipality of Acuto (FR); and Poggi Baldi (UNIROMA1), in the northern Apennines. In addition, *THEROCKLAB* aims to establish a new field site in the Dolomites, which is managed by UNIMIB, to specifically study the rockfall processes due to permafrost degradation. The knowledge gained from the already existing monitoring sites was used as a guide for the proper design of this new site.

The field investigations are complemented by laboratory scale activities and by finite element (FEM) numerical simulations to further evaluate the mechanical properties of the rock masses and the influence of external thermal and hydrogeological drivers on their stability over time. Cold chamber laboratory tests, such as freeze-thaw cycles on different samples, will be then used as a proxy to study how seismic and mechanical parameters evolve in relation to temperature and water saturation conditions. Numerical simulations, which will be validated and constrained using the collected field and laboratory data, will support and guide the design of new field and laboratory tests.

The core feature of the proposed *THEROCKLAB* research activity is its integrated methodology, which includes remote sensing techniques, geomechanical monitoring, meteorological monitoring and geophysical monitoring. Remote sensing techniques, including ground-based and UAV photogrammetry and thermography surveys, will be used to reconstruct the 3D geometry of the field test sites and to characterize the surface temperature distribution of the rock slopes. Geomechanical

monitoring systems include strain gauges, extensometers and crackmeters which are used to measure deformation within the rock mass. Weather parameters (such as precipitation and wind speed) and air and rock temperatures are also measured to support the analysis of the effect of external physical drivers on the rock mass stability. A key role in this multi-method approach is played by geophysical methods, in particular by continuous passive seismic monitoring, which can provide useful information on the internal processes of the rock mass. Spectral analysis and cross-correlation of the ambient seismic noise, indeed, allow for the detection of changes in two seismic parameters that characterize the unstable compartment, namely the resonance frequency and the seismic velocity, both of which are directly related to the mechanical properties of the rock mass itself. Reversible variations of these two seismic parameters are interpreted as being caused by external meteorological factors, mainly temperature, precipitation, and ice formation, whereas sudden irreversible drops not correlated to meteorological factors indicate a deterioration of the mechanical properties of the mass leading to a potential failure and collapse. The identification of irreversible drops on seismic parameters through continuous monitoring can therefore serve as an early warning method for rock mass failures.

The expected outcomes of the *THEROCKLAB* initiative include: a deeper understanding of the relationship between rock mass quality and susceptibility to damage caused by thermal and hydrogeological factors across various scales; the investigation of the evolution of mechanical and seismic parameters resulting from damage accumulation leading to failure; the establishment of standardized procedures for multi-scale characterization and monitoring of hydro- and thermo-mechanical effects on fractured rock masses; the application of innovative and multidisciplinary approaches to rock mass monitoring.

In a broader long-term perspective, *THEROCKLAB* aims to contribute to the ongoing controversial and challenging topic in the field of geoengineering and rock mechanics, namely the understanding of the dynamic response of rock masses to thermal and hydromechanical forces. This research is particularly relevant in the

context of anthropogenic influences and weather/climatic variations, especially in environments facing climate change-related hazards. In addition, it provides a methodological contribution related to the development of processing techniques for the management of integrated geophysical and mechanical monitoring data. At the national level, the project fosters collaboration among academic institutions to monitor landslide-prone areas across the country, while facilitating knowledge transfer to stakeholders interested in deploying monitoring systems for hazard prevention, civil protection, or occupational safety. It also aligns with national research programs focused on security of natural systems and adaptation to climate change, as well as broader goals to improve forecasting capabilities and mitigate the impacts of climate change. Moreover, the project has a local impact on the identified site laboratories, contributing to their understanding and management of geological hazards within their respective regions.

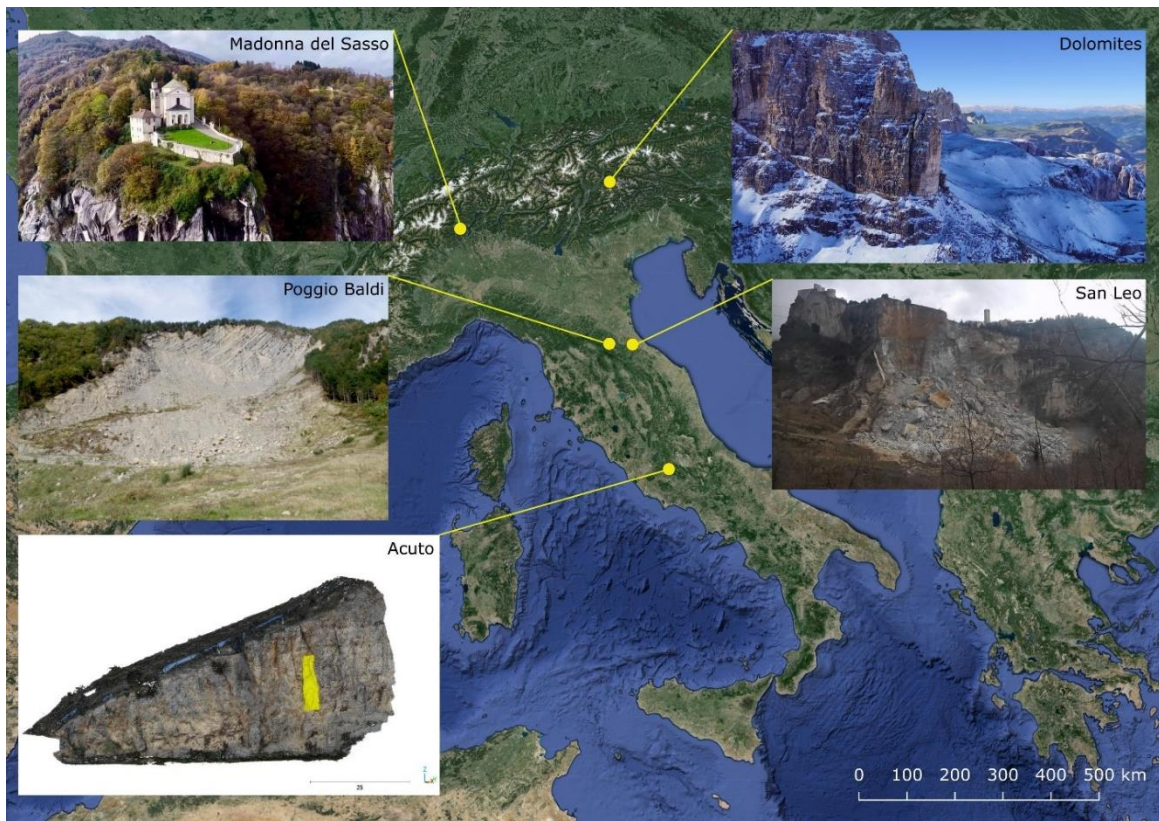


Figure 1.1 Locations of the natural field laboratories selected in the *THEROCKLAB* PRIN project.

2 THEORETICAL FRAMEWORK

2.1 Integrated rock mass monitoring

Managing the risks associated with unstable rock formations has become increasingly important, especially in regions such as Italy, which is known for its diverse geological landscape. Italy faces a significant incidence of landslides, affecting approximately 7.9% of its territory, particularly in the Alps and the Apennines (Trigila et al. 2021). Effective mitigation of potential rockfall disasters demands a comprehensive strategy, that includes the identification and characterization of vulnerable areas prone to collapse, as well as the implementation of robust monitoring systems to forecast impending failures and activate early warning alert systems (Colombero, Comina, et al. 2018).

In this perspective, it is crucial to understand the multitude of external factors that can trigger slope instability. These factors include heavy rainfall, changes in hydrogeological conditions induced by precipitation, freeze-thaw cycles, snowmelt, temperature fluctuations, seismic activity, volcanic eruptions, and human activities (Colombero, Comina, et al., 2018). Furthermore, it is worth noting that the impact of these factors varies depending on environmental conditions, with certain mechanisms exerting greater influence than others. For example, in elevated regions characterized by cold climates, such as mountainous areas, temperature variations are an important driver of rockslides and rockfalls. This phenomenon causes the alternate freezing and thawing of water in the cracks of rock mass, hastening the deterioration of the rock mass (Colombero, Comina, et al. 2018).

The behavior of potentially unstable compartments and their failure mechanisms are influenced not only by external physical factors but also by structural characteristics, including the persistence, aperture, roughness, and orientation of fractures (Colombero et al. 2021). Proper and effective survey campaigns are therefore essential for gathering comprehensive information about unstable rock masses.

To effectively characterize rock slopes, several well-established survey methods are available, each with distinct advantages and limitations. A common challenge for these methods is the acquisition of subsurface information. Classical geological and geotechnical survey techniques, such as strain gauges, extensometers, and crackmeters, are extremely useful in providing information on the structural configuration and internal deformation of the rock mass, but they can have significant limitations in terms of accessibility, cost, safety, and data quality (Lévy et al. 2010), especially in steep mountainous environments. On the other hand, terrestrial and airborne remote sensing techniques (such as photogrammetry, tacheometry, and laser scanning) offer promising solutions to these problems. They are often cost-effective and do not impose accessibility constraints, although they face strong depth limitations (Colombero et al. 2017). Remote sensing techniques are employed primarily to reconstruct the Digital Surface Model (DSM), which is helpful to obtain quantitative information on the location and orientation of joints, thereby enabling the estimation of the unstable volume and geometry potentially involved in the collapse (Lévy et al. 2010). However, the DSM still lacks valuable information on the internal structure of the rock mass. As for traditional active seismic campaigns such as cross-hole tomography, which can quantify the persistence and depth of the identified fractures, they may also be affected by limited space and accessibility (Colombero et al. 2017), as well as by limited depth of resolution due to intense scattering and velocity gradients (Burjánek et al. 2018). Ground penetrating radar (GPR) profiles on cliff faces offer superior penetration and resolution, providing geometry and continuity of large open joints. However,

deployment challenges and the applicability limitations of GPR to high resistive rock slopes restrict its use to specific surveys (Lévy et al., 2010).

A common limitation among the discussed methods is their inability to effectively predict rapid rockslides and rockfalls. Unlike other types of landslides, rockfalls often occur suddenly and without visible pre-failure signs, posing significant challenges for accurate forecasting (Colombero, Baillet, et al. 2018). Consequently, while these methods are valuable for monitoring purposes, they are less suitable for implementing effective early warning systems.

Given the challenges associated with obtaining information on the internal structures of rock slopes and identifying precursors for early warning, which are typical of other survey methods, passive seismic monitoring emerges as a standout among available geophysical techniques. Passive seismic methods offer unique potential for characterizing and monitoring internal rock mass processes.

Analysis of ambient seismic noise recordings allows the extraction of two seismic parameters: resonance frequencies and seismic velocity changes within potentially unstable compartments. This has the potential to facilitate the detection of failure precursors and potential threats to slope stability (Lévy et al. 2010). In fact, the irreversible decline of these easily monitored seismic parameters, which are directly dependent on the mechanical properties of the rock mass, signals degradation prior to failure and impending instability, thereby aiding early warning purposes (Colombero et al. 2021). Furthermore, surface crack opening, which is a typical precursor of other types of landslides, can be observed in localized areas but does not provide sufficient warning of impending rockfall, whereas resonance frequency and velocity changes are global parameters that characterize the entire unstable compartment (Lévy et al. 2010). Moreover, among the geophysical methods for rock mass characterization and monitoring, ambient noise recording is unique in allowing continuous tracking (Lévy et al. 2010).

However, besides irreversible variations, reversible fluctuations in resonance frequency and relative velocity change are also observed, mainly due to the influence

of external meteorological factors such as air temperature and precipitation. These variations highlight the sensitivity of the seismic response to environmental conditions, while suggesting the need for robust monitoring systems capable of distinguishing between reversible and irreversible changes associated with internal damage to implement effective early warning systems (Colombero et al. 2021).

In conclusion, recent endeavors to investigate and monitor fractured rock masses (Burjánek et al. 2018; Lévy et al. 2010; Colombero, Comina, et al. 2018; Colombero, Baillet, et al. 2018; Colombero et al. 2021; 2017) have demonstrated the necessity of adopting an integrated approach to effectively manage the risks posed by unstable rock formations. The integration of survey and monitoring techniques, particularly passive seismic methods, holds great promise for improving our understanding and management of unstable rock slopes, thus contributing to safer and more resilient environments. Sections 2.2 and 2.3 provide a more detailed explanation of how changes in natural frequency and wave velocity function can serve as monitoring parameters for early warning applications.

2.2 Eigenfrequency as a monitoring seismic parameter

Eigenfrequencies, or natural frequencies, are certain discrete frequencies at which a system is prone to vibrate. The *eigenmode* is the shape of the deformation that the structure undergoes when vibrating at a specific *eigenfrequency*.

Monitoring strategies using passive seismic methods leverage the principle that spectral peaks in seismic noise recorded on unstable compartments correspond to their resonance frequencies (Lévy et al. 2010; Burjánek et al. 2018; Colombero et al. 2017), which is further supported by the absence of such peaks in the noise recorded on stable rock compartments (Colombero et al. 2017; Colombero, Baillet, et al. 2018).

Unstable rock volumes can be studied in analogy with the simple oscillator described by Equation 2.1, so that its resonance frequency is inversely proportional to its mass M and directly proportional to the stiffness K of the unstable volume and of the rock bridges between the stable and unstable compartments (Colombero, Baillet, et al. 2018).

$$f_r = \frac{1}{2\pi} \sqrt{\frac{K}{M}} \quad \text{Eq. 2.1}$$

The K parameter as a whole describes the mechanical properties of the prone-to-fall compartment, including the internal stiffness K_b of the unstable compartment described by the Young modulus of the bulk material E_b , and the contact stiffness K_c of the rock bridges between the stable and the unstable compartments (Colombero et al. 2021). K_c is usually challenging to quantify, as it depends on multiple properties of the fracture, such as depth, width, roughness, and filling material (Colombero et al. 2021).

Resonance frequency values are usually derived from the peaks in the power spectral density (PSD) of continuous noise recordings. The PSD represents the proportion of the total signal power contributed by each frequency component of the signal and it is simply derived from the continuous record by averaging the intensity of the fast Fourier transform (FFT) of the record (Larose et al. 2015):

$$PSD(f) = |FFT(\varphi_A(t))|^2 \quad \text{Eq. 2.2}$$

The calculation of spectral ratios both single-station (e.g. H/V method) or site-reference (i.e. between the same component of two different stations, e.g. V/V, E/E, N/N or H/H) is typically performed to enhance the spectral peaks (Burjánek et al. 2018; Colombero et al. 2021).

Another important analysis that can be performed on ambient seismic noise is to examine the 3D spatial directivity of spectral peaks and their long-term temporal variations, as described by Colombero et al. (2017). This involves calculating the frequency distribution (radial axis) and associated azimuth (polar angle) of the vibration energy in the horizontal plane from the N and E spectra of each station. The results are presented in a polar plot, where the radial axis represents the frequency value and the polar angle, measured clockwise from the north, represents the associated azimuth. By combining the horizontal spectrum along the direction of each frequency peak (typically f_1 , f_2 , and f_3) with the vertical component spectrum, the three-dimensional orientation of the first three eigenmodes at each station can be determined. It is observed that clear peaks emerge at specific orientations and frequencies, while stable compartments exhibit null or less significant peaks in amplitude and directionality (Colombero et al. 2017). This suggests that eigenfrequencies and eigenmodes can be employed to effectively monitor and track the behavior of unstable rock compartments.

This three-dimensional spatial analysis of the spectral content is a valuable tool for investigating the influence of fracture configurations on vibration directions. A notable distinction exists between two-dimensional (2D) geometries, which are defined by an unstable volume separated by a single planar fracture, and more complex three-dimensional (3D) configurations. In two-dimensional cases, the vibration motion at the first resonance frequency typically has the largest spectral amplitude and is oriented perpendicular to the main fracture set, indicating bending of the rock column perpendicular to the rear fracture (Lévy et al. 2010; Valentin et al. 2017; Bottelin et al. 2013). The second and third modes frequently correspond to torsion and bending parallel to the rear fracture (Valentin et al. 2017; Lévy et al. 2010), or vice versa (Bottelin et al. 2013). Despite the potential for inversions between the second and third eigenmodes, these three vibration modes have been consistently observed in two-dimensional scenarios. In complex 3D cases with site-specific fracture sets, the direction of vibration is affected by the presence of different

fracture sets. The majority of field investigations indicate that the vibration directions are predominantly controlled by the fractures in closest proximity to each station (Colombero et al. 2017). Furthermore, the presence of subvertical fractures has been observed to significantly impact the frequency dip directions, while oblique basal fractures have been noted to affect mostly the dip angles (Colombero et al. 2017). In such cases, three-dimensional FEM modeling is crucial to support the analysis.

2.3 Cross-correlation of ambient seismic noise

The relative wave velocity change dV/V is one of the seismic parameters, along with eigenfrequencies, used for passive seismic monitoring and early warning of unstable rock slopes. This parameter can be extracted from ambient seismic noise recordings using the cross-correlation method.

The ambient noise correlation technique is used to reconstruct the impulse response between two sensors A and B by performing the cross-correlation $C(\tau)$ on the ambient seismic noise signal $\varphi(t)$, as if one station was the receiver and the other one the active source (Larose et al. 2015). In fact, the cross-correlation between the diffuse wavefield signals recorded simultaneously by A and B converge to the Green's function when the following conditions are met (Larose et al., 2015):

- The sources are uncorrelated in time.
- The sources are placed all around the receiver to reconstruct surface waves.
- There is a proper ratio between compressional and shear waves (equipartitioned field) to reconstruct bulk waves.

These requirements are rarely met in real cases but are compensated for by the presence of scattering phenomena occurring at the subsurface interfaces and discontinuities (Larose et al. 2015; Colombero et al. 2021).

The cross-correlation method is based on the idea that, if the sensors' locations are fixed and the ambient noise sources are statistically stable, then a time shift in the computed correlograms is only due to a seismic velocity change in the medium caused by a variation in the mechanical properties of the rock mass. In the case of a homogeneous velocity change, the following relation applies (Larose et al. 2015; Colombero et al. 2021):

$$\frac{dV}{V} = -\frac{dt}{t} \quad \text{Eq. 2.3}$$

The general workflow for extracting hourly or daily relative velocity changes dV/V from ambient seismic noise involves the following steps (Larose et al. 2015):

- Equalization of the frequency content of the ambient noise in the frequency domain through frequency normalization or spectral whitening.
- Amplitude normalization in the time domain (e.g. clipping, event removal or 1-bit processing) to reduce the statistical influence of rare, large amplitude events.
- Definition of the reference correlogram, typically the first, a specific part (e.g. a stable period) or the average correlogram over the recorded period.
- Comparison of each hourly or daily correlation $C_{AB}^d(t)$ with the reference correlation $C_{AB}^{ref}(t)$, typically employing the stretching technique.

The stretching technique consists in testing different dV/V values to find the one that maximizes the correlation coefficient. This task is performed by filtering the correlograms in narrow frequency bands with central frequency f_c and resampling them in time (stretching the time axis) according to Poupinet et al. (1984):

$$h_{f_c} \rightarrow h_{f_c} \left(t \left(1 - \frac{dV}{V} \right) \right) \quad \text{Eq. 2.4}$$

The calculation is typically performed on coda waves rather than direct waves. This is because coda waves spend more time traveling through the medium of interest and accumulate more changes along the way (Larose et al. 2015). This makes them more sensitive to mechanical variations and more stable in the presence of ambient noise variations. Once the relative velocity change dV/V at a given frequency has been detected, it is possible to relate it to a change in the stiffness of the material under investigation (Colombero et al. 2021):

$$V_s = \sqrt{\frac{G}{\rho}} \quad \text{Eq. 2.5}$$

where G is the shear modulus or modulus of stiffness and ρ is the density of the medium. The investigation depth is inversely proportional to the frequency on which dV/V is calculated by the stretching technique (Colombero et al. 2021). In essence, a decrease in the rock compartment rigidity, which can lead to instability and potential rockfall, determines a negative wave velocity variation, which is why seismic noise cross-correlation can be used for monitoring and early warning applications.

2.4 Driving mechanisms for rock mass resonant behavior

In the study of reversible variations in the resonance frequencies of unstable rock compartments, six driving mechanisms have been identified in the scientific literature (Colombero et al. 2021). Three of these mechanisms are directly associated with temperature changes: the *fracture effect*, the *surface effect*, and the *bulk effect*. Two mechanisms are influenced by water, either independently (*water effect*) or in combination with temperature (*ice effect*). The final mechanism pertains specifically to the hydro- and thermal behavior of clay.

Isolating and understanding the environmental influences on seismic parameters is crucial for distinguishing the origins of detected variations in these parameters. This distinction is critical for separating reversible fluctuations from irreversible changes, which indicate alterations in the mechanical properties of the rock mass. Such differentiation is essential for the effective use of seismic parameters for early warning purposes (Larose et al. 2015).

2.4.1 Fracture effect

The *fracture effect* refers to the effect of air temperature variations on the behavior of rock mass, particularly their joints. As the temperature rises, the rock mass undergoes thermal expansion, causing fractures and microcracks to close and increasing fracture contact stiffness. This results in a relative increase in the fundamental resonance frequency f_1 and a decrease in velocity variations dV/V . Conversely, as temperatures decrease, the rock mass contracts, causing fractures to open and fracture contact stiffness to decrease, resulting in opposite trends in f_1 and dV/V . This phenomenon, known as thermal dilation and contraction, is primarily driven by daily and seasonal temperature variations, with diurnal reversible changes typically ranging from 1% to 7% for f_1 and 1.5% to 5% for dV/V (Colombero et al. 2021). Seasonal variations, controlled by thermal effects, can range from 4% to 12% for f_1 and 2% to 12% for dV/V . These variations are particularly significant in highly fractured rock sites, where the seismic response is influenced by the number, opening, and persistence of fractures relative to the volume of the unstable compartment (Colombero et al. 2021).

2.4.2 Surface effect

The *surface effect* is characterized by the differential dilation between the rock surface and its bulk in response to air temperature variations. This phenomenon leads to an increase in internal stresses σ_i , and consequently an increase in bulk

stiffness K_b , which acts as a confining pressure. As the temperature increases, the surface effect causes an immediate increase in the fundamental resonance frequency and a positive velocity change, as observed in the seismic parameters. Conversely, as the temperature decreases, the process is reversed. The *surface effect* is recognized as a mechanism in addition to thermal dilation, particularly evident in immediate responses to daily air temperature variations. This effect is primarily due to heat propagation at the rock surface and is distinct from the subsequent *bulk effect*. While the *bulk effect* becomes more pronounced on longer time scales, as explained in the following section, the *surface effect* induces an immediate response in seismic parameters, highlighting its importance in understanding the dynamic behavior of rock masses under varying environmental conditions (Colombero et al. 2021).

2.4.3 Bulk effect

The *bulk effect* refers to the reduction in f_1 values and the negative velocity shift induced by temperature-driven changes in bulk stiffness when heat penetrates the bulk of an unstable compartment. Xia et al. (2011) proposed the following linear correlation between Young modulus (E_b) and temperature T :

$$E_b(T) = E_b(T_0)[1 - \theta(T - T_0)] \quad \text{Eq. 2.6}$$

where T_0 is a reference temperature and θ is a positive coefficient which depends on the material. Eq. 2.6 indicates that E_b decreases with increasing temperature, which subsequently reduces the bulk stiffness K_b and the shear modulus G_b , resulting in a decline of f_1 values and a negative velocity change dV/V . Conversely, a reduction in temperature will reverse this process. The *bulk effect* can result in reversible variations of up to $\pm 12\%$ in f_1 (Colombero et al. 2021).

The relative influence of the fracture or *bulk effect*, and the resulting time delay between external temperature changes and seismic parameter responses, is

contingent upon the size of the unstable compartment, the number and configuration of fractures, and the duration of thermal cycles. In general, the relationship between temperature cycles and compartment size is of paramount importance: larger unstable sectors take longer for the diffusive temperature front to penetrate significantly, thereby delaying the *bulk effect*'s manifestation.

In large unstable compartments, the penetration of temperature through the bulk rock is less effective, and fluctuations are primarily governed by fracture stiffness rather than bulk stiffness (Colombero, Baillet, et al. 2018). Consequently, it can be reasonably assumed that the fluctuations in resonance frequency in these scenarios will be in phase with the variations in air temperature on both the daily and seasonal scales (Colombero, Baillet, et al. 2018). An increase in ambient air temperature causes thermal expansion and microcracks closure, resulting in higher contact stiffness and thus higher resonance frequencies. Consequently, the *fracture effect* is responsible for short-term, daily observable changes, while the *bulk effect* may occur at the seasonal scale (Colombero et al. 2021).

In smaller compartments or highly fractured sites, the diffusive temperature front reaches significant depths more quickly, thereby affecting the overall stiffness of the rock mass (Burjánek et al. 2018). In these instances, the *bulk effect* can be observed not only at the seasonal scale but also as a primary driving mechanism at the daily scale, with variations up to $\pm 1\%$ on f_1 (Colombero et al. 2021). Here, an opposite trend is observed: as the Young modulus decreases with rising temperature, a corresponding decrease in resonance frequency is observed.

2.4.4 Water effect

The *water effect* is manifested as a reduction in both the contact and bulk shear moduli of the rock due to the increased mass and density resulting from water accumulation. Consequently, a reduction in the resonance frequency f_1 and a negative dV/V are anticipated in accordance with Eq. 2.1. Conversely, as the water table recedes and the material dries out, the opposite effect is expected. As a

consequence of the *water effect*, seismic parameters such as resonance frequency and seismic wave velocity are expected to exhibit a negative correlation with precipitation levels. Moreover, the impact of the *water effect* is markedly contingent upon the configuration of discontinuities within the unstable compartment. In particular, sites with open fractures in the posterior facilitate the effective drainage of infiltrating water, thereby reducing the retention within the rock volume. Consequently, such sites would not experience the reversible fluctuations in seismic parameters associated with precipitation patterns (Colombero et al. 2021).

2.4.5 Ice effect

The *ice effect* refers to a significant increase in fracture contact stiffness K_c resulting from the conversion of water in rock fractures to ice when temperatures drop below 0°C. This change in the mechanical properties of fractures affects seismic parameters, resulting in an increase in the resonance frequency f_1 and a positive velocity change dV/V . Conversely, a reversal of this effect is observed when ice within fractures melts. The presence of ice inside the fractures strengthens the connection between the unstable compartment and the stable area, as confirmed by the cross-correlation analysis of the signals recorded in both zones, which show higher CC values during the freezing period (Colombero et al. 2021). The *ice effect* is, therefore, closely linked to site-specific conditions and only manifests itself when the internal structure of fractures within the rock mass facilitates water retention and in climatic regions where temperatures drop below freezing.

2.4.6 Clay effect

The *clay effect* is a highly site-specific driving mechanism observed primarily in clayey unstable blocks. This phenomenon induces reversible fluctuations in seismic parameters that are uniquely influenced by the behavior of the clay. It generates a negative correlation between the resonance frequency f_1 and temperature T ,

coupled with a positive correlation between f_1 and precipitation P . This characteristic behavior is due to the response of normally consolidated clays to temperature variations: as the temperature increases, these clays tend to contract, resulting in the opening of superficial fractures. This behavior has a noticeable effect on f_1 values, which show variations of up to $\pm 5\%$ on a daily scale and $\pm 12\%$ over a quadrimester, yet there is no discernible correlation with dV/V . Conversely, in terms of correlation with precipitation, an increase in f_1 and a positive change in velocity are observed, as infiltrating water mitigates the clay's contraction tendencies by wetting its grains (Colombero et al. 2021).

2.5 Fundamentals of the finite element method (FEM)

The finite element method (FEM) is a numerical technique that solves complex mathematical problems by breaking them down into smaller parts called finite elements which are connected at points called nodes. These nodes form a mesh that represents the problem domain. FEM approximates the solution by shifting from solving complex continuous equations over the entire domain to solving simpler equations for each discrete element. These local solutions are then interpolated into a global solution that approximates the solution to the original problem over the entire domain. In essence, FEM is a discretization and interpolation method. In geotechnical calculations, the finite element method involves six steps as described by Potts and Zdravković (1999) and discussed in the following paragraphs.

2.5.1 Element discretization

The element discretization step involves discretizing the geometry of the boundary value problem and transforming it into a mesh of small regions called finite elements. The first task, therefore, is to define and quantify the original boundary value problem using a discretized geometry, while applying the necessary simplifications. It is

important to achieve accurate discretization of the problem's boundary to minimize the initial approximation error, as this error will propagate throughout the problem's solution.

The boundary geometry is then replaced by a mesh of finite elements. These elements have key points, or nodes, defined at their boundaries or within the elements. For example, nodes are typically placed at the corners of elements with straight sides, while elements with curved sides require an additional node at the midpoint of each side. The geometry of the finite elements is thus determined by the coordinates of their nodes.

The complete final mesh consists of the entire set of elements connected by their sides and nodes. A systematic numbering of both nodes and elements is essential to reference the complete mesh. They are numbered separately but similarly, usually sequentially from left to right. In addition, an element connectivity list is generated to describe the location of each element by specifying the nodes of each one of them, usually in a counterclockwise order.

A critical aspect of this stage is defining the appropriate number of elements based on the specific problem under investigation. It is important to find a balance between the accuracy of the results and the computational time required, both of which depend on the number of elements. In addition, considerations of the original shape of the boundary, the presence of any geometric discontinuities, and the applied boundary conditions are essential. In general, higher-order elements with mid-side nodes are recommended for curved boundaries or curved material interfaces; geometric discontinuities such as corners, cracks, or load discontinuities at the boundary also suggest a natural form of subdivision with nodes placed at these points.

The size and number of elements in combination with these factors depend on the material behavior. For linear materials, only areas characterized by rapid variation of the unknowns (e.g., a cut in a block) require a refined mesh to obtain accurate results. For nonlinear materials, the situation is more complex because

additional factors such as boundary conditions and material properties must be considered when generating the mesh. In general, it is good practice to create a mesh of finite elements that are as regular as possible. Figure 2.1 shows some examples of discretization for two-dimensional cases.

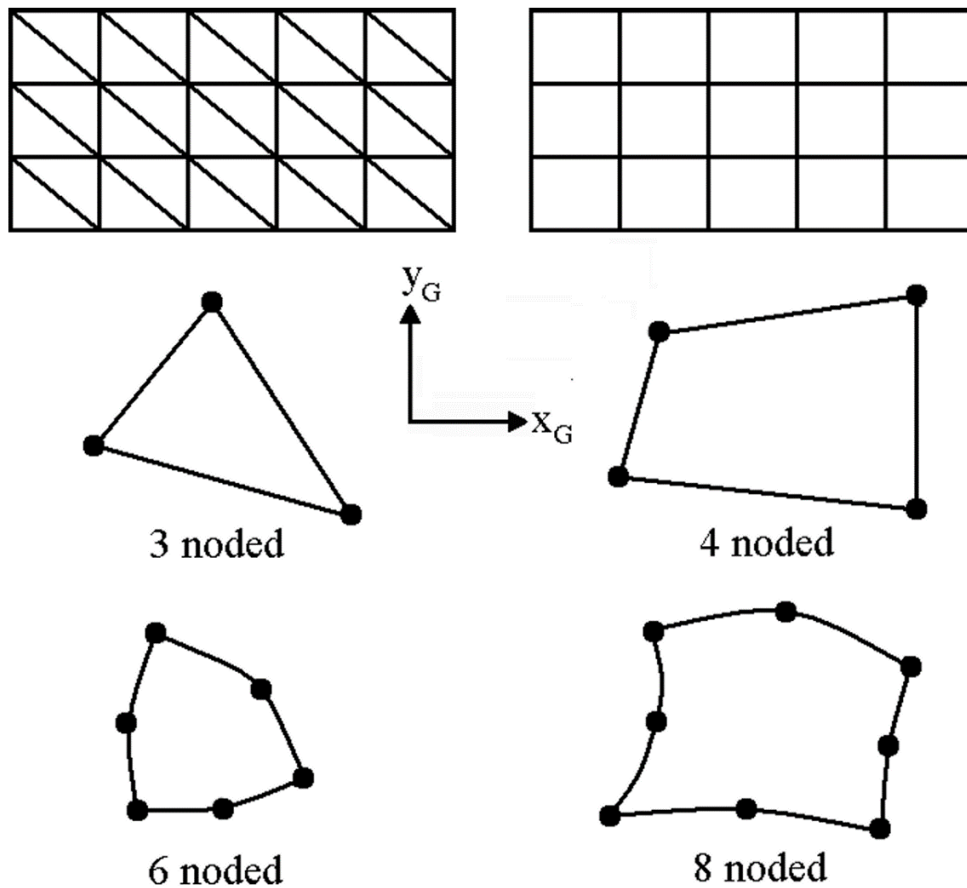


Figure 2.1 Typical 2D finite elements (Potts and Zdravković 1999).

2.5.2 Primary variable approximation

This step entails the selection of a primary variable, such as displacement or stress, and the formulation of a rule for how that variable should vary across a finite element in terms of node values. In geotechnical engineering, the primary variable is typically displacement, from which stresses and strains are calculated as secondary quantities. The FEM approach considers displacements at a discrete number of

points, the mesh nodes, rather than as a continuous function over the entire domain. The primary approximation in this step is the assumption of a specific rule for how the displacement components vary across the domain under study.

2.5.3 Element and global equations

These steps involve deriving equations comprising parameters specific to the constitutive model by means of an appropriate variational principle, which is typically the principle of minimum potential energy. Initially, only the element equation is considered (Eq. 2.7):

$$[K_E] \{\Delta d_E\} = \{\Delta R_E\} \quad \text{Eq. 2.7}$$

where $[K_E]$ represents the element stiffness matrix, $\{\Delta d_E\}$ is the vector of incremental nodal displacements for the element, and $\{\Delta R_E\}$ is the vector of incremental nodal forces for the element. Once Eq. 2.7 has been calculated for each finite element, the model combines these element equations into global equations (Eq. 2.8):

$$[K_G] \{\Delta d_G\} = \{\Delta R_G\} \quad \text{Eq. 2.8}$$

where the vectors and matrices refer to global parameters, not element-specific ones.

2.5.4 Boundary conditions

To establish the global system of equations, it is essential to define boundary conditions that comprehensively describe the boundary value problem. These conditions include loading conditions that affect $\{\Delta R_G\}$ and displacement conditions that affect $\{\Delta d_G\}$. Their effects are incorporated directly into the system's matrices or vectors, depending on the type of condition.

Loading conditions, such as line or point forces, are integrated directly into the right vector $\{\Delta R_G\}$, while pressure boundary conditions require conversion to equivalent node forces before being integrated into $\{\Delta R_G\}$.

For displacement conditions, a sufficient number must be specified to constrain all rigid body deformation modes, such as rotations and translations of the entire finite element mesh, to avoid singularity of the global stiffness matrix which would make the system impossible to solve.

2.5.5 Solving the global equations

Once the global equations and boundary conditions are defined, they form a large set of simultaneous equations that are solved to obtain the nodal displacement vector $\{\Delta d_G\}$. Several mathematical techniques can be used to find the solution. In the case of two-dimensional problems, direct solution methods, such as Gaussian elimination, are effective. However, for three-dimensional problems, these methods can result in excessive computation times due to the intensive process of inverting the stiffness matrix. In three-dimensional FEM analysis, iterative techniques are more cost-effective because they store only the non-zero elements of the stiffness matrix at each iteration, significantly reducing memory requirements.

After solving for nodal displacements, secondary quantities, such as stresses and strains, can be calculated from these displacements, providing all necessary results. The results may then be displayed graphically by plotting the nodes according to their global coordinates and displaying the calculated parameters with different colors, which facilitates visualization and analysis.

2.5.6 Adopted FEM software tools

2.5.6.1 COMSOL Multiphysics

COMSOL Multiphysics¹ is a robust interactive simulation environment capable of modeling and solving a diverse array of engineering problems. This software features an integrated desktop environment with a Model Builder that offers a comprehensive overview of the model and access to all functionalities. COMSOL Multiphysics allows for the seamless extension of conventional single-physics models into multi-physics models, enabling the simultaneous solution of coupled phenomena.

COMSOL Multiphysics' built-in physics interfaces allow to apply physical quantities and variables such as material properties, loads, constraints, sources, and fluxes directly to the domain, without the need to manually define the underlying equations and independently of the computational mesh. It then internally compiles the set of equations representing the model. A key feature of COMSOL Multiphysics is its ability to create sequences that record all steps involved in creating the geometry, mesh, physics, studies and solver setting, facilitating the parametrization of the model. Therefore, by modifying an element in the model tree and rerunning the sequences, the information and data are automatically updated.

COMSOL Multiphysics stems out for its user-friendly interface and its versatility, which enables to perform various types of studies, including stationary and time-dependent studies, and linear and nonlinear ones. The computational approach is based on the finite element method, supporting both two-dimensional and three-dimensional modeling, and offers a wide range of options for mesh element shapes, including triangles, quadrilaterals, tetrahedrons, hexahedrons, prisms, and pyramids.

COMSOL Multiphysics has been used in this thesis project to perform the Eigenfrequency analysis, included in the Mechanics Module.

¹ <https://www.comsol.com/comsol-multiphysics>. Last accessed 02/07/2024.

2.5.6.2 MIDAS GTS NX

GTS NX², developed by MIDAS Information Technology Co., is a finite element analysis software designed for advanced geotechnical analysis, including soil and rock deformation and stability, soil-structure interaction, groundwater flow, and dynamic vibrations. It is mainly used for analysis, testing and design tasks in geotechnical, civil and mining engineering. In this thesis research project GTS NX has been used to perform both eigenfrequency and thermo-mechanical analysis.

GTS NX provides sophisticated modeling capabilities through CAD-based commands that resemble standard CAD modeling interfaces, which are typically familiar to engineers. In addition, it supports a wide range of CAD file types to speed up the drafting phase, while specific tools are provided for accurate terrain and soil layer modeling.

In terms of mesh generation, GTS NX integrates hybrid generation functions that combine hexahedral and tetrahedral elements. The integration of hexahedrons optimizes the accuracy of the results, while tetrahedrons are more effective for modeling corners and sharper curves. Element size can be controlled both automatically and manually to ensure that the mesh fits the domain geometry accurately. The auto-mesh feature automates the generation of the mesh, while standard protrusion operations, such as extrusion and revolution, facilitate a seamless transition from 2D to 3D meshes.

GTS NX includes a high-performance 64-bit parallel solver that distributes the computational load of the stiffness matrix across cores for increased speed. The calculation is further accelerated by a special feature of the solver that can save the element matrix to disk when it detects that the system is running out of memory. Another key feature of GTS NX is its post-processing engine which can convert complex models into simple cross-sections, planes and contour lines, and displays excellent graphical outputs.

² <https://www.midasgeotech.com/solution/gtsnx>. Last accessed 03/07/2024.

3 LABORATORY SCALE ACTIVITY

In line with the objectives of the *THEROCKLAB* PRIN project, numerical simulations and laboratory activities have been explored as complementary tools to field activities conducted at experimental sites.

The laboratory scale activities within the *THEROCKLAB* project focus on assessing the effect of external thermal and hydromechanical factors on rock properties and stability under controlled conditions. Additionally, these activities aim to determine the feasibility of performing such analyses on a small scale and to evaluate whether the methodologies and results can be effectively translated to field-scale applications.

As part of this thesis, preliminary laboratory scale work was conducted to inform future analysis in subsequent *THEROCKLAB* phases. Specifically, it aimed to achieve the following objectives:

- Characterize the mechanical parameters of the specimen.
- Gain familiarity with laboratory instrumentation.
- Investigate the frequency ranges at which resonance frequencies occur and their expected amplitudes at the small scale.
- Assess the suitability of available instrumentation for the intended applications at the laboratory scale within the *THEROCKLAB* project.
- Evaluate the consistency of the results between seismic recording laboratory tests and eigenfrequency FEM simulations.

- Use FEM simulation to guide the design of future rock samples, which will then be used to study the effects of cut geometry and hydrothermal factors on rock mass stability.

The laboratory analysis was conducted on two specimens of different geometry and material: a granite column and a marble slab, both available in the geophysics laboratory of Politecnico of Turin and previously uncharacterized. These specimens were designated as Specimen A and Specimen B, respectively. The dimensions of these specimens are reported in Table 3.1.

Table 3.1 Dimensions of Specimen A and Specimen B.

Dimension	Specimen A	Specimen B
Width (X)	9.5 cm	15.2 cm
Depth (Y)	10.1 cm	7.9 cm
Height (Z)	29.9 cm	15.3 cm

Photogrammetric techniques were used to reconstruct detailed three-dimensional models, with a distinct set of photographs for each specimen. The photographs were subjected to a structure-from-motion process using Metashape software to generate sparse and dense point clouds. Subsequently, the dense point clouds data was then processed in CloudCompare, where outliers were removed, and mesh reconstruction was performed using the Dirichlet algorithm. The details of the photogrammetric 3D modeling procedure are presented in Table 3.2, while the final 3D models are illustrated in Figures 3.1 and 3.2.

Table 3.2 Photogrammetric 3D model details for Specimen A and Specimen B.

	Specimen A	Specimen B
Number of photograms	89	44
Number of points (dense cloud)	1,781,473	275,801
Octree depth value	10	10



Figure 3.1 3D model of Specimen A generated using photogrammetric techniques. Units in meters.



Figure 3.2 3D model of Specimen B generated using photogrammetric techniques. Units in meters.

3.1 Geomechanical characterization of specimens

This chapter outlines the determination of fundamental rock mass parameters including unit weight, Young elastic modulus, Poisson's ratio, and shear modulus. These parameters were obtained through basic laboratory tests including ultrasonic pulse velocity (UPV) testing. The following sections will provide a detailed explanation of the procedures performed.

3.1.1 Principles of ultrasonic pulse velocity (UPV) testing

Ultrasonic P-wave Velocity (UPV) testing is a cost-effective, reliable non-destructive method commonly used to estimate the velocity of a wave through a solid medium. It is suitable for both field and laboratory scale in a wide range of fields, such as mining, geotechnical and civil engineering (Garia et al. 2021). As for rock engineering, UPV testing is widely used to characterize and categorize different types of rocks, since the ultrasonic P-wave velocity results are affected by several petrophysical and geomechanical properties of the rock, such as unit weight, lithology, grain size and shape, anisotropy, porosity, confining pressure, temperature, and weathering.


UPV testing is performed using a portable non-destructive digital ultrasonic indicating tester, which is commonly referred to as a PUNDIT. The test apparatus consists of two transducers of a given frequency, one acting as a transmitter and the other as a receiver, a pulse generator, and an electronic counter to measure the wave propagation time. Measurements can be made with a single transducer acting as both the transmitter and receiver (*pulse-echo technique*) or with both transducers (*through-transmission technique*) (Garia et al. 2021). UPV values are calculated from the length of the sample between the two transducers and from the transit travel time of the ultrasonic pulse, which is measured.

3.1.2 Procedures for UPV testing

UPV testing was performed using a Proceq Pundit Lab instrument (see Table 3.3 for technical specifications³) with two flat-head transducers in *through-transmission* configuration. The length of the main dimension of the specimen was measured manually with a tape measure. Coupling gel was applied to the faces of the transducers to prevent the formation of air pockets, thus ensuring full contact between the transducers and the surface to which they were applied. The transducers were then calibrated using a specific core of acrylic glass. They were then positioned on the opposing end parallel surfaces of the specimens across the previously measured side.

The data visualization and acquisition processes were conducted via the Punditlink desktop application (software version 2.4.0), which was connected to the PUNDIT through a USB port. The *Data Logging* mode was used to define a test sequence.

Table 3.3 Technical specifications of the Pundit Lab device for UPV testing.

Pundit Lab technical specifications		
	Device Name	Pundit Lab
	Serial number	PL02-005-0300
	Bandwidth	20 to 500 kHz
	Measuring resolution	0.1 μ s
	Pulse voltage	± 125 V to ± 500 V
	Nominal Transducer Frequency	24 – 500 kHz
	Pulse Shape	Square Wave
	Pulse Delay	-
	Number of Channels	1
	Measuring Range	Up to 15 m depending on material

³ <https://www.screeningeagle.com/en/products/pundit-lab>. Last accessed 03/07/2024.

The configuration settings for the PUNDIT and the *Data Logging* settings are presented in Tables 3.4 and 3.5, respectively.

Table 3.4 Pundit Lab configuration settings for UPV testing.

Pundit Lab configuration settings	
Pulse length	9.3 μ s
Probe frequency	54 kHz
Pulse amplitude	500 V
Rx probe gain	10x
Calibration time offset	-3.6 μ s
Distance	30 cm (A), 15.2 cm (B)
Time frame	200 μ s
Sampling frequency	2000 (kHz)

Table 3.5 Configuration settings for the *Data Logging* acquisition mode.

<i>Data Logging</i> settings	
Interval	1 s
Number of events	10
Readings per event	1

3.1.3 Results of UPV testing

For both Specimen A and Specimen B, three test sequences were performed, each consisting of ten recorded events, resulting in a total of 30 measurements and three different datasets for each specimen. Dataset 1 was obtained using standard flat-head transducers, while Dataset 2 and Dataset 3 were obtained using specialized flat-head transducers tailored for S-wave velocity detection (ten recordings with 0° polarization and ten with a 180° polarization).

For each dataset, the signal averaged over the ten recordings was then calculated and normalized to the maximum. The mean signal of Dataset 1 was used

to obtain the P-wave velocity by manually picking the first arrival time (Figures 3.3 and 3.5). By dividing the length of the specimen by this arrival time, the P-wave velocity was calculated and validated against the P-wave velocity provided by the PUNDIT. The two averaged signals from Dataset 2 and Dataset 3 were then juxtaposed to determine the point of polarization inversion corresponding to the arrival time of the S-waves (Figures 3.4 and 3.6). The S-wave velocity was then calculated from this identified point. This entire procedure was performed twice, once for specimen A and once for specimen B. Table 3.6 presents the results of the UPV testing.

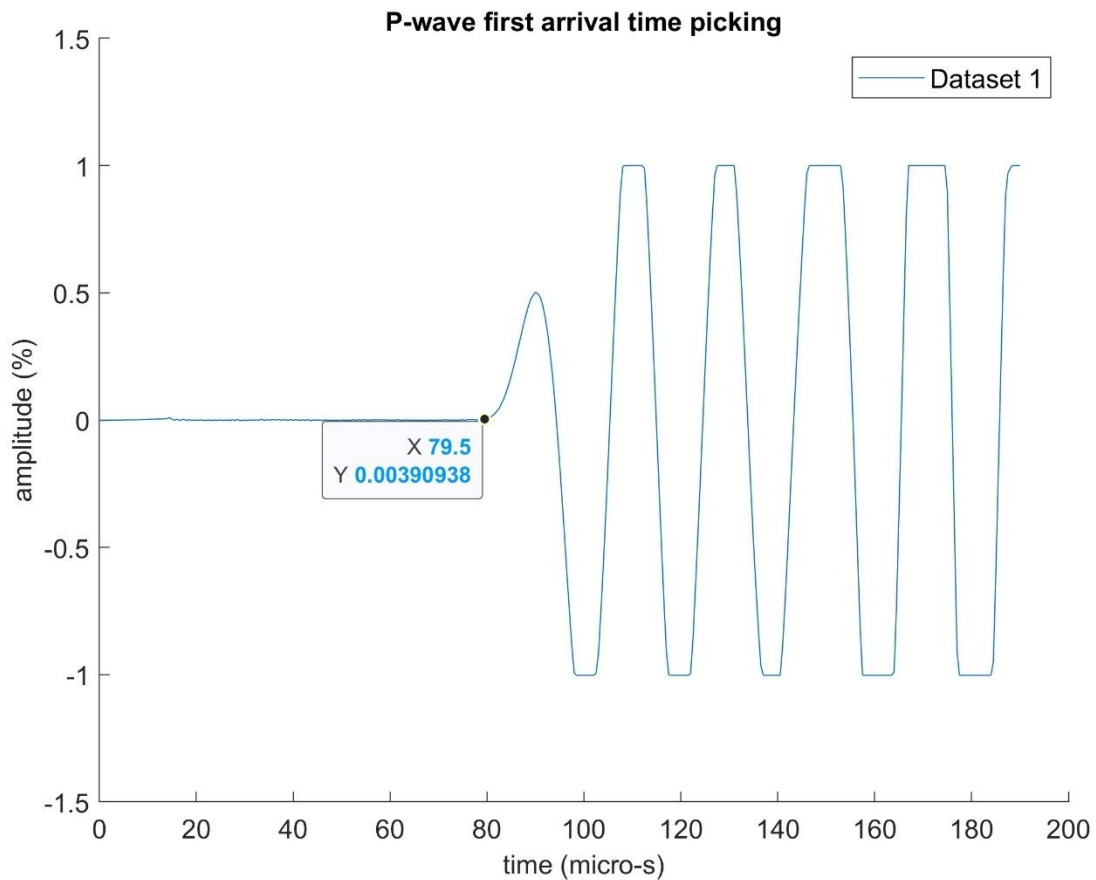


Figure 3.3 Determination of P-wave first arrival time for Specimen A.

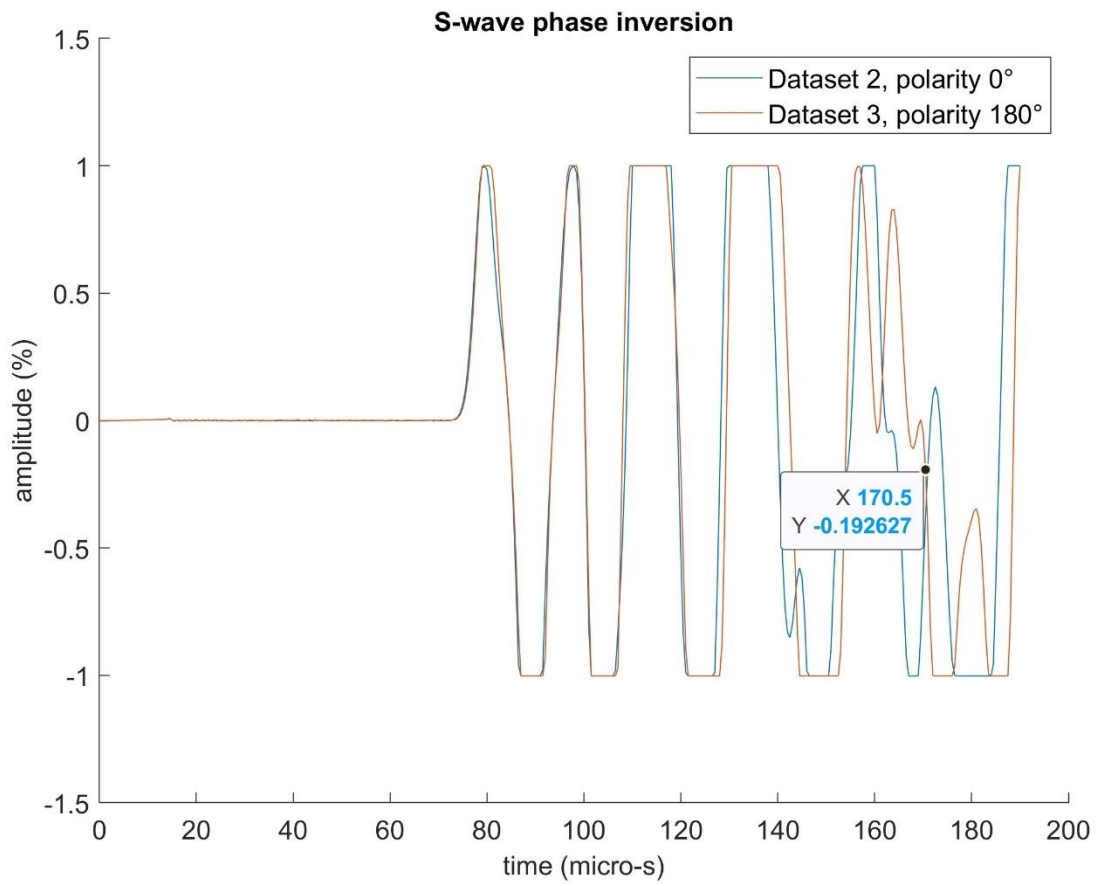


Figure 3.4 Determination of S-wave polarization inversion time for Specimen A.

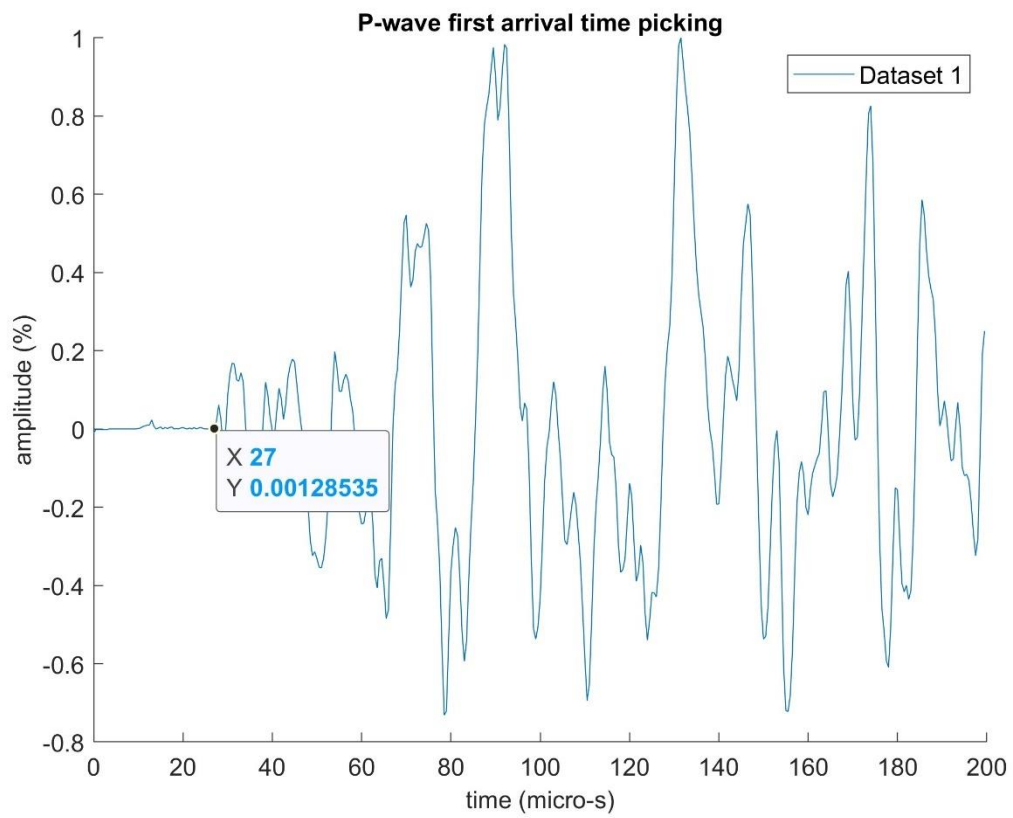


Figure 3.5 Determination of P-wave first arrival time for Specimen B.

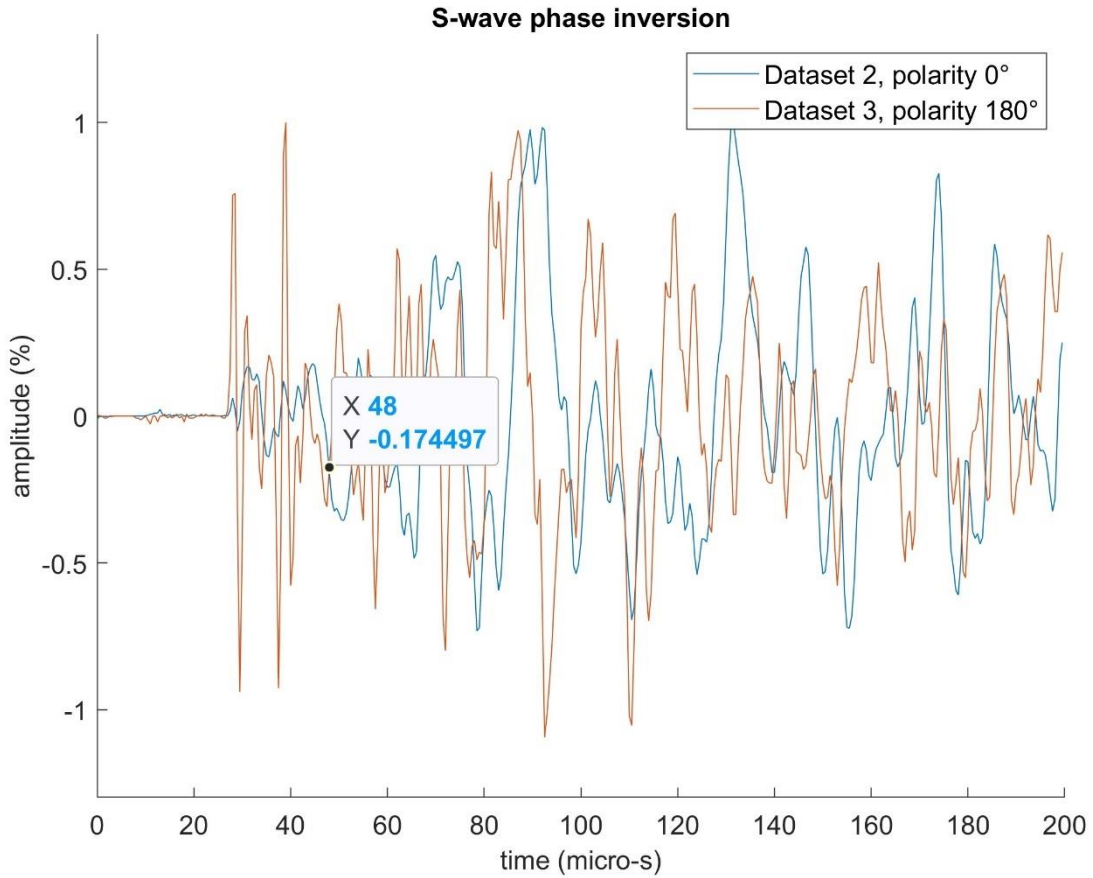


Figure 3.6 Determination of S-wave polarization inversion time for Specimen B.

Table 3.6 UPV testing results for Specimen A and Specimen B.

UPV tests result	Specimen A	Specimen B
Sample length (<i>cm</i>)	29.9	15.3
First arrival time (μs)	79.5	27
P-wave velocity (<i>m/s</i>)	3720	5186
Polarization inversion time (μs)	170.5	48
S-wave velocity (<i>m/s</i>)	1750	3187

3.1.4 Calculation of elastic parameters

The S-wave velocity (V_s) and P-wave velocity (V_p) values obtained from the UPV tests were used as the basis for calculating the mechanical parameters of the rock

samples analyzed. Seismic wave velocities are inherently related to the petrophysical and geomechanical properties of the medium they traverse. Poisson's ratio ν , shear modulus G and Young modulus E were calculated using the velocity values obtained. The Poisson's ratio was derived solely from the V_s and V_p values (Eq. 3.1), while the calculation of G and E required the bulk density value (Eq. 3.2 and Eq. 3.3). The bulk density value, ρ , was calculated indirectly from the mass and volume of the specimens. The mass was measured using a laboratory scale, while the volume was determined indirectly from the 3D model using a specific tool within CloudCompare.

$$\nu = \frac{(V_p/V_s)^2 - 2}{2(V_p/V_s)^2 - 2} \quad \text{Eq. 3.1}$$

$$G = \rho V_s^2 \quad \text{Eq. 3.2}$$

$$E = 2G(1 + \nu) \quad \text{Eq. 3.3}$$

The parameters obtained from laboratory characterization of the specimens are presented in Table 3.7.

Table 3.7 Geomechanical characterization results for Specimen A and Specimen B.

Parameter	Specimen A	Specimen B
Volume (dm^3)	2.9	1.8
Mass (kg)	7.3	4.9
Bulk density ρ (kg/m^3)	2541	2674
Poisson's ration ν (-)	0.35	0.20
Young modulus E (GPa)	22.2	65.0
Shear modulus G (GPa)	8.2	27.2

3.2 FEM eigenfrequency analysis at the laboratory scale

Eigenfrequency analysis is a common type of analysis supported by finite element (FEM) simulation softwares, used to solve for the natural frequencies of a system and the shapes of the corresponding eigenmodes. While eigenfrequency analysis cannot determine the amplitude of any physical vibration, it provides the mode shapes. To ascertain the actual size of the deformation, knowledge about the excitation and damping properties is required⁴.

The eigenfrequency analysis of Specimen A and Specimen B was performed using two finite element (FEM) software programs, COMSOL Multiphysics and GTS NX, with the following objectives:

- Estimate the resonance frequencies of the two samples, which serve as reference values for comparison with seismic recording laboratory tests.
- Evaluate whether the two software packages provide consistent results.

The material properties of both specimens were defined using the parameters obtained from laboratory characterization (see Table 3.7). For the purposes of the eigenfrequency analysis, where failure mechanisms and plastic deformation are not the focus, the materials were modeled as linear elastic. Subsequently, a mesh was generated, and fixed boundary conditions were applied to the base of each specimen to replicate the laboratory setup where rock samples are placed on a workbench. The results of this analysis are presented in Tables 3.8 and 3.9.

⁴ <https://www.comsol.com/multiphysics/eigenfrequency-analysis>. Last accessed 03/07/2024.

Table 3.8 Eigenmode Analysis Comparison: GTS NX vs. COMSOL Multiphysics for Specimen A.

	Specimen A			
	COMSOL	GTS NX	Error (%)	Eigenmode
$f_1(\text{Hz})$	478	498	4.1	Bending perpendicular to the shorter side
$f_2(\text{Hz})$	503	521	3.4	Bending perpendicular to the longer side
$f_3(\text{Hz})$	1381	1439	4.2	Torsion around the vertical axis

Table 3.9 Eigenmode Analysis Comparison: GTS NX vs. COMSOL Multiphysics for Specimen B.

	Specimen A			
	COMSOL	GTS NX	Error (%)	Eigenmode
$f_1(\text{Hz})$	2316	2310	0.3	Bending perpendicular to the longer side
$f_2(\text{Hz})$	3431	3406	0.7	Bending perpendicular to the shorter side
$f_3(\text{Hz})$	4243	4242	0.03	Torsion around the vertical axis

The comparison between the two software packages shows quite similar results, with discrepancies down to about 4.2% for both specimens. This close agreement between the two FEM tools reinforces the reliability of the eigenfrequency analysis performed.

As predicted by Equation 2.1, Specimen A exhibits lower resonance frequencies. This outcome is consistent with its lower Young modulus, which directly affects stiffness, and with its higher mass. The simulated eigenmodes are consistent with those documented in the literature, with f_1 and f_2 corresponding to bending modes, and f_3 to torsion. However, there are differences in the eigenmodes between the two specimens: Specimen A shows f_1 corresponding to bending perpendicular to its shorter side, while Specimen B shows f_1 corresponding to bending

perpendicular to its longer side. It is also noteworthy that Specimen A has an almost square cross section, while Specimen B has a significantly elongated one.

Figures 3.7 through 3.12 display the eigenmode displacements corresponding to the first three resonance frequencies for both Specimen A and Specimen B, obtained with COMSOL Multiphysics. Correspondingly, Figures 3.13 through 3.18 present these results as modeled on GTS NX.

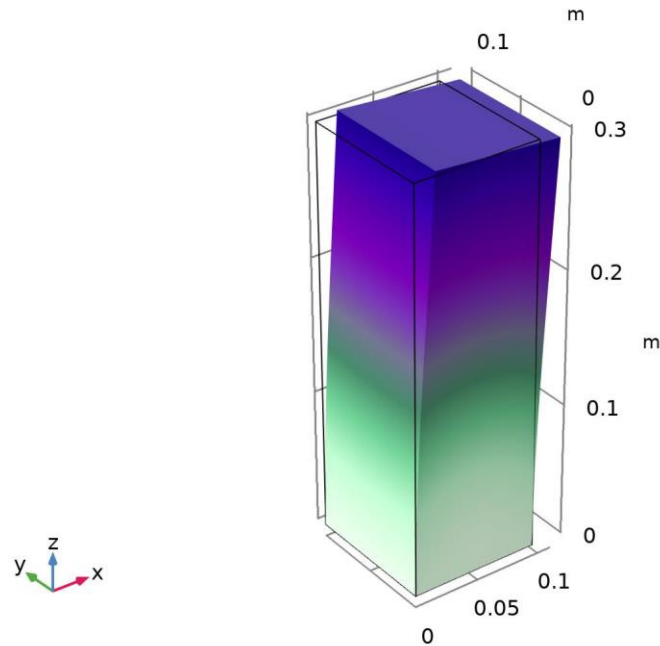


Figure 3.7 First eigenmode displacement visualization in COMSOL Multiphysics for Specimen A.

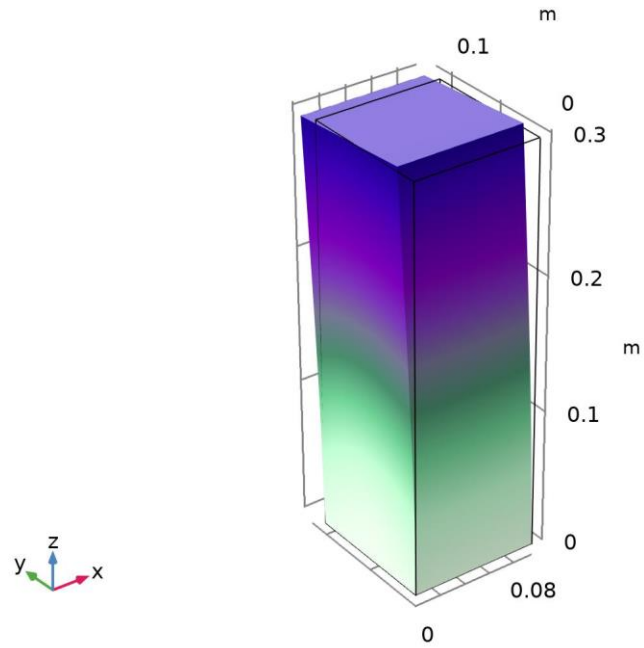


Figure 3.8 Second eigenmode displacement visualization in COMSOL Multiphysics for Specimen A.

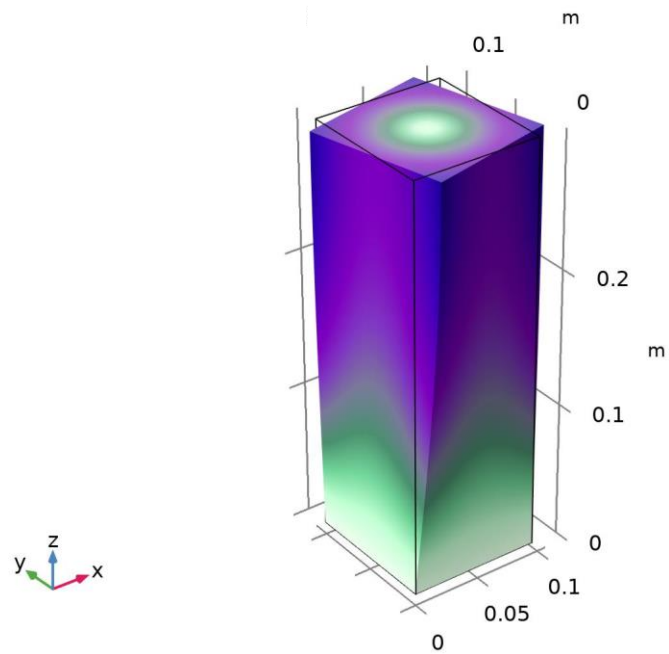


Figure 3.9 Third eigenmode displacement visualization in COMSOL Multiphysics for Specimen A.

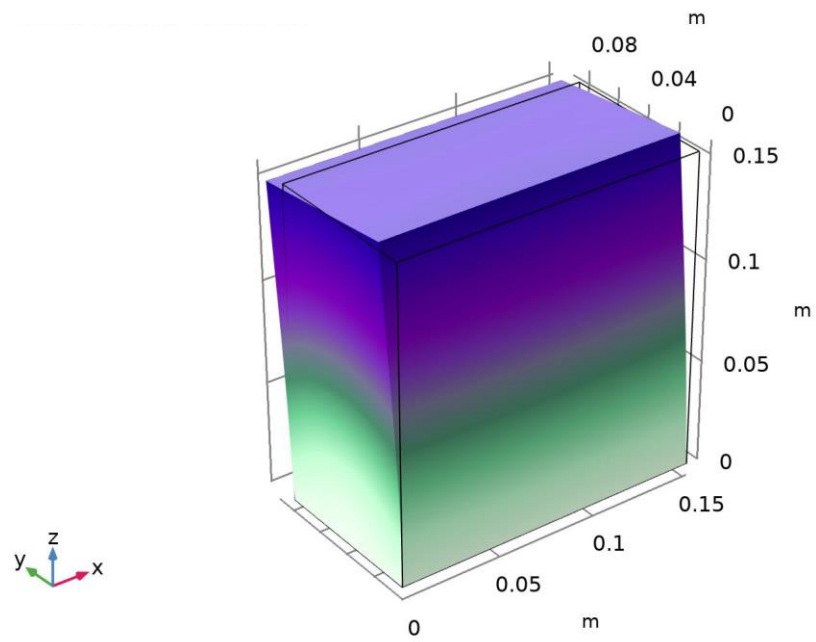


Figure 3.10 First eigenmode displacement visualization in COMSOL Multiphysics for Specimen B.

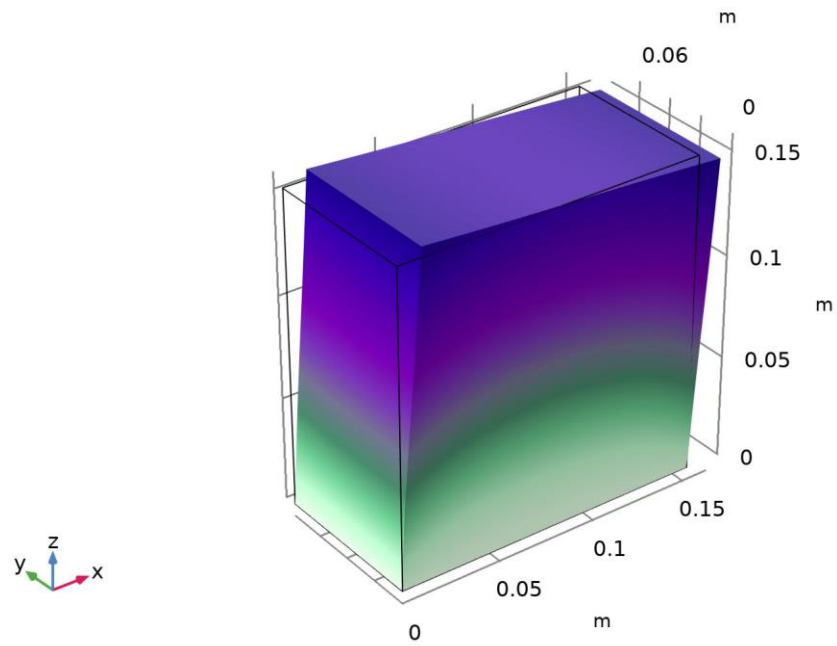


Figure 3.11 Second eigenmode displacement visualization in COMSOL Multiphysics for Specimen B.

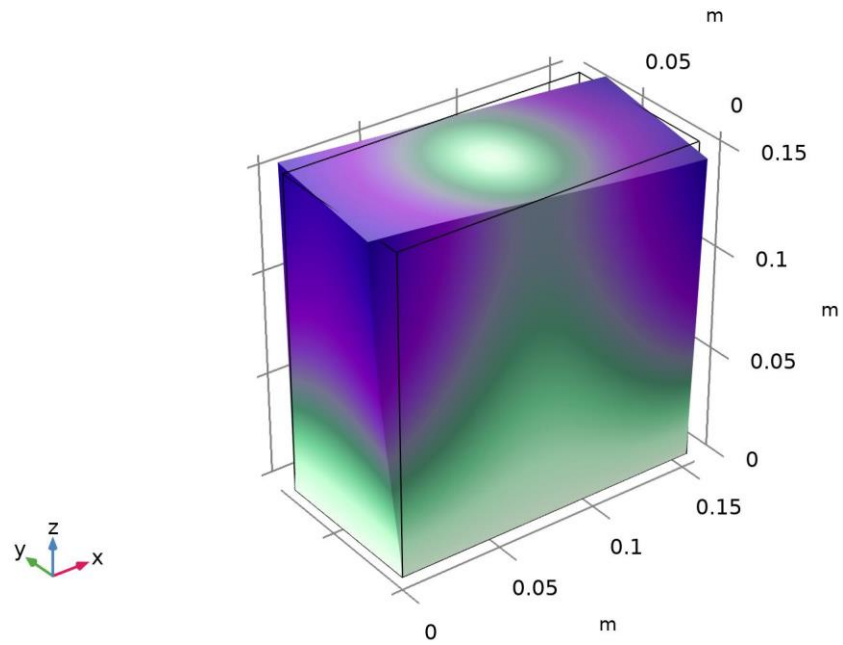


Figure 3.12 Third eigenmode displacement visualization in COMSOL Multiphysics for Specimen B.

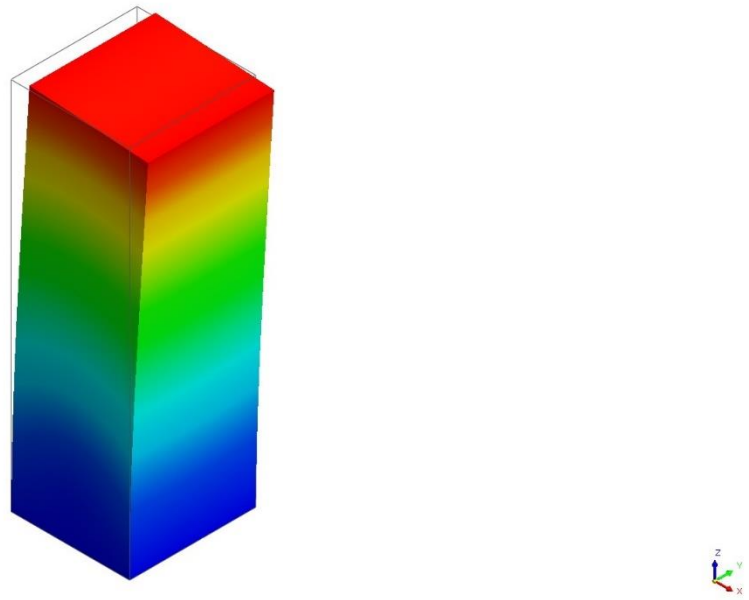


Figure 3.13 First eigenmode displacement visualization in GTS NX for Specimen A.



Figure 3.14 Second eigenmode displacement visualization in GTS NX for Specimen A.

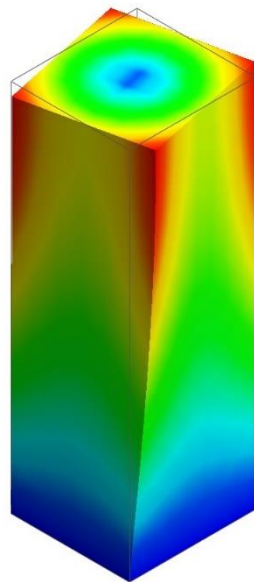


Figure 3.15 Third eigenmode displacement visualization in GTS NX for Specimen A.

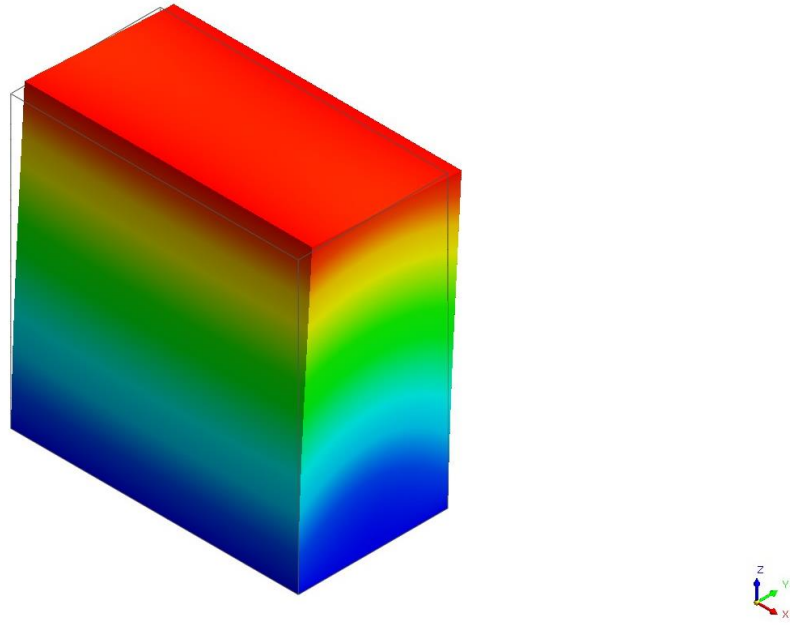


Figure 3.16 First eigenmode displacement visualization in GTS NX for Specimen B.

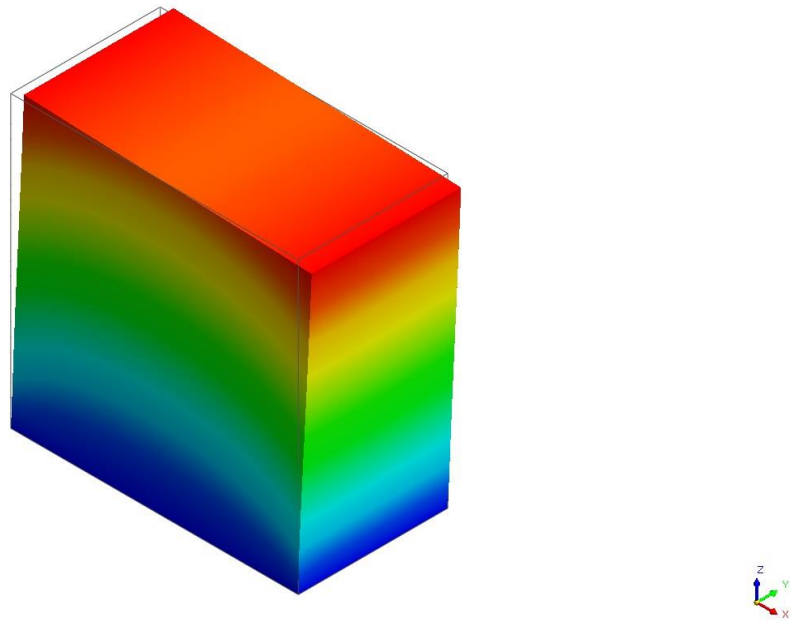


Figure 3.17 Second eigenmode displacement visualization in GTS NX for Specimen B.

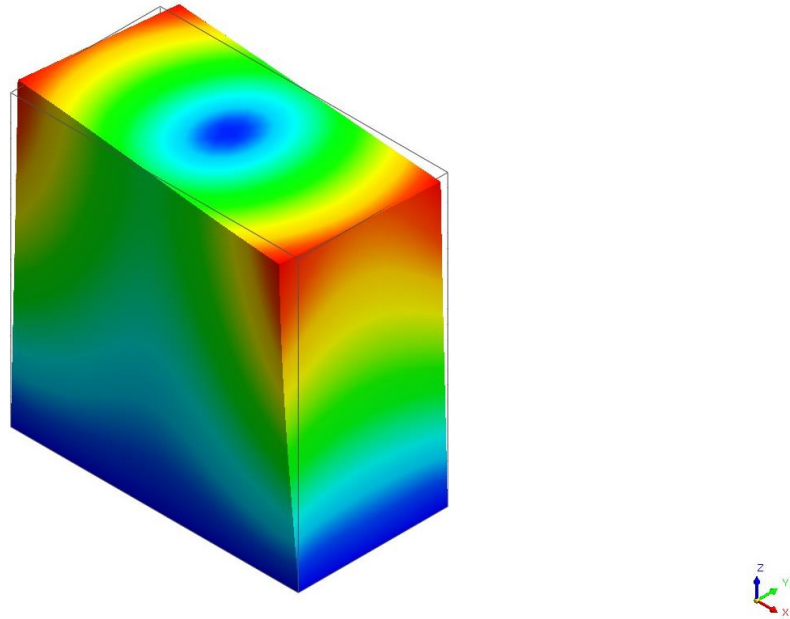


Figure 3.18 Third eigenmode displacement visualization in GTS NX for Specimen B.

3.3 H/V spectral ratio simulation at the laboratory scale

Spectral ratios H/V were simulated for both rock samples to gain deeper understanding of their resonant behavior and to predict the outcomes of laboratory testing. A time-dependent simulation was performed in COMSOL Multiphysics to simulate the acceleration induced at the top of the specimen. First, acceleration components in the three orthogonal directions were recorded by a triaxial sensor placed on the workbench near the base of the specimens. The 1.5-second signals (Figure 3.19) were then imported into COMSOL Multiphysics as acceleration functions to define the prescribed acceleration constraints at a point in the center of the sample base. Furthermore, fixed base constraints were defined to replicate the laboratory setup. Once the time-dependent study was solved, the induced acceleration at the center of the top surface of each sample was exported and used to calculate the H/V ratio with a custom MATLAB code.

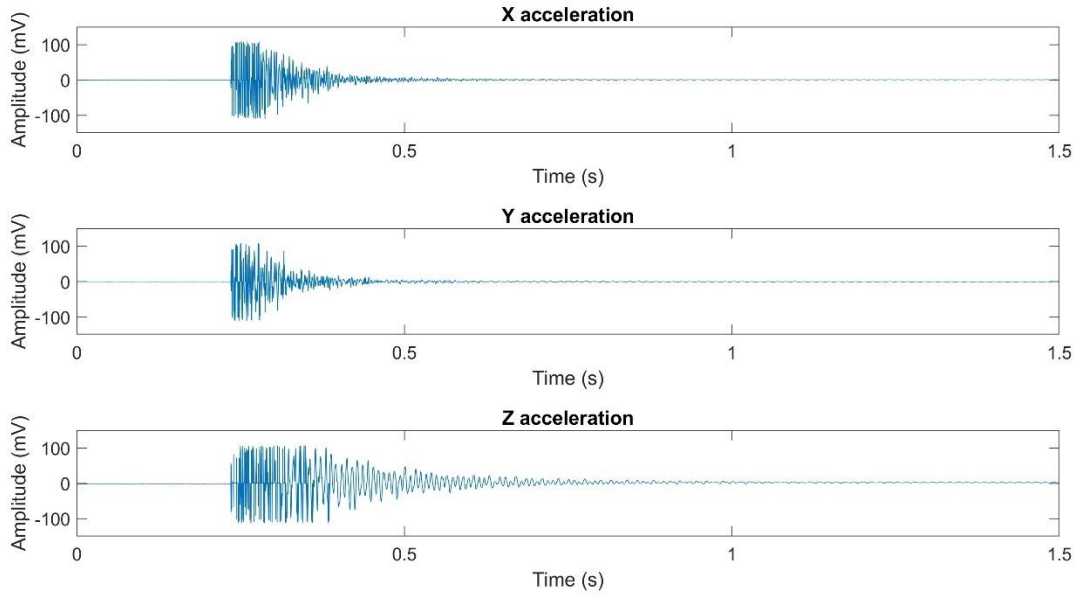


Figure 3.19 Base acceleration inputs (X, Y, Z) for H/V simulation.

A key consideration was to ensure that the maximum mesh element size did not exceed L_{max} (Colombero et al. 2017), defined by Eq. 3.4:

$$L_{max} = \frac{V_{R\ min}}{10f_{max}} = \frac{0.92V_s}{10f_{max}} \quad \text{Eq. 3.4}$$

where $V_{R\ min}$ is the minimum Rayleigh velocity, V_s is the S-wave velocity, and f_{max} is the upper frequency limit at which most of the signal energy is contained. By examining the frequency spectrum of the three acceleration components (Figure 3.20), it was determined that f_{max} should be set to 1000 Hz. Using the S-wave velocity values from Table 3.6, the maximum element size L_{max} was calculated as 16.1 cm for Specimen A and 29.3 cm for Specimen B.

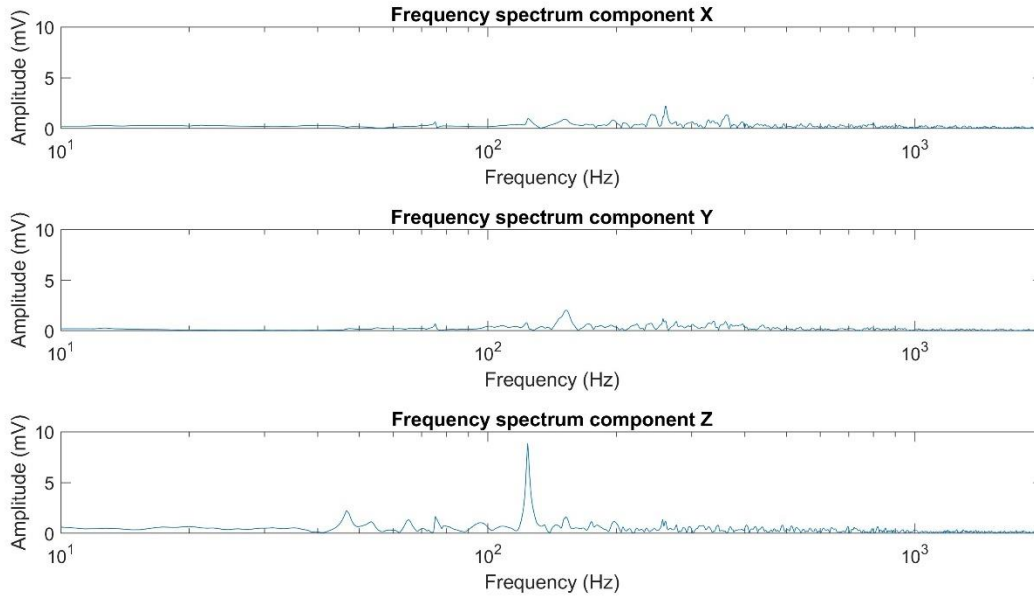


Figure 3.20 Frequency spectrum of base acceleration inputs (X, Y, Z) for H/V simulation.

The sampling frequency of the induced acceleration was set according to the expected eigenfrequency values from the eigenfrequency analysis. The simulated f_3 value is 1439 Hz for Specimen A and 4242 Hz for Specimen B. Therefore, the sampling frequency was set to investigate up to 2000 Hz and 5000 Hz, respectively. The mesh size and sampling parameters for both specimens are reported in Table 3.10.

Table 3.10 L_{max} , sampling frequency and Nyquist frequency for H/V simulation for Specimen A and Specimen B.

	Specimen A	Specimen B
L_{max} (cm)	16.1	29.3
Sampling frequency (Hz)	4000	10000
Nyquist frequency (Hz)	2000	5000

Figures 3.21 and 3.22 display the simulated H/V spectral ratios. For both specimens, the absolute maximum corresponds to the simulated f_1 value, but no peaks are observed at f_2 and f_3 . Furthermore, the H/V peak value for specimen A is

almost twice that of specimen B. These findings are highly useful because they clearly demonstrate that:

- Observing peaks corresponding to f_2 and f_3 during laboratory testing is expected to be very challenging, while tracking f_1 over time would already yield a notable result.
- Tracking f_1 on Sample A is expected to be more straightforward than on Sample B, possibly due to the resonant characteristics of a columnar sample compared to a slab one.

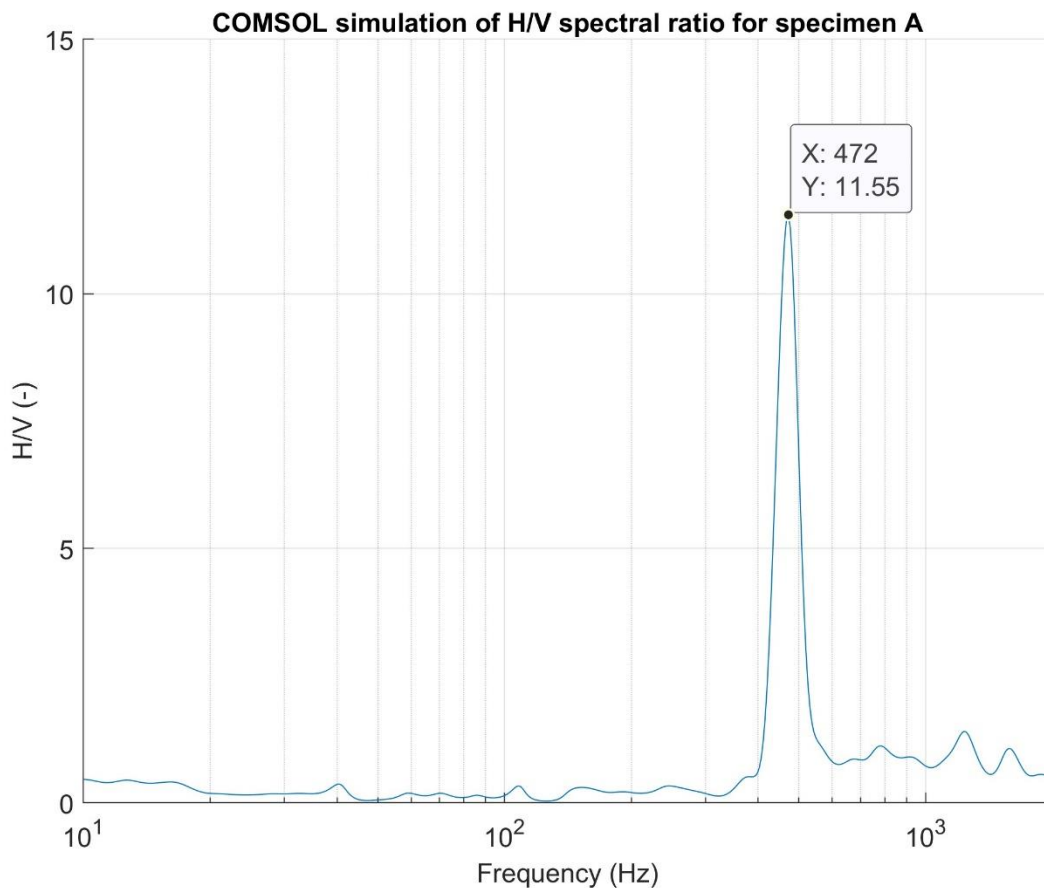


Figure 3.21 H/V simulation for Specimen A obtained with COMSOL Multiphysics.

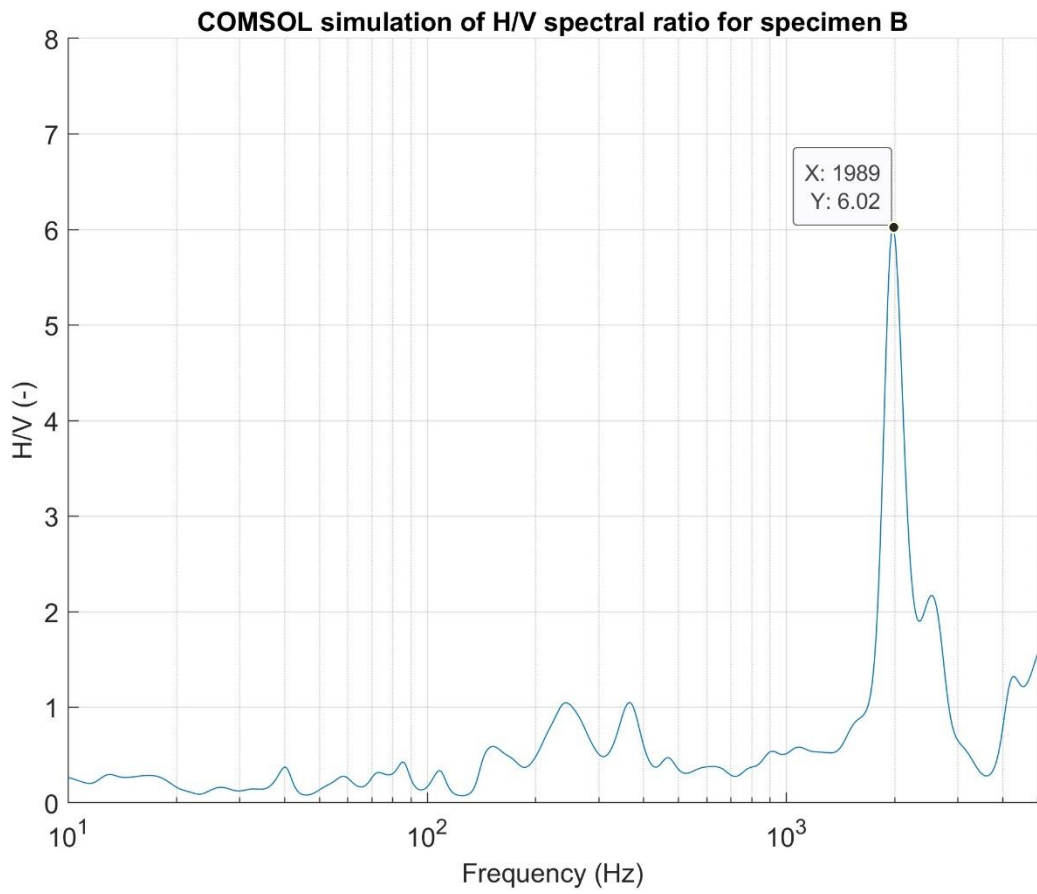



Figure 3.22 H/V simulation for Specimen B obtained with COMSOL Multiphysics.

3.4 Three-component (3C) seismic recordings at the laboratory scale

3.4.1 Description of the lab 3C seismic tests

The tests were performed with two PCB Piezotronics triaxial sensors (see Table 3.11 for technical specifications⁵).

Table 3.11 Technical specifications of the Triaxial ICP Accelerometer.

Triaxial ICP accelerometer technical specifications		
	Sensor name	TRIAxIAL ICP ACCELEROMETER
	Model	356A45
	PERFORMANCE	
	Sensitivity ($\pm 10\%$)	10.2 mV/(m/s ²)
	Measurement range	± 490 m/s ² pk
	Frequency range (+/- 5%)	0.7 to 7000 Hz
	Frequency range (+/- 10%)	0.4 to 10000 Hz
	Resonance frequency	≥ 30 kHz
	Broadband resolution	0.005 m/s ² rms
	Non-linearity	$\leq 1\%$
	Transverse sensitivity	$\leq 6\%$
	ENVIRONMENTAL	
	Overload limit (shock)	± 49050 m/s ² pk
	Temperature range	-54 to 85 °C

⁵ <https://www.pcb.com/products?m=356a45>. Last accessed 03/07/2024.

	Base strain sensitivity	.01 (m/s ²)/μϵ
	ELECTRICAL	
	Excitation voltage	20 to 30 VDC
	Constant current excitation	2 to 20 mA
	Output impedance	≤200 Ohm
	Output bias voltage	8 to 12 VDC
	Settling time (within 105 of bias)	≤5 sec
	PHYSICAL	
	Sensing element	Ceramic
	Sensing geometry	Shear
	Housing material	Titanium
	Sealing	Hermetic
	Height	10.2 mm
	Length	19.1 mm
	Width	10.2 mm
	Weight	4.2 gm

A variety of sensors configurations have been established. Figure 3.23 shows a configuration in which one sensor is positioned on the specimen and the other one on the workbench. This configuration is designed to ensure that any observed phenomena are intrinsic to the specimen.

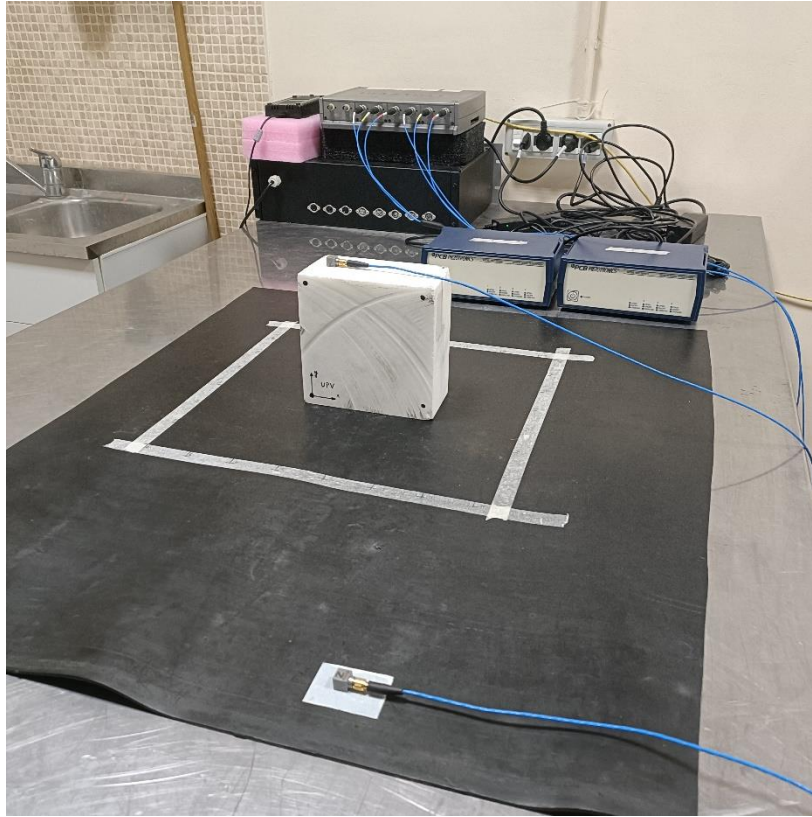


Figure 3.23 Example of laboratory setup for 3C seismic recording tests.

Both passive and active tests were performed. Passive tests were designed to detect any potential continuous vibrations around the natural resonance frequencies of the specimen. Active tests were designed to amplify the vibration intensity when the specimen was energized, thereby highlighting potential natural resonance frequencies.

The signal was acquired using the HDSL software (Golden Software), which require the definition of test and acquisition settings, including sampling frequency and full scale. A total number of 69 tests were performed, as summarized in Table 3.12.

Table 3.12 Summary of 3C seismic recordings.

Test	Specimen	A/P	Setup	SF	Full scale	Notes
1	A	Passive	Both sensors on the specimen	20 kHz	100 mV	
2	A	Active	Both sensors on the specimen	20 kHz	100 mV	
3	A	Passive	Both sensors on the specimen	20 kHz	100 mV	
4	A	Passive	Both sensors on the specimen	10 kHz	100 mV	
5	A	Active	Both sensors on the specimen	10 kHz	100 mV	
6	A	Passive	1 on the workbench, 2 on the specimen	10 kHz	100 mV	
7	A	Active	1 on the workbench, 2 on the specimen	10 kHz	100 mV	
8	A	Passive	1 on the workbench, 2 on the specimen	20 kHz	100 mV	
9	A	Active	1 on the workbench, 2 on the specimen	20 kHz	100 mV	
10	A	Passive	Both sensors on the specimen	20 kHz	100 mV	
11	A	Passive	Both sensors on the specimen	20 kHz	100 mV	
12	A	Active	Both sensors on the specimen	20 kHz	100 mV	
13	A	Passive	1 on the workbench, 2 on the specimen	20 kHz	100 mV	
14	A	Active	1 on the workbench, 2 on the specimen	20 kHz	100 mV	
15	B	Passive	1 on the specimen, 2 on the workbench	100 kHz	100 mV	
16	B	Passive	1 on the specimen, 2 on the workbench	10 kHz	100 mV	

17	B	Passive	1 on the specimen, 2 on the workbench	20 kHz	100 mV	
18	B	Active	1 on the specimen, 2 on the workbench	20 kHz	100 mV	
19	B	Passive	1 on the specimen, 2 on the workbench	20 kHz	100 mV	
20	B	Active	1 on the specimen, 2 on the workbench	20 kHz	100 mV	
21	B	Passive	1 on the specimen, 2 on the workbench	20 kHz	100 mV	
22	B	Passive	1 on the specimen, 2 on the workbench	20 kHz	100 mV	
23	B	Passive	1 on the specimen, 2 on the workbench	20 kHz	100 mV	
24	B	Passive	1 on the specimen, 2 on the workbench	20 kHz	100 mV	
25	B	Passive	1 on the specimen, 2 on the workbench	20 kHz	100 mV	
26	B	Passive	1 on the specimen, 2 on the workbench	20 kHz	100 mV	
27	B	Passive	1 on the specimen, 2 on the workbench	20 kHz	100 mV	
28	B	Passive	1 on the specimen, 2 on the workbench	20 kHz	100 mV	
29	B	Passive	1 on the specimen, 2 on the workbench	20 kHz	100 mV	
30	B	Passive	1 on the specimen, 2 on the workbench	20 kHz	100 mV	

31	B	Active	1 on the specimen, 2 on the workbench	21 kHz	100 mV	
32	B	Active	1 on the specimen, 2 on the workbench	22 kHz	100 mV	
33	B	Active	1 on the specimen, 2 on the workbench	23 kHz	100 mV	
34	B	Active	1 on the specimen, 2 on the workbench	24 kHz	100 mV	
35	B	Active	1 on the specimen, 2 on the workbench	25 kHz	100 mV	
36	B	Active	1 on the specimen, 2 on the workbench	26 kHz	100 mV	
37	B	Active	1 on the specimen, 2 on the workbench	27 kHz	100 mV	
38	B	Active	1 on the specimen, 2 on the workbench	28 kHz	100 mV	
39	B	Active	1 on the specimen, 2 on the workbench	29 kHz	100 mV	
40	B	Active	1 on the specimen, 2 on the workbench	30 kHz	100 mV	
41	B	Active	1 on the specimen, 2 on the workbench	31 kHz	100 mV	
42	B	Active	1 on the specimen, 2 on the workbench	32 kHz	100 mV	
43	-	Passive	1 on the workbench, 2 on the floor	20 kHz	100 mV	far from the fan
44	-	Passive	1 on the workbench, 2 on the floor	20 kHz	100 mV	

45	-	Passive	1 on the workbench, 2 on the floor	10 kHz	100 mV	
46	-	Passive	Both sensors on the workbench	20 kHz	100 mV	
47	-	Passive	Both sensors on the workbench	20 kHz	100 mV	
48	-	Passive	Both sensors on the workbench	20 kHz	100 mV	
49	-	Passive	Both sensors on the floor	20 kHz	100 mV	
50	A	Passive	1 on the workbench, 2 on the specimen	20 kHz	100 mV	
51	A	Passive	1 on the workbench, 2 on the specimen	20 kHz	100 mV	
52	A	Passive	1 on the workbench, 2 on the specimen	20 kHz	100 mV	
53	A	Passive	1 on the workbench, 2 on the specimen	20 kHz	100 mV	
54	A	Passive	1 on the workbench, 2 on the specimen	20 kHz	100 mV	
55	A	Active	1 on the workbench, 2 on the specimen	20 kHz	100 mV	
56	A	Active	1 on the workbench, 2 on the specimen	20 kHz	100 mV	
57	A	Active	1 on the workbench, 2 on the specimen	20 kHz	100 mV	
58	A	Active	1 on the workbench, 2 on the specimen	20 kHz	100 mV	
59	A + B	Passive	1 on top of B, 2 on top of A	20 kHz	100 mV	without amplifier
60	A + B	Active	1 on top of B, 2 on top of A	20 kHz	100 mV	

61	-	Active	Both sensors on the workbench	20 kHz	100 mV	BNC cables replaced
62	B	Active	1 on the workbench, 2 on the specimen	20 kHz	100 mV	
63	A	Active	1 on the workbench, 2 on the specimen	20 kHz	100 mV	
64	A	Active	1 on the workbench, 2 on the specimen	20 kHz	100 mV	
65	A	Active	Both sensors on the specimen	20 kHz	100 mV	
66	A	Active	Both sensors on the specimen	20 kHz	100 mV	
67	B	Active	Both sensors on the specimen	20 kHz	100 mV	
68	B	Active	Both sensors on the specimen	20 kHz	100 mV	

3.4.2 Results of the lab 3C seismic tests

For each recorded signal, the frequency spectrum and the H/V spectral ratios were computed on MATLAB. The following outputs were produced:

- Time signal trace for both sensors.
- Frequency spectrum for the whole signal.
- Frequency spectrum for each time window into which the signal was divided.
- H/V spectral ratio.

Regarding Specimen A, where the detection of f_1 was expected to be easier based on the higher simulated H/V value, the laboratory tests yielded rather disappointing results. Out of 29 tests performed on Specimen A, only four exhibited a relative maximum at f_1 that could be interpreted as the first resonance frequency. Additionally, the presence of other relative maxima complicates the detection and

interpretation of f_1 compared to the numerical H/V simulation, making it difficult to isolate a definite resonance peak. Figures 3.24 and 3.25 show the H/V plot for tests n. 56 and 58, highlighting the relative maxima around the simulated f_1 value.

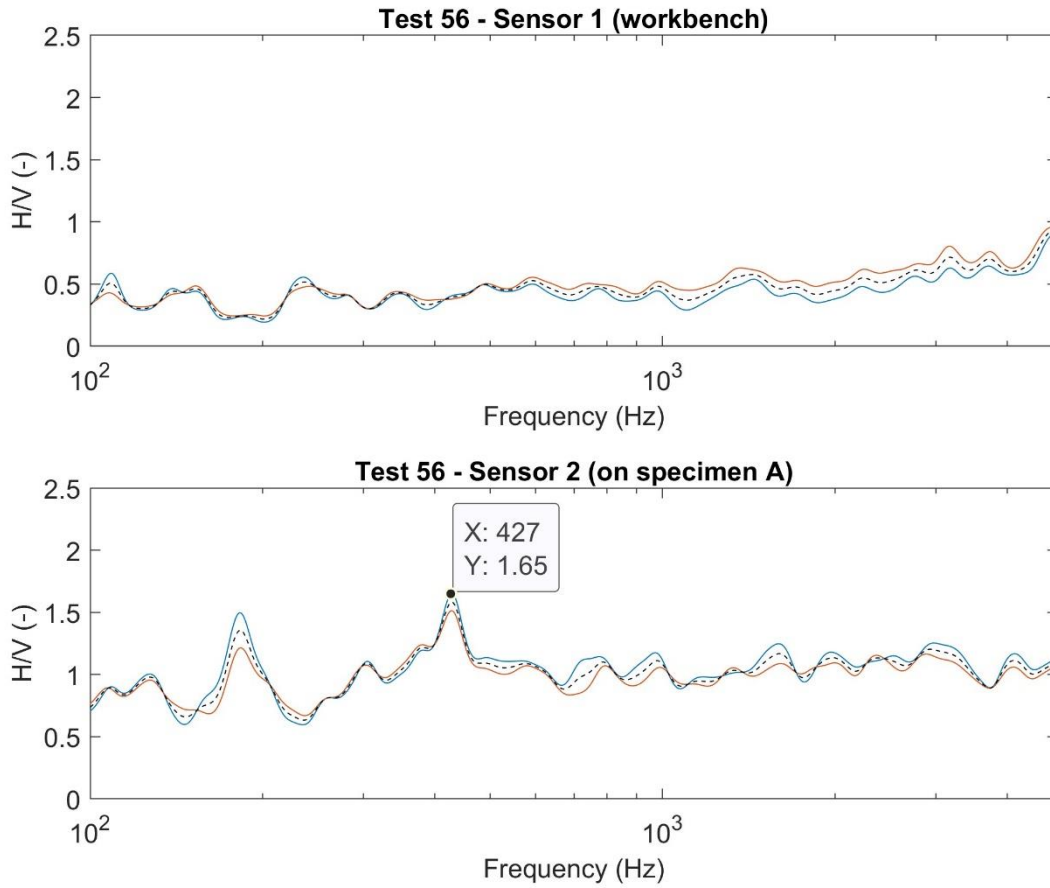


Figure 3.24 H/V plot – Test 56.

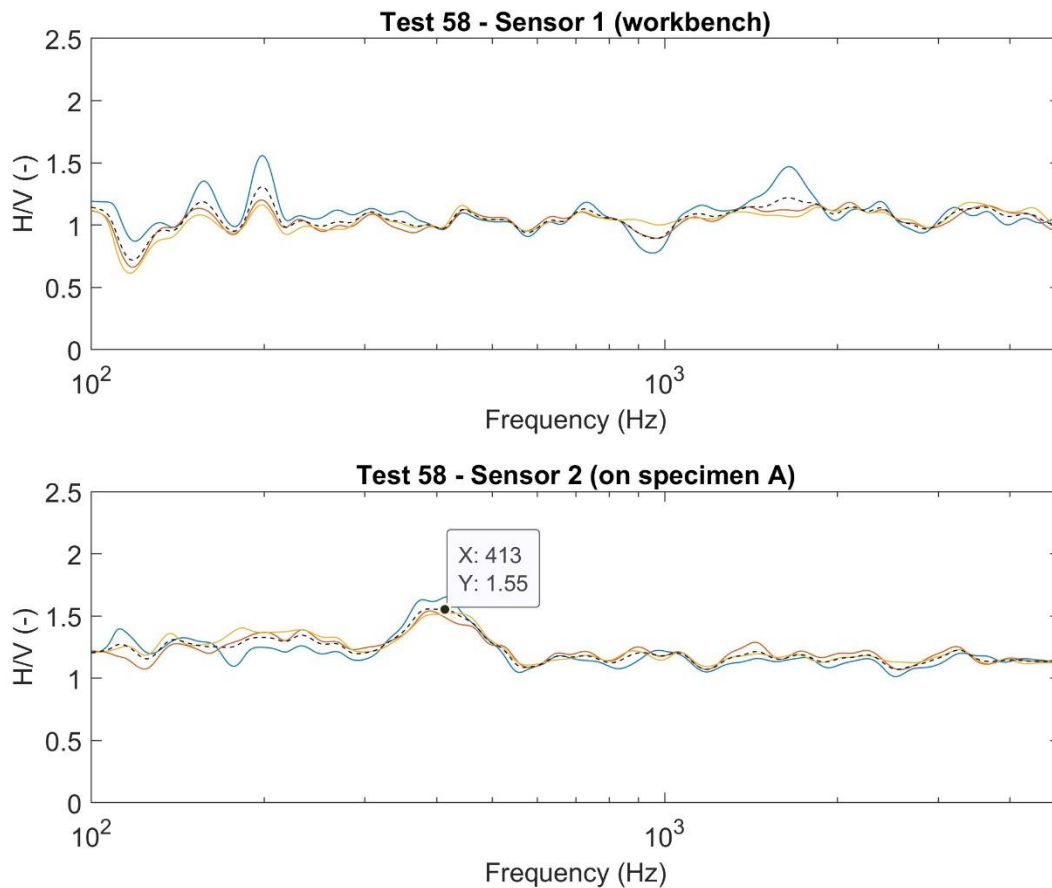


Figure 3.25 H/V plot – Test 58.

As for specimen B, an initial examination of the H/V plots consistently showed distinct peaks or dips in the 1900-2400 Hz and 3900-4400 Hz frequency ranges across the tests, with dips indicating a lower horizontal component than the vertical component and peaks suggesting the opposite. These features were initially interpreted as potentially representing the first and third resonant modes, based on their alignment with the simulated f_1 and f_3 values. However, this interpretation failed to explain why the same peaks/dips could consistently be observed regardless of the configurations, also at the sensor placed on the workbench, as shown in Figure 3.26.

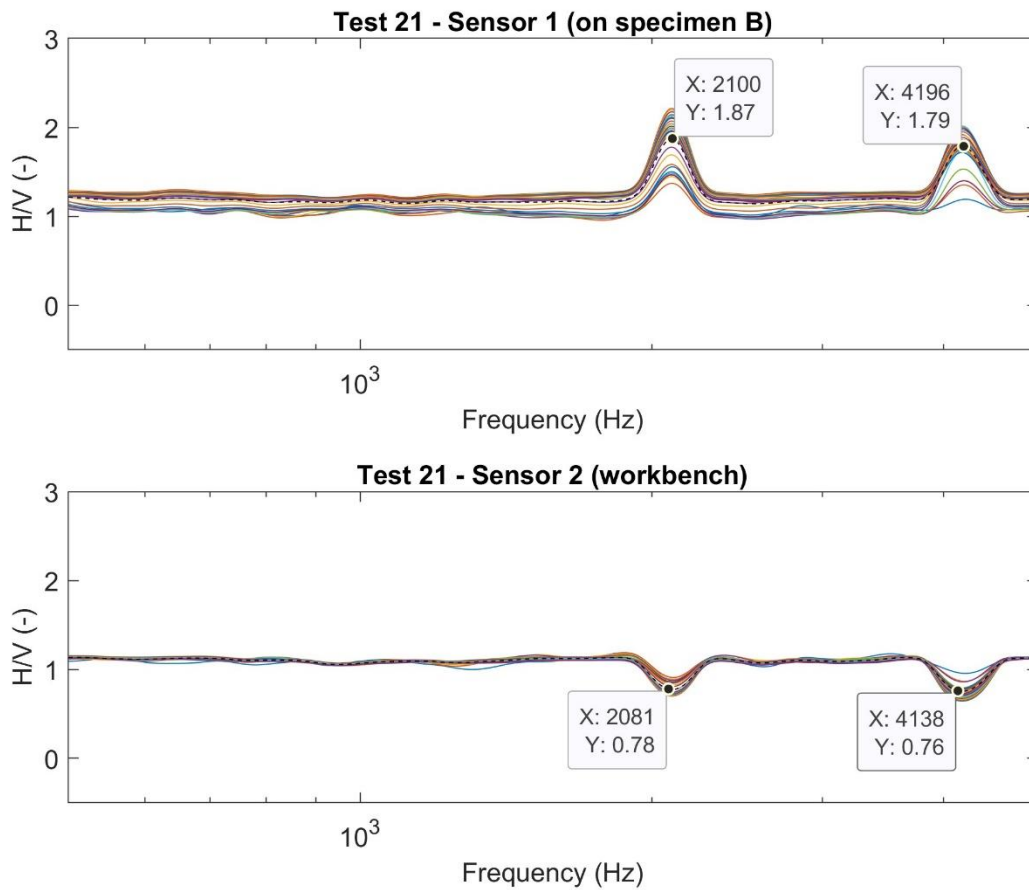


Figure 3.26 H/V plot – Test 21.

Further examination of the frequency spectra for tests performed on Specimen B identified peculiar shapes around the 1900-2400 Hz (Figure 3.28) and 3900-4400 Hz (Figure 3.29) ranges that were determined to be artifacts or noise affecting all the three components of the signal. These features were not initially detected on the spectrum due to the very low amplitude value associate to them (Figure 3.27); however, the relative values between the horizontal and the vertical components produced the maxima observed in the H/V plots (Figure 3.26).

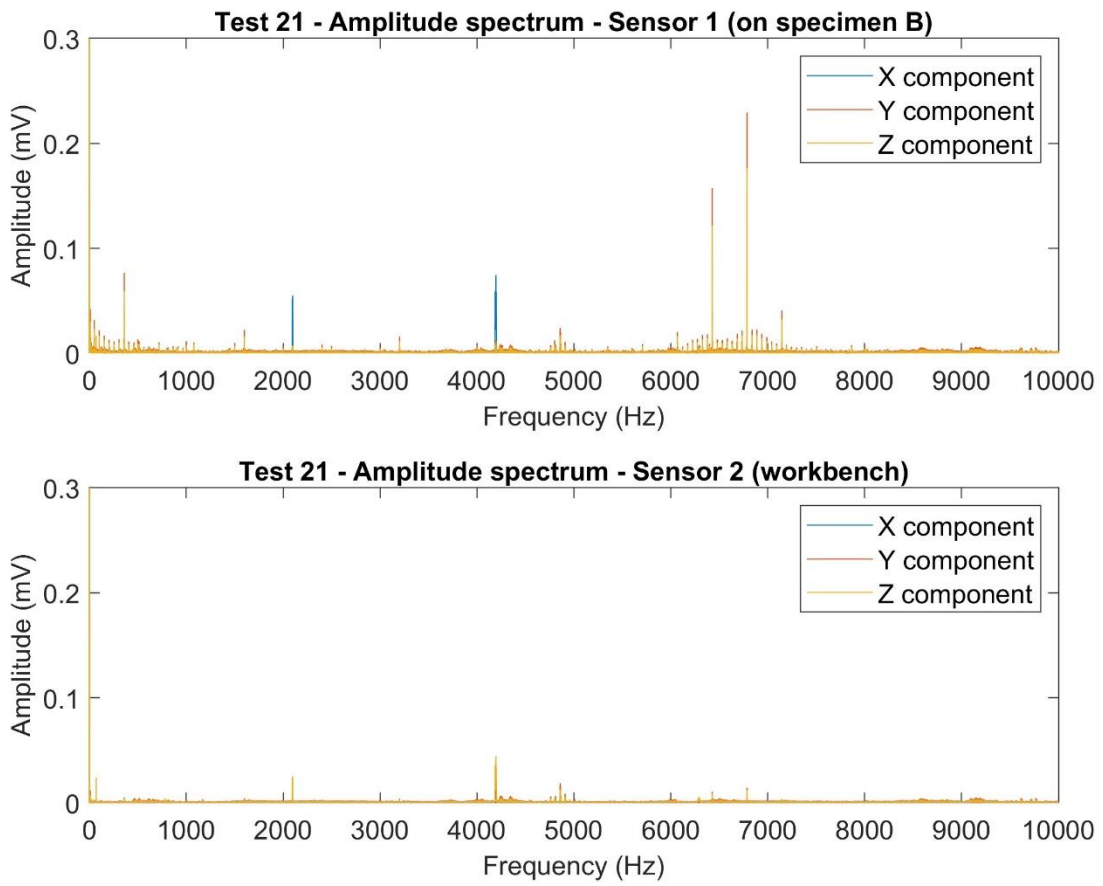


Figure 3.27 Amplitude spectrum – Test 21.

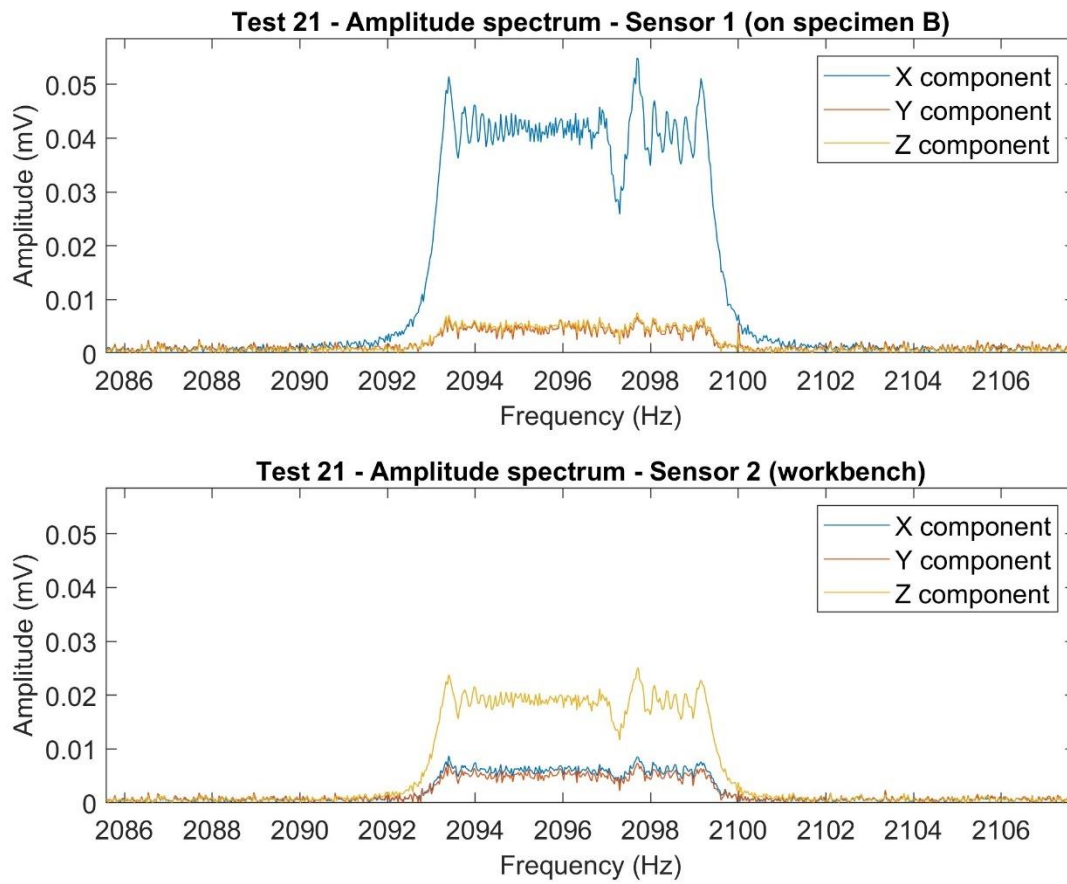


Figure 3.28 Amplitude spectrum – Test 21 – zoom around 2000 Hz.

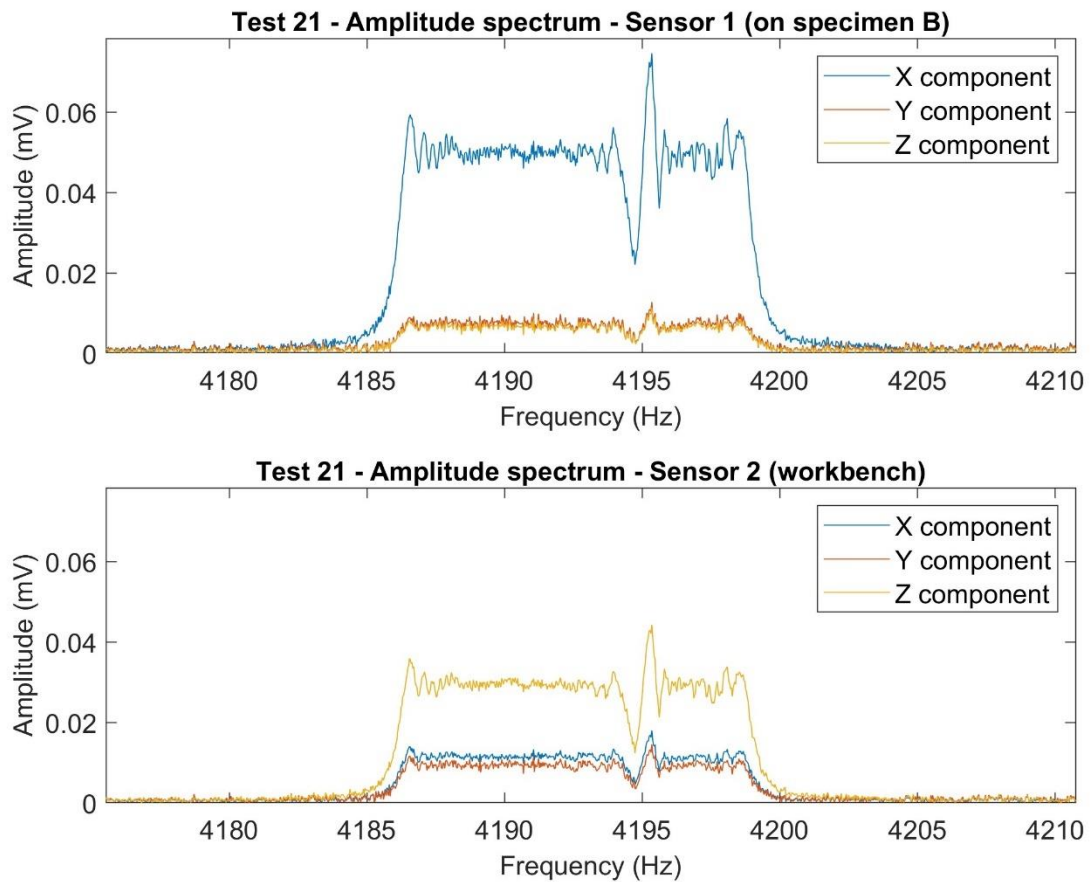


Figure 3.29 Amplitude spectrum – Test 21 – zoom around 4200 Hz.

Based on these findings, the critical regions of the spectrum were also investigated for the tests performed on Specimen A, which revealed similar features (Figure 3.30). However, for this sample, the relative values between the horizontal and the vertical components did not produce consistent peaks or dips in the H/V plot.

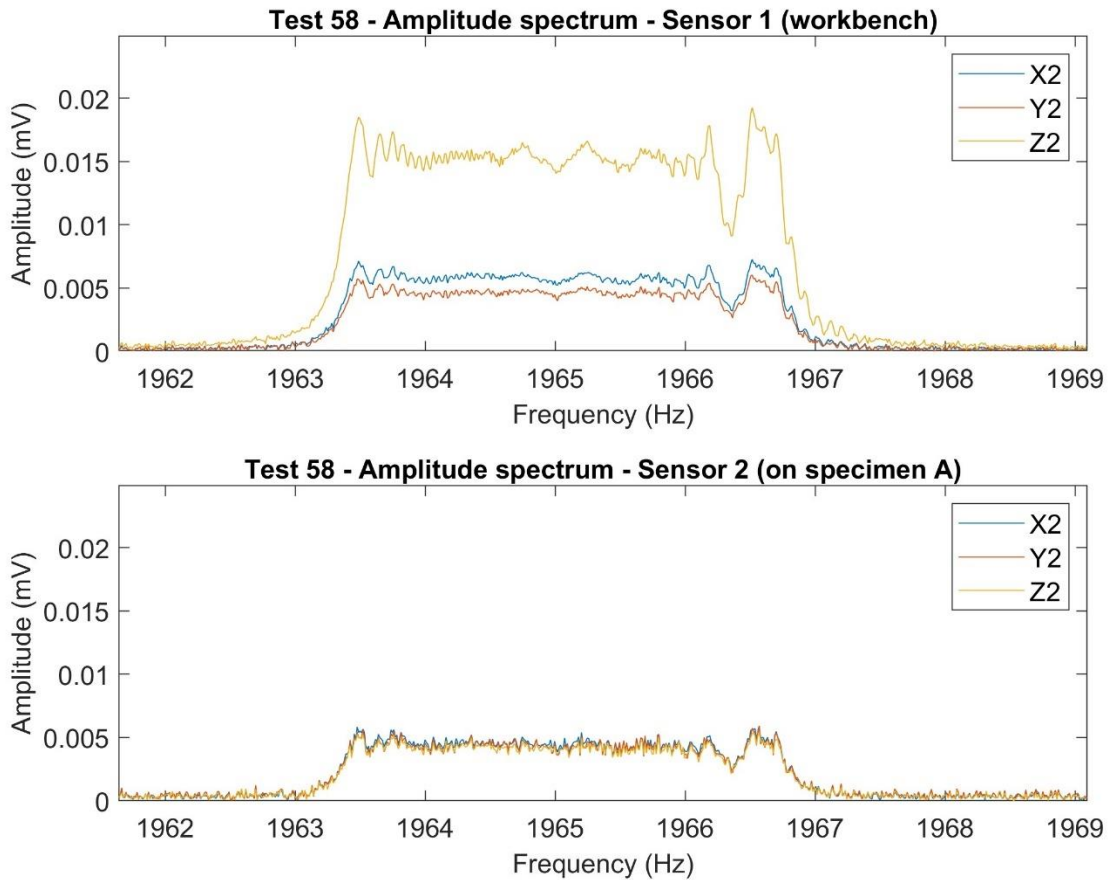


Figure 3.30 Amplitude spectrum – Test 58 – zoom around 1965 Hz.

These findings indicate that the observed peaks and dips in the H/V plots are unlikely to represent natural resonance frequencies, prompting further investigation into their origins. Moreover, the presence of this noise in specific frequency ranges poses a significant challenge, potentially obscuring the true resonance frequencies of the specimens. This is particularly relevant for Specimen B, where numerical simulations indicated resonance values in the range of these perturbations. Consequently, eliminating these disturbances or conducting analysis outside of the critical frequency ranges is crucial for an accurate assessment of the resonant behavior of the samples.

Several hypotheses have been explored to explain the observed peaks and dips, including:

- Ambient noise from the motherboard fan.
- Sensor characteristics.
- Amplifier issues.
- Cable obsolescence.

Extended tests were then performed to investigate each hypothesis separately and ultimately confirm or reject them. Tests n. 43-49 were performed with both sensors placed on the floor to evaluate the effect of ambient noise from the motherboard placed in the corner of the workbench. Despite this adjustment, the interference persisted (Figure 3.31), indicating that it was not due to ambient noise in the laboratory.

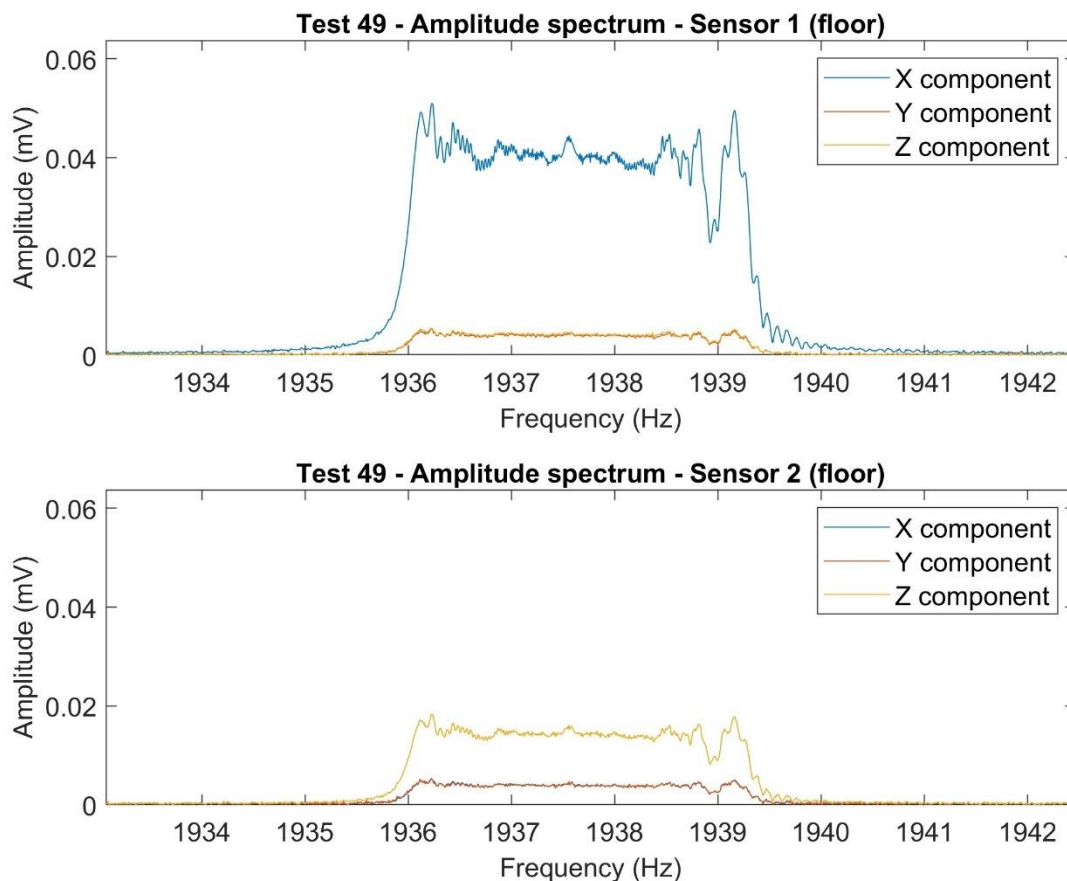


Figure 3.31 Amplitude spectrum – Test 49 – zoom around 1935 Hz.

Tests n. 59-60 were performed without the amplifiers, with the sensors connected directly to the motherboard, to see if the amplifiers had any noticeable effect on the spectral content of the signal. Once again, the interference persisted (Figure 3.32), leading to the conclusion that the hypothesis attributing its origin to intrinsic amplifier characteristics must be rejected.

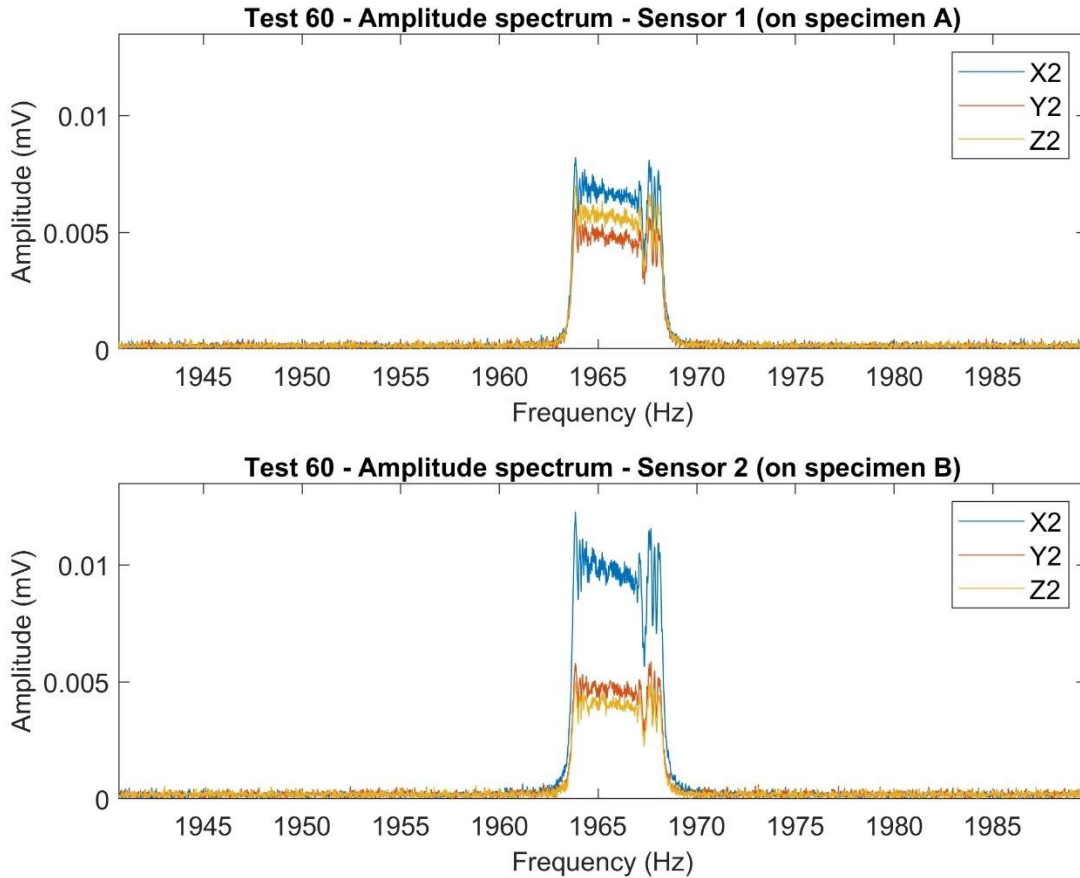


Figure 3.32 Amplitude spectrum – Test 60 – zoom around 1665 Hz.

Tests n. 61-68 were performed after replacing the BNC cables connecting the amplifiers to the motherboard with a brand-new set. The purpose of this step was to evaluate the hypothesis of a possible effect due to the obsolescence of the cables. Despite this change, the interference persisted in the frequency spectrum. However, the replacement of all the BNC cables proved effective in mitigating the problem by equalizing the amplitude of the three noise components (Figure 3.33) so that the H/V

value remained around 1 and the dips and peaks in the H/V plot disappeared. Consequently, this adjustment may allow the identification of potential resonance frequencies in the H/V spectral ratio plot, provided that they do not interfere with the critical ranges.

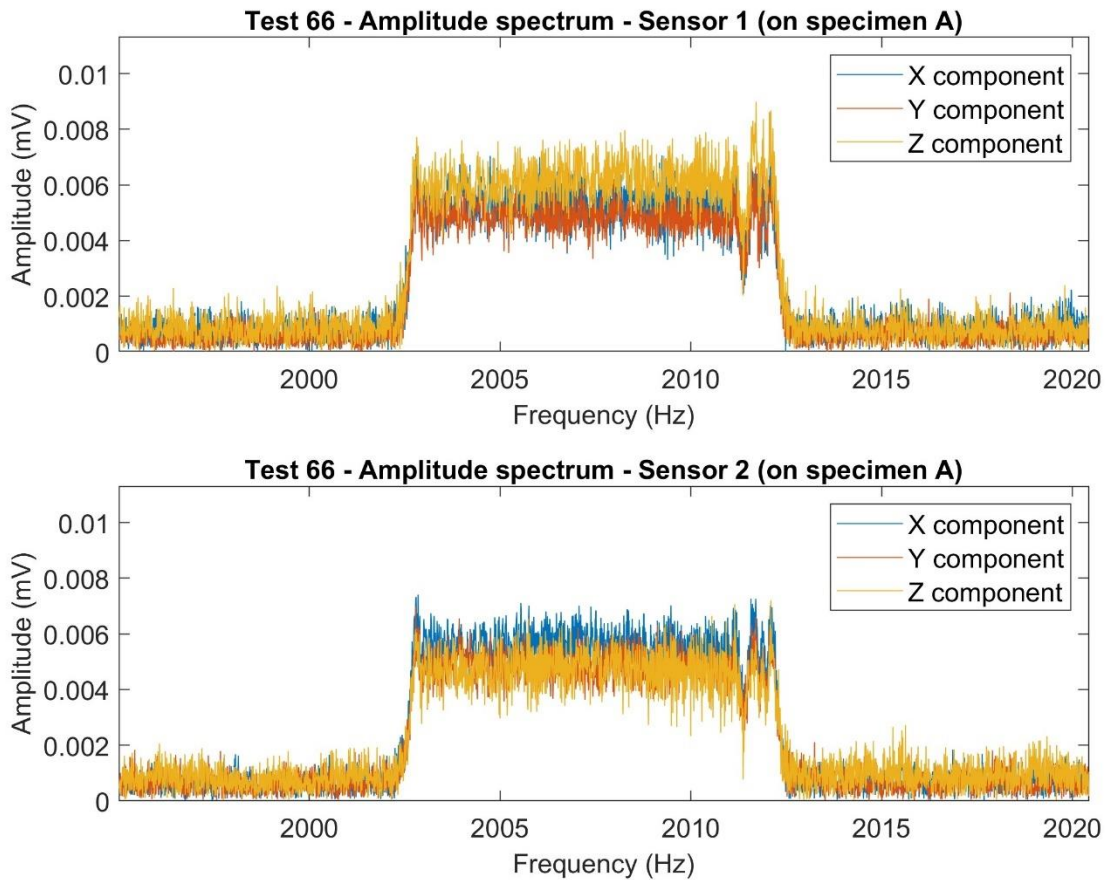


Figure 3.33 Amplitude spectrum – Test 66 – zoom around 2010 Hz.

3.4.3 Insights and implications from the lab 3C seismic tests

FEM modeling proves valuable in guiding the interpretation of laboratory results, as it enables the prediction of the appropriate ranges for potential resonance frequencies. This focused approach increases the likelihood of identifying resonance frequencies, as demonstrated with Specimen A, which exhibited some relative

maxima at approximately 430 Hz in a few of the tests. These results could only be interpreted as f_1 due to the reference simulations.

Analysis of the 3C seismic recordings for Specimen A and Specimen B revealed perturbations within the frequency spectrum, manifested as distinct frequency peaks or dips within the 1900-2400 Hz and 3900-4400 Hz frequency ranges in the H/V spectral ratio plot. However, there was no consistent explanation for the occurrence of dips or peaks across different test configurations. Despite attempts to mitigate this noise by changing experimental conditions, including sensor placement, amplifier removal, and BNC cable replacement, the noise persisted. However, replacing all of the BNC cables proved successful in alleviating the problem by equalizing the amplitude of all three noise components and eliminating peaks and dips in the H/V plot.

Nevertheless, the presence of spectral noise indicates a challenge in accurately identifying potential resonance frequencies within the noise regions. This is particularly problematic for Specimen B, where the spectral noise interferes with the detection of potential resonance frequencies because both f_1 and f_3 fall exactly within the noisy range according to FEM simulation.

Additionally, the slab shape of Specimen B is expected to produce lower H/V values compared to the column-shaped Specimen A, as demonstrated by numerical simulations. Consequently, even if the natural resonance frequencies of Specimen B were not situated within the noisy regions, they might still be challenging to detect, since the resonance frequencies of Specimen A were already difficult to discern despite the higher expected H/V values.

The shape, dimensions, and characteristics of Specimen B render it unsuitable for analysis with the available sensors. This limitation underscores the importance of selecting appropriate specimens for laboratory 3C seismic tests to avoid interference from instrumentation-induced noise and to maximize the resonant response. Further work should involve the use of rock samples with simulated resonance frequencies much below 1900 Hz and a column-like shape, which should

amplify the oscillatory behavior. Such samples may circumvent the aforementioned challenges and facilitate frequency identification. In this regard, it is recommended that numerical modeling be employed to inform sample preparation.

3.5 Designing future specimens using FEM simulation

3.5.1 Objectives of the design process

Building upon the data gathered from numerical simulations and laboratory testing of Specimen A and Specimen B, the objective now is to propose an optimal design for a new specimen. This specimen will be utilized in subsequent phases of the *THEROCKLAB* PRIN project. Preliminary laboratory scale investigations on intact specimens yielded several key insights:

- **Software Consistency:** The results demonstrated a high level of consistency between the two software packages, COMSOL Multiphysics and GTS NX.
- **Eigenfrequency Alignment:** There was a strong agreement between the eigenfrequency results and the simple oscillator model described by Equation 2.1.
- **Resonant Responses:** The H/V plots revealed distinct resonant responses influenced by the geometry of the specimens.
- **Instrument Limitations:** The available instrumentation was unable to investigate the critical frequency ranges (1900-2400 Hz and 3900-4400 Hz) due to systematic noise.

The finite element method (FEM) should be employed to design a new specimen that incorporates these findings and considers future steps of the *THEROCKLAB* project. In particular, the transition from intact samples to samples with artificial fractures is of interest, as this will simulate the presence of fractures in real rock slopes. Furthermore, the project aims to evaluate the impact of external thermo-

hydro factors, such as water infiltration and thermal cycling, on the stability of rock masses. These conditions should be replicated under controlled laboratory settings, such as the simulation of water and ice filling fractures and the conduct of freeze-thaw cycles within a cold chamber.

This section presents the results of FEM simulations on various cut geometries to examine the trends in resonance frequencies as the cut geometry varies. The objective is to identify the most suitable sample for future laboratory scale studies.

The investigation began with the identification of two distinct intact geometries: a column and a slab, designated as Specimen C and Specimen D, respectively. The samples were designed to have identical height and depth dimensions, differing only in width, as detailed in Table 3.13. The elastic material properties of both samples were defined consistently using marble as the selected material. The parameters for marble were derived from the sample characterization described in Section 3.1.4.

Table 3.13 Dimensions of Specimen C and Specimen D.

	Specimen C	Specimen D
Width (X)	10 cm	40 cm
Depth (Y)	10 cm	10 cm
Height (Z)	30 cm	30 cm

A systematic approach was employed to isolate an element of the sample and simulate an unstable compartment mimicking real-site conditions but on a laboratory scale. A 30° inclined section, 5 mm thick, of increasing length was created (see Table 3.14 and Figure 3.34). The cut was 10 cm wide, matching the shorter side of the cross-section of both specimens, and started 2.3 cm from the edge on the top face of the sample. This method ensured that, for any given cut length, the volume of the isolated sector remained consistent between both specimens. This approach allows for determining whether and how the overall geometry of the rock block influences the resonant behavior when the unstable volume is the same. It is anticipated that as the cut length increases, the oscillation will predominantly

involve only the isolated sector, resulting in the two specimens exhibiting similar resonance frequencies. Conversely, as the cut length decreases, it is anticipated that the overall geometry will have a more significant impact on the resonant behavior. Consequently, greater differences in resonance frequencies between the two specimens are expected, with Specimen D displaying lower frequencies than Specimen A due to its greater mass.

Table 3.14 Cut lengths (in cm) for eigenfrequency simulations of Specimen C and Specimen D.

	Length 0	Length 1	Length 2	Length 3	Length 4
Cut length (cm)	0	3.1	7.1	11.1	15.1

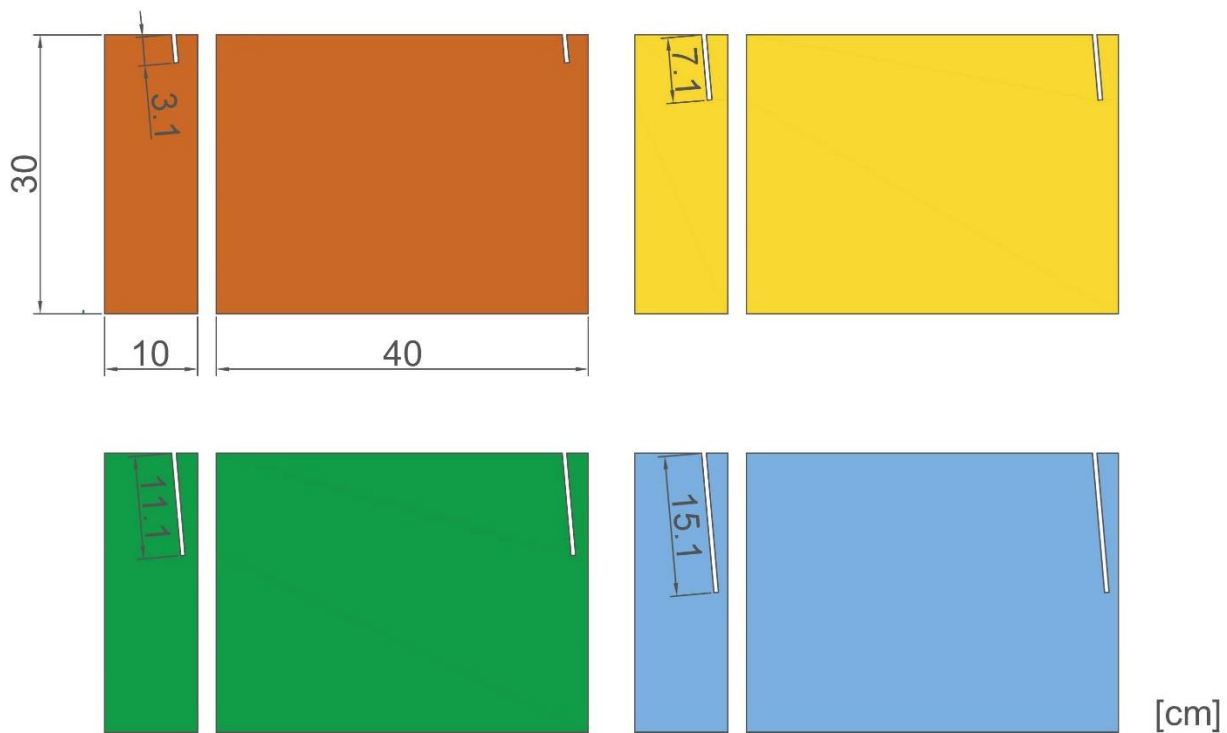


Figure 3.34 Cut configurations for Specimen C and Specimen D.

In addition, two fixed constraint configurations were evaluated (Figure 3.35): Mode 1 involved constraining solely the base, while Mode 2 included constraints on the base, one side, and the top surface. Mode 2 was introduced to further isolate the

unstable sector, thereby enhancing the isolation effect. It is anticipated that Specimens C and D will exhibit more similar resonance frequencies under Mode 2, as the oscillating portion of the block will be nearly identical, and the overall constrained geometry of the block will have a reduced influence.

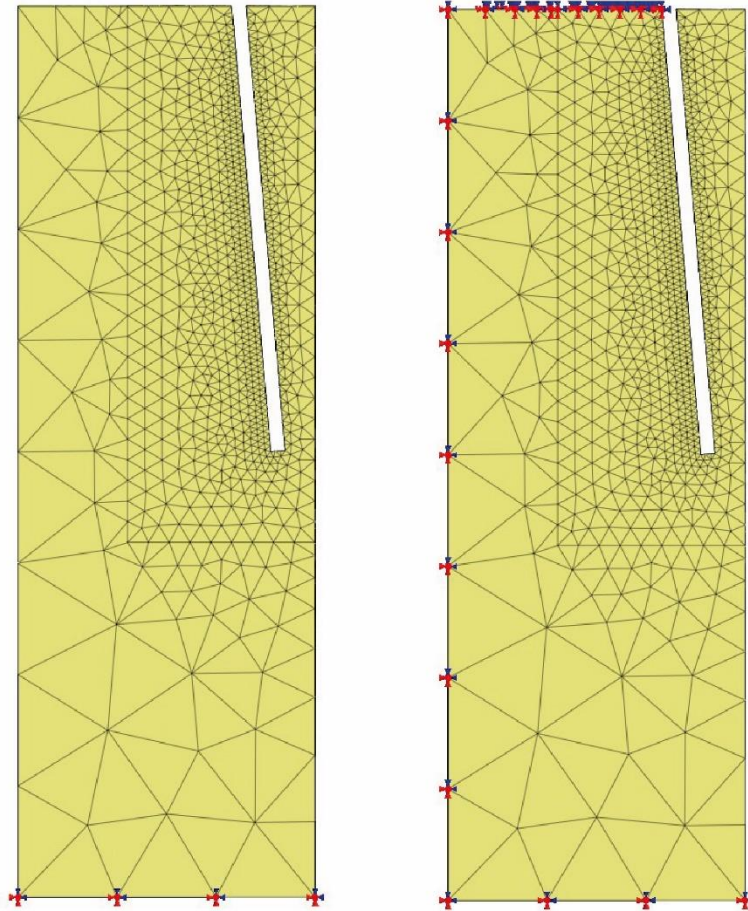


Figure 3.35 Representation of Constraint Mode 1 and Constraint Mode 2.

3.5.2 Simulation results

The results of the eigenfrequency simulation conducted on GTS NX are reported in Table 3.15 and Table 3.16.

Table 3.15 Eigenfrequency simulation results (Constraint Mode 1) for Specimen C and D using GTS NX.

	Constraint Mode 1									
	Length 0		Length 1		Length 2		Length 3		Length 4	
	C	D	C	D	C	D	C	D	C	D
$f_1(Hz)$	673	806	536	696	531	651	427	483	203	209
$f_2(Hz)$	716	1187	544	1104	543	1051	534	623	533	643
$f_3(Hz)$	1925	1370	1560	1180	1333	1125	625	1002	574	870
$f_4(Hz)$	2509	2514	2330	2214	1525	1315	1353	1190	861	944

Table 3.16 Eigenfrequency simulation results (Constraint Mode 2) for Specimen C and D using GTS NX.

	Constraint Mode 2									
	Length 0		Length 1		Length 2		Length 3		Length 4	
	C	D	C	D	C	D	C	D	C	D
$f_1(Hz)$	4042	2445	3824	2372	1254	1251	470	484	205	209
$f_2(Hz)$	5634	3236	4658	3147	2569	2106	1426	1440	863	869
$f_3(Hz)$	6365	3332	4843	3326	2682	2564	1608	1527	1002	985
$f_4(Hz)$	7737	4661	6133	4244	4056	2758	3288	2395	1748	1783

The following observations can be derived from the results:

- Specimens with full constraints consistently exhibited higher resonance frequencies than those with only base constraints. This observation is consistent with Equation 2.1: Constraint Mode 2, which allows only the

isolated unstable part to move, involves a significantly smaller mass than Constraint Mode 1.

- The resonance frequencies exhibited a consistent decrease with increasing cut depth. This observed trend aligns seamlessly with the theoretical framework encapsulated in Equation 2.1. As the cut depth increases, the dimension of the unstable compartment increases correspondingly, leading to the expectation of a decreased resonance frequency. The only values that do not respect this expected trend are the f_2 values for Specimen D at Length 4 and Length 3 in Constraint Mode 1, which show an inversed trend.
- The anticipated decrease in percent error between Specimen C and Specimen D, as a function of increasing cut length, is generally confirmed by the results of the numerical simulations, despite some notable discrepancies (see Table 3.17 and Table 3.18 below). Focusing on the first resonance frequency (f_1), which is of primary interest for this study, the anticipated trend is confirmed: f_1 tends to converge to the same value as the cut length increases. However, under Constraint Mode 2, the f_1 values already converge at Length 2, whereas, for Constraint Mode 1, the maximum cut length is required to observe this convergence. Additionally, for Constraint Mode 1, the percent error at Length 0 slightly contradicts the expected behavior. Nevertheless, this does not impact the overall conclusion that a significant cut length is necessary for the f_1 value to depend solely on the volume of the unstable sector.

Table 3.17 Percent error in eigenfrequency values between Specimen C and D as function of the cut length – Constraint Mode 1.

Percent Error - Constraint Mode 1					
	Length 0	Length 1	Length 2	Length 3	Length 4
f_1	19.7%	29.7%	22.6%	13.2%	2.9%
f_2	65.8%	102.8%	93.6%	16.7%	20.7%
f_3	40.5%	32.2%	18.5%	60.5%	51.7%
f_4	0.2%	5.2%	15.9%	13.7%	9.6%

Table 3.18 Percent error in eigenfrequency values between Specimen C and D as function of the cut length – Constraint Mode 2.

Percent Error - Constraint Mode 2					
	Length 0	Length 1	Length 2	Length 3	Length 4
f_1	65.3%	61.2%	0.2%	3.0%	1.9%
f_2	74.1%	48.0%	22.0%	1.0%	0.6%
f_3	91.0%	45.6%	5.6%	5.3%	1.7%
f_4	66.0%	44.5%	47.1%	37.3%	2.0%

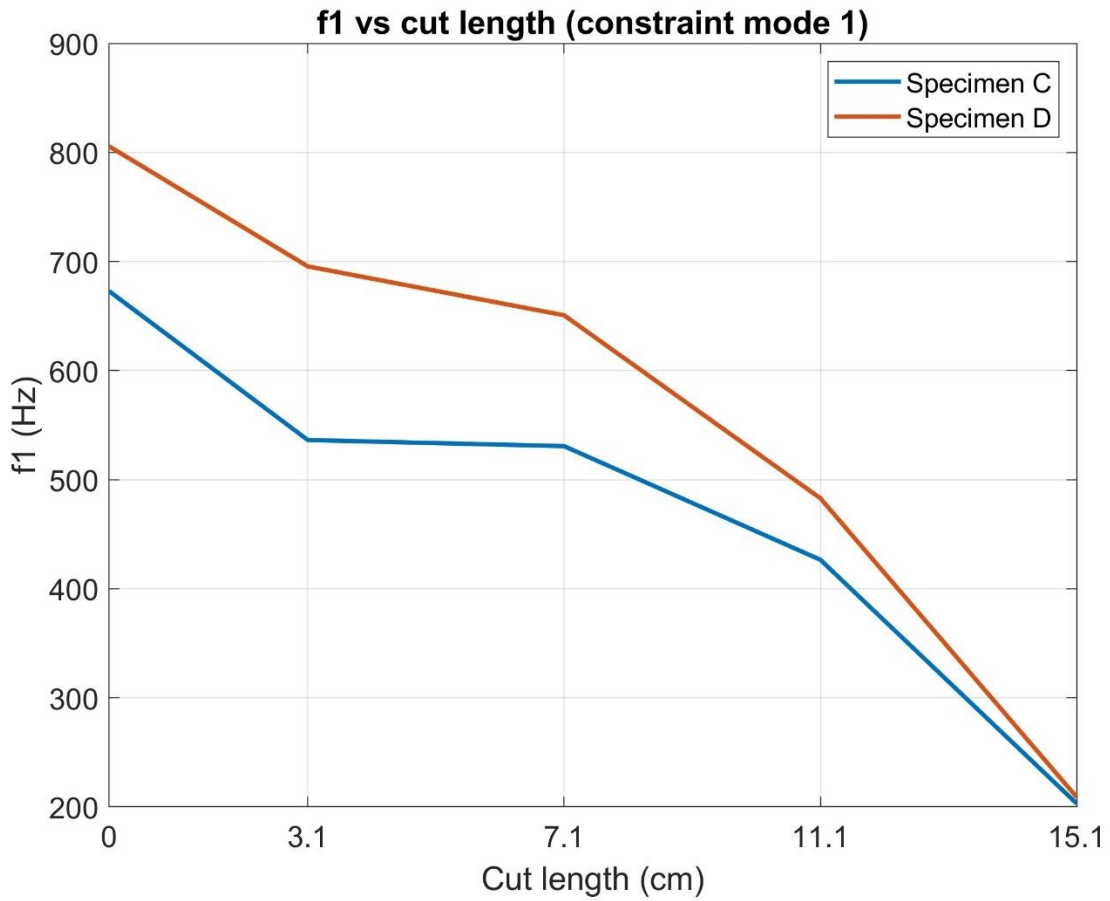


Figure 3.36 f_1 value variations with cut length for Specimen C and Specimen D – Constraint Mode 1.

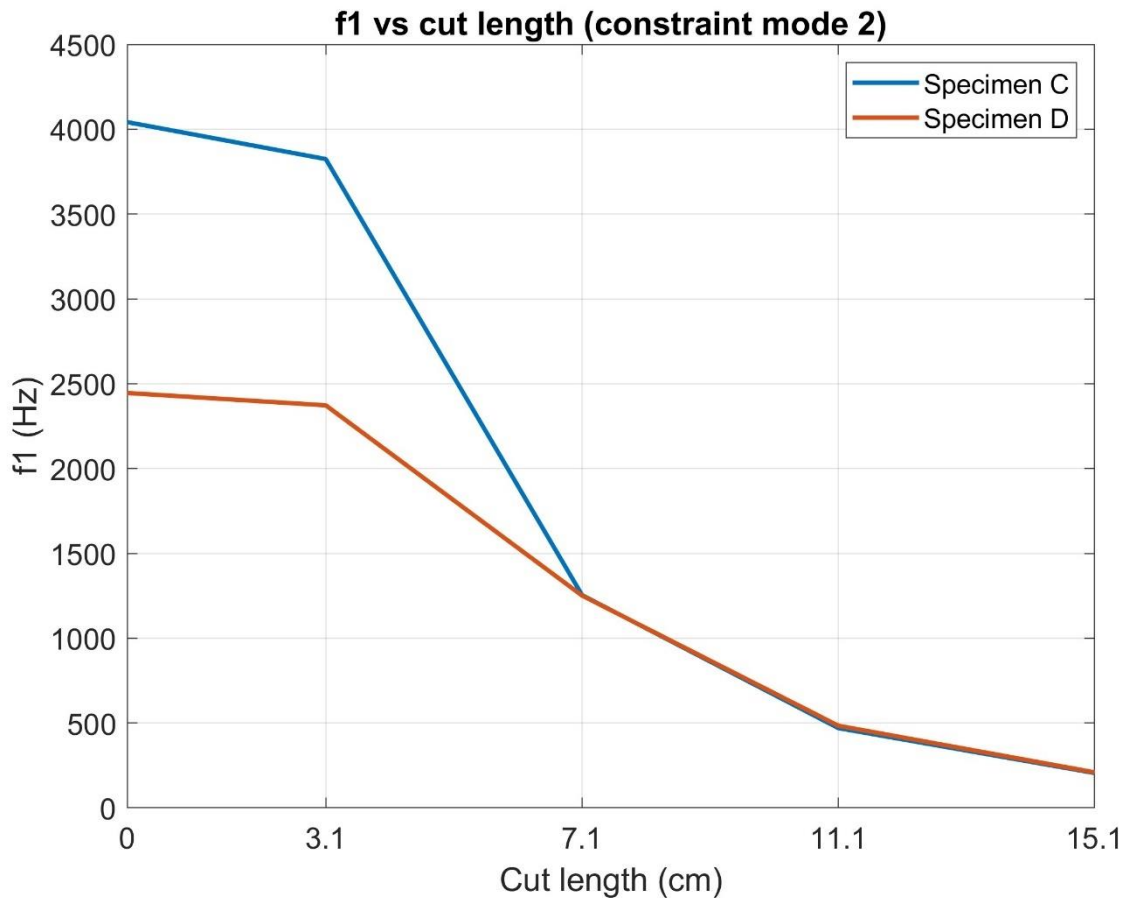


Figure 3.37 f_1 value variations with cut length for Specimen C and Specimen D – Constraint Mode 2.

Regarding the eigenmodes, no discernible pattern emerges from the numerical simulations. Neither between the two specimens for the same cut length nor within the same specimen for different cut lengths does a clear pattern emerge. For the intact blocks, both specimens exhibit bending at f_1 and f_2 , and torsion at f_3 .

In Constraint Mode 2, at Length 1, the oscillatory behavior of the unstable sector is not clearly isolated, exhibiting a mix of bending and torsional modes involving larger parts of the block. When focusing on the first eigenmode, which is of primary interest, it consistently shows bending of the unstable sector perpendicular to the fracture across all cut lengths, with the exception of Length 1. As for higher modes, at Length 2, Specimen C exhibits torsion at f_2 and bending parallel to the fracture at f_3 , whereas Specimen D shows the opposite behavior. The eigenmodes

observed at Length 3 and 4 are highly consistent: the f_1 eigenmode corresponds to bending perpendicular to the fracture, the f_2 eigenmode to torsion around the vertical axis, and the f_3 eigenmode to bending parallel to the fracture. Overall, the bending eigenmodes at Length 2, 3, and 4 align with findings in the literature on site-scale studies, where the first bending mode is consistently perpendicular to the fracture and the second is parallel.

The situation is more complex for Constraint Mode 1. Specimen C at Length 1 exhibits the same eigenmodes as at Length 0, indicating that the cut has little influence on the resonant behavior due to its short length. However, Specimen D at Length 1 shows torsion at f_2 and bending at f_3 , contrary to the intact specimen. At Length 2, the oscillation of only the unstable sector is observed at f_3 , whereas f_1 and f_2 correspond to the same eigenmodes as Length 1. When Length 3 or higher is reached, the oscillation of the unstable sector is already isolated at f_1 for both specimens, and especially for Length 4. Additionally, f_2 corresponds to bending of the entire block perpendicular to the longer side for both specimens. As the modes of oscillation further increase, the consistency between the two specimens is lost. Specimen D exhibits torsion at f_3 , while Specimen C exhibits torsion at f_4 and another bending mode involving the entire block at f_3 .

The results of the FEM simulations described in this section indicate that the recommended design for a new specimen for *THEROCKLAB* laboratory scale activities is Specimen C with Length 4 as cut geometry. This is based on the following reasons:

- Isolation of Unstable Sector: Length 4 ensures that at f_1 only the unstable sector oscillates, even under Constraint Mode 1, regardless of the geometry of the rest of the block. This better simulates field conditions, where the focus is on the stability of the unstable compartment. The analysis is limited to f_1 , as previous laboratory scale testing indicated that tracking f_1 would be a significant achievement, while tracking higher modes is highly unlikely.

- Operational Efficiency: Since at Length 4 only the unstable sector oscillates, it is preferable to work with the column shape of Specimen C, as its volume and weight are four times lower than Specimen D. This makes it easier to handle in the laboratory.
- Frequency Range: The simulated eigenfrequency values ensure that the investigated frequency range is much lower than the critical ranges of 1900-2400 Hz and 3900-4400 Hz.

The recommended design will be referred to as Specimen C4. For this design, the eigenfrequency analysis has been repeated using COMSOL Multiphysics to further assess the consistency of the two FEM software packages. Here the percent error is slightly higher than those obtained for the intact Specimen A and B, reaching up to 13.4% percent (Table 3.19). However, the systematically higher values of GTS NX and the full consistency of the simulated eigenmodes between the two software allow to confirm the reliability and validity of eigenfrequency simulations performed.

Table 3.19 Percent error in eigenfrequency between GTS NX and COMSOL Multiphysics for Specimen C4.

	GTS NX	COMSOL	Percent Error
f_1	203 Hz	179 Hz	13.4%
f_2	533 Hz	505 Hz	5.5%
f_3	574 Hz	547 Hz	4.9%
f_4	861 Hz	762 Hz	13%

Additionally, a simulation of the H/V spectral ratios was performed considering three points on the top surface of the specimen (Figure 3.38):

- Stable sector: central point of the stable sector.
- Unstable sector, midpoint: central point of the unstable sector.
- Unstable sector, edge: 1 cm from the edge of the specimen.

The H/V plots have been examined close to the eigenmodes to facilitate interpretation (Figure 3.39).

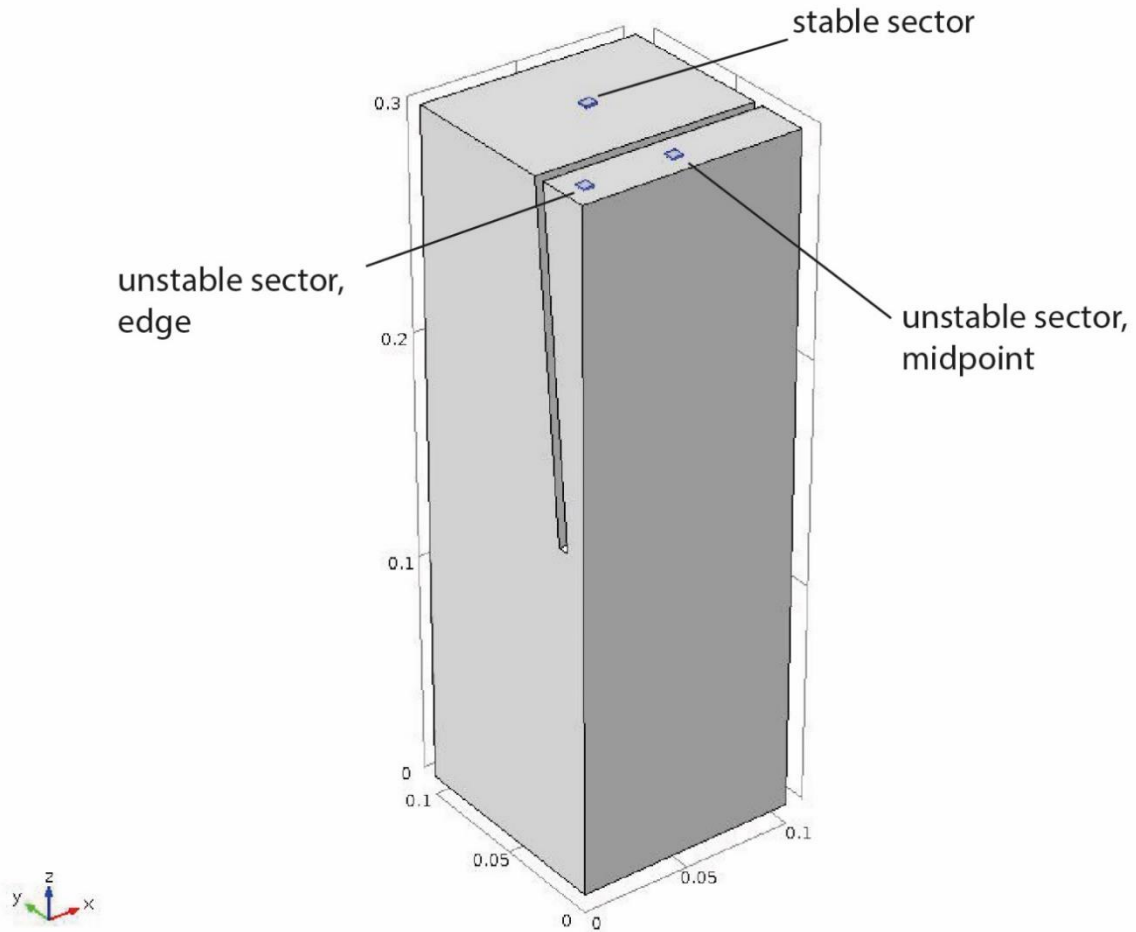


Figure 3.38 Location of the three points considered to perform the H/V simulation with COMSOL Multiphysics for Specimen C4.

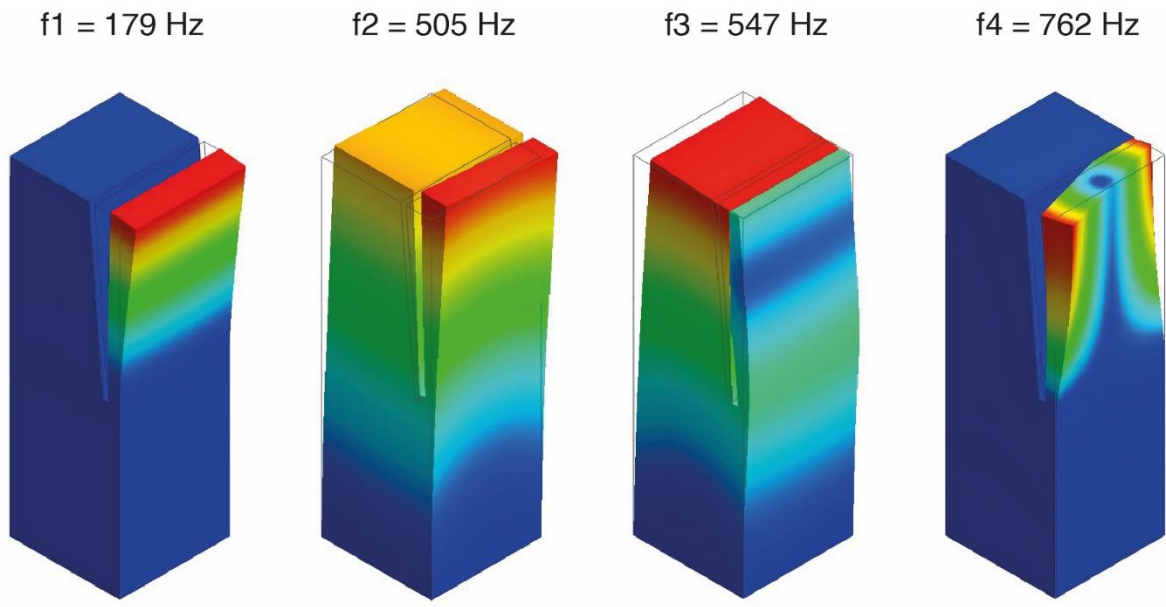


Figure 3.39 Eigenmode displacement visualization for Specimen C4.

As expected, the H/V plot related to the stable sector does not show a peak at f_1 or f_4 , since these resonant modes involve only the unstable sector. It shows a peak at about 531 Hz, which can be interpreted as the bending modes corresponding to f_2 and/or f_3 (Figure 3.40).

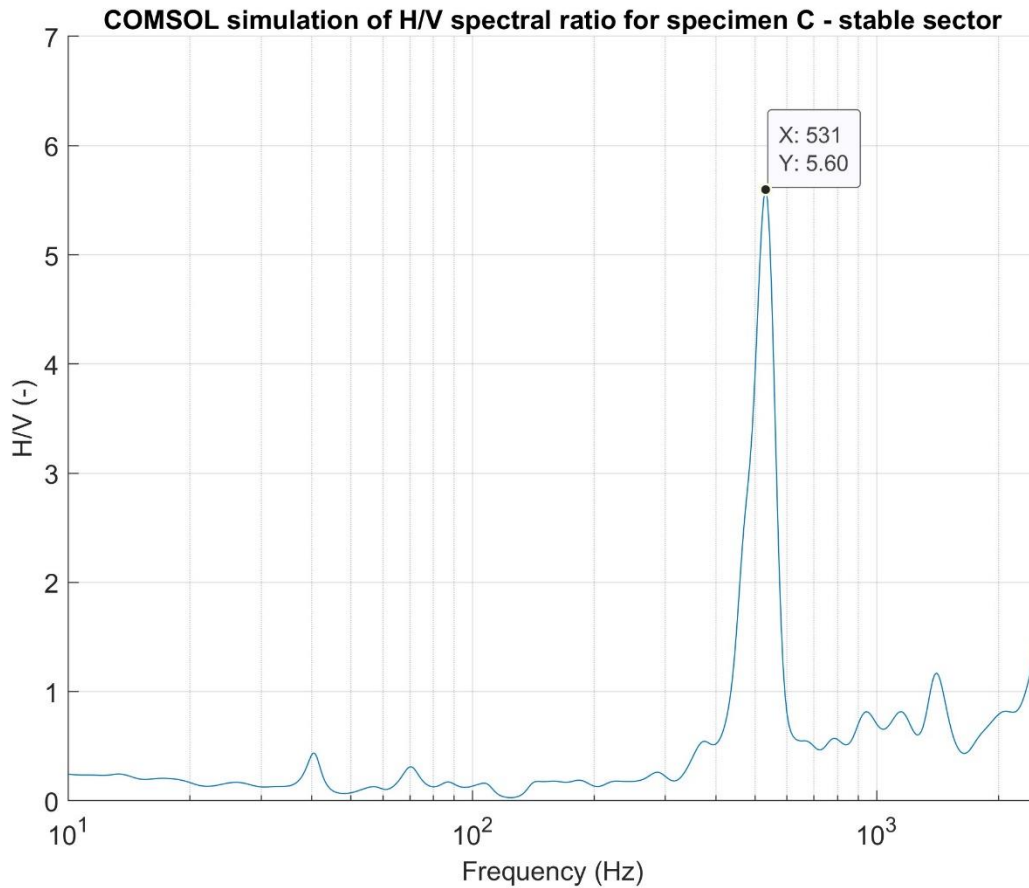


Figure 3.40 H/V simulation for Specimen C4 (stable sector) obtained with COMSOL Multiphysics.

The H/V plots for the unstable sector (Figure 3.41 and Figure 3.42) exhibit a peak corresponding to f_1 , which aligns with the simulated first eigenmode, indicating a bending of only the unstable part. Additionally, these plots display another peak at approximately 480 Hz, which may correspond to f_2 and/or f_3 . With regard to the torsion mode at f_4 , the H/V plot for the edge point exhibits a relative maximum at approximately 708 Hz (Figure 3.42), which is not present at the midpoint of the unstable part (Figure 3.41). This result is consistent with the simulated displacement, as the midpoint of the unstable sector is on the rotation axis and, therefore, is not expected to undergo any displacement, in contrast to the lateral point. Nevertheless, the relatively low H/V value indicates that the torsional mode is comparatively weak

in comparison to the lower modes and some higher modes, which are represented by maxima in the higher part of the spectrum and have not been further investigated.

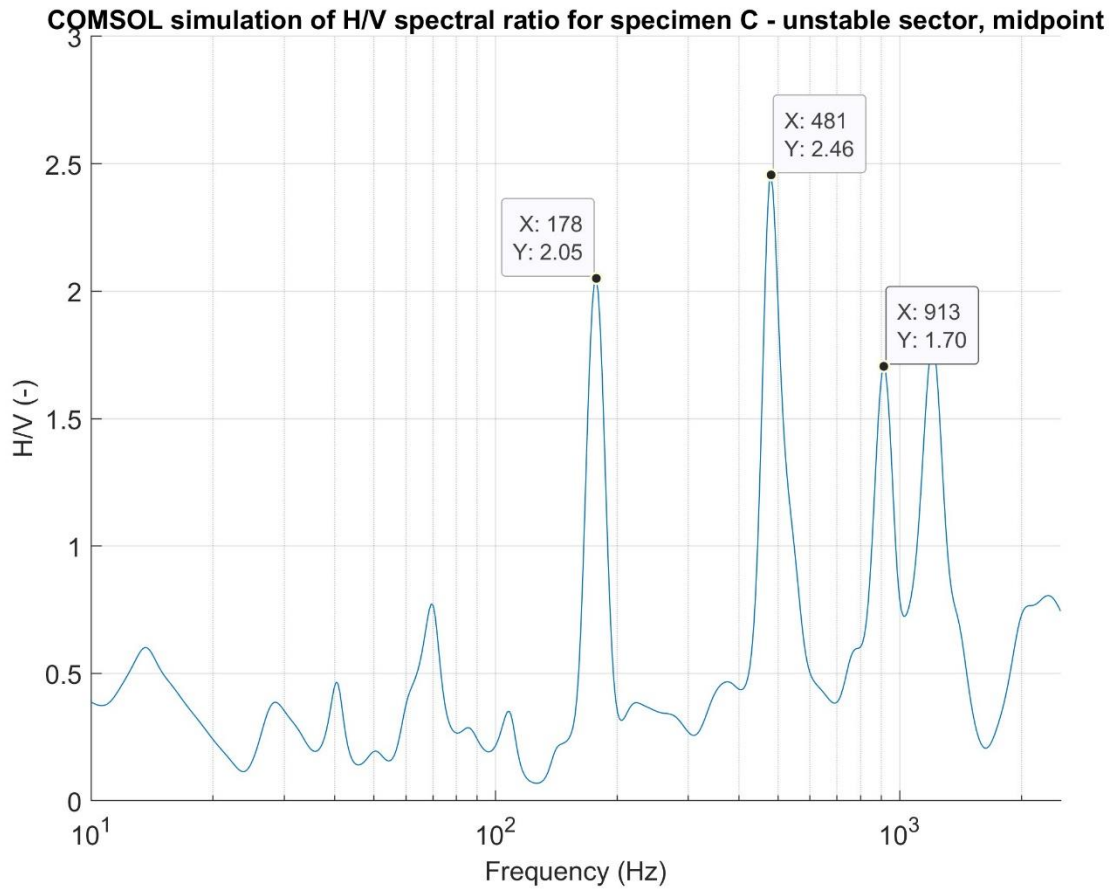


Figure 3.41 H/V simulation for Specimen C4 (unstable sector, midpoint) obtained with COMSOL Multiphysics.

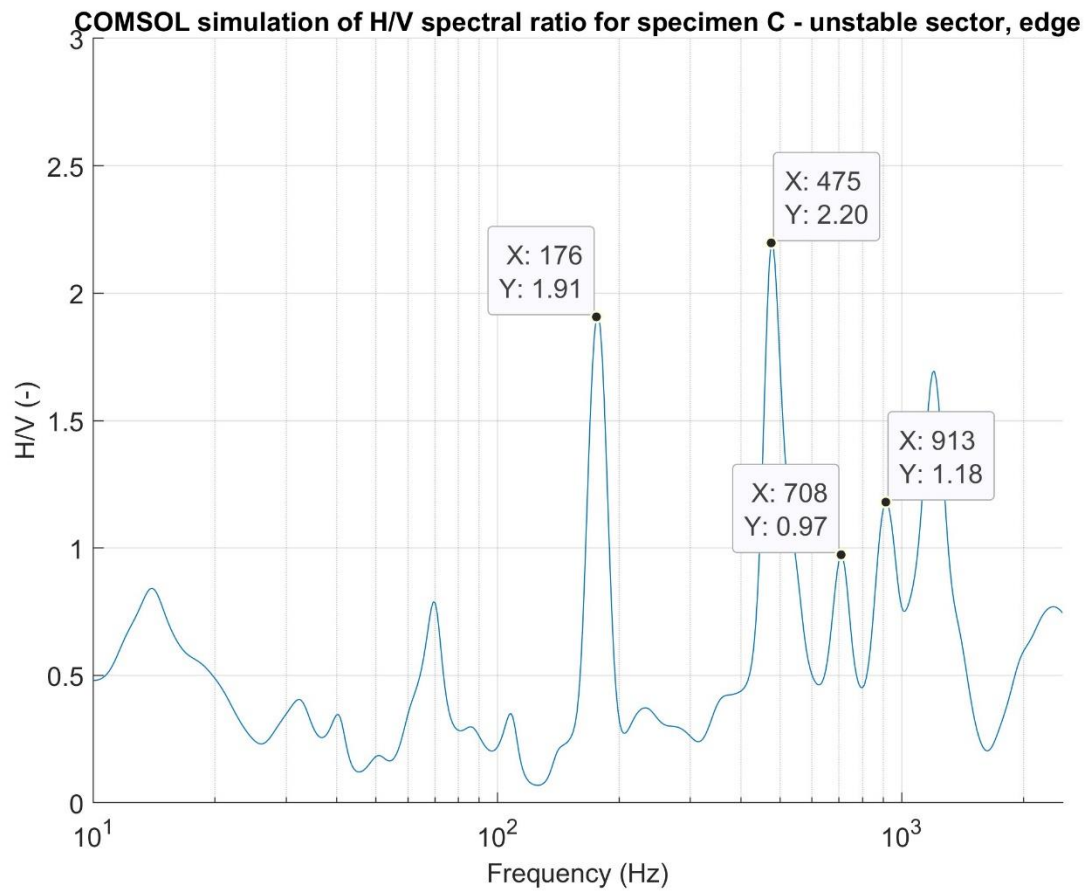


Figure 3.42 H/V simulation for Specimen C4 (unstable sector, edge) obtained with COMSOL Multiphysics.

4 FIELD SCALE ACTIVITY

4.1 The Acuto field laboratory

The Research Center for Geological Risks (CERI) at Sapienza University of Rome established the Acuto Field Laboratory (AcutoFieldLab) within an unstable quarry wall in the Acuto municipality (Figure 4.1), approximately 100 km southeast of Rome. The disused quarry is situated on the western part of the Mt. Simbruini–Ernici ridge, featuring a sedimentary sequence of Mesozoic limestone that has been extensively fractured due to both compressive and extensional tectonic processes involved in the development of the Central Apennines (Grechi et al. 2021). The unstable quarry face, which extends nearly 500 meters in length and reaches heights of up to 50 meters, faces N20°E (Grechi et al. 2021) and was heavily mined until the late 1970s (D’Angiò et al. 2021). This location was selected in late 2015 as an optimal site for establishing a field laboratory to investigate the impacts of human activities and natural forces on extensively jointed rock masses (Grechi et al. 2021). As part of the *THEROCKLAB* PRIN initiative, the quarry site offers the potential to conduct full-scale field tests under controlled conditions as part of future research.

A protruding rock block separated from the rock wall by a subvertical open joint was identified as the optimal site for deploying a multisensory and multiparametric monitoring system.

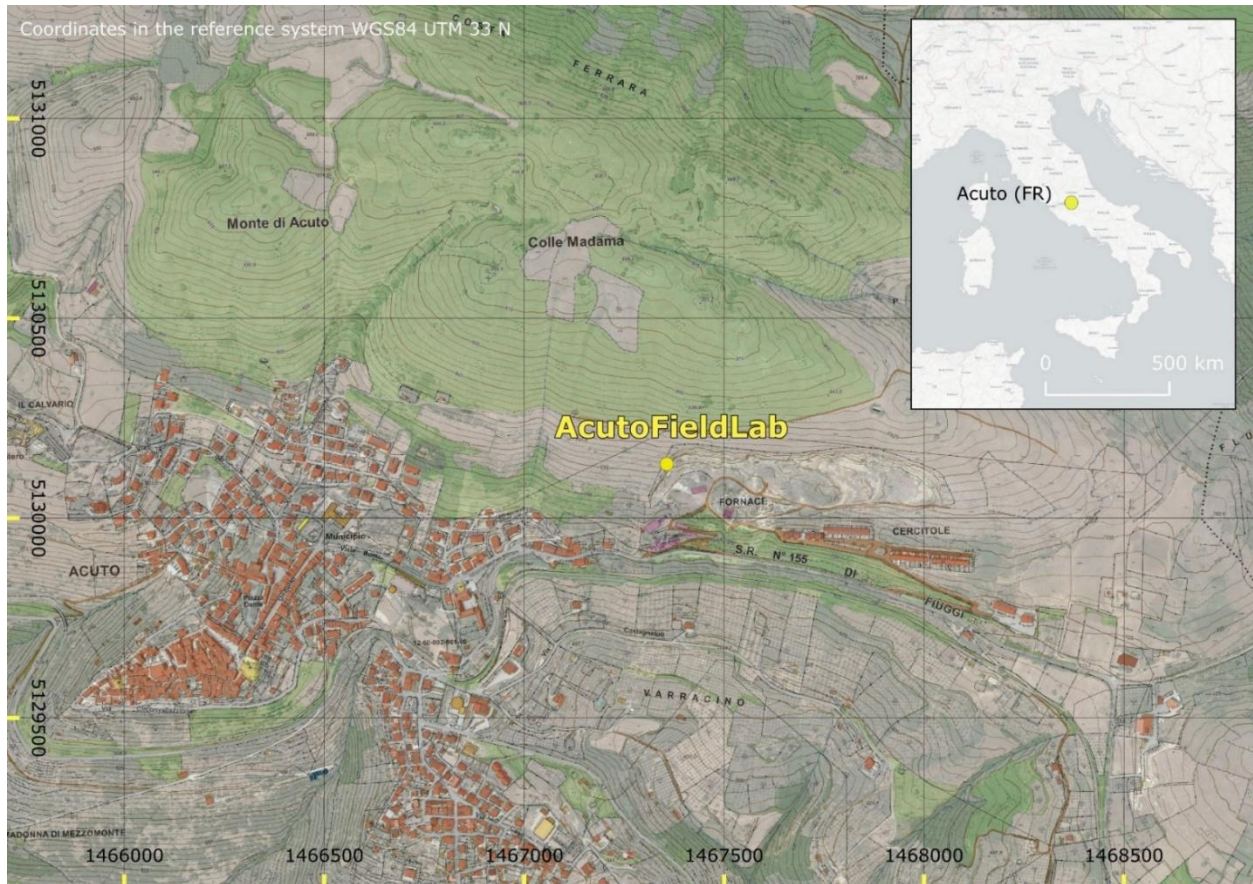


Figure 4.1 AcutoFieldLab geographic location.

The system comprised the following components (Fiorucci et al. 2020):

- A weather station situated on the exterior of the wall, comprising an air thermometer, hygrometer, rain gauge, and anemometer for the measurement of wind speed and direction.
- A Type-K thermocouple, inserted 8 cm into the rock mass to monitor temperature.
- Six strain gauges placed on micro-joints of the rock block.
- Four extensometers positioned across open joints.
- An optical camera linked to a custom AI system.

Meteorological, thermal, and strain data were sampled at a rate of one sample per minute and recorded by a digital data logger (D'Angiò et al. 2021). The technical features of the installed devices are showed in Table 4.1 (Fiorucci et al. 2020).

Table 4.1 Technical specifications of the installed monitoring devices

Device	Measuring Range	Precision	Resolution
Air thermometer	-40/+60 °C	±0.1 K	-
Hygrometer	0-100% RH	±0.8% RH	-
Wind Speed	1.5/79 m/s	±1.5 m/s	0.1 m/s
Wind Direction	0-352°	±7°	-
Rain Gauge (<i>standard WMO</i>)	-	±0.2 mm	0.2 mm H ₂ O
Rock thermometer	-30/+100 °C	-	0.1 °C
Strain Gage (1-LY41-50/120)	50 mm (measurement base)	-	1 µstrain
Extensometer	25 mm (measurement base)	-	0.01 mm

For the purpose of ambient seismic noise monitoring, six on-rock mono-axial FBA11 accelerometers from KINEMATRICS (Pasadena, CA 91107, USA) were installed, with three positioned on the rock block and three on the rock wall (Fiorucci et al. 2020). The accelerometers were connected by cables to a KINEMATRICS K2 data logger, which was equipped with a triaxial accelerometer at the slope base recording data continuously at a 250 Hz sampling rate. Table 4.2 provides the designations and characteristics of the installed accelerometers, while Figure 4.2 shows the point cloud of the field site, highlighting the protruding block and the accelerometers' locations.

Table 4.2 Characteristics of the installed accelerometers.

Station	Compartment	Position	Sampling frequency	Nominal frequency
PRT10	Stable	Base of the wall	1053 Hz	10 Hz
PRT45	Stable	Base of the wall	531 Hz	4.5 Hz
SCR45	Stable	Top of the wall	531 Hz	4.5 Hz
TUF10	Unstable	Upper part	1053 Hz	10 Hz
TRU45	Unstable	Upper part	531 Hz	4.5 Hz
TRL45	Unstable	Lower part	531 Hz	4.5 Hz

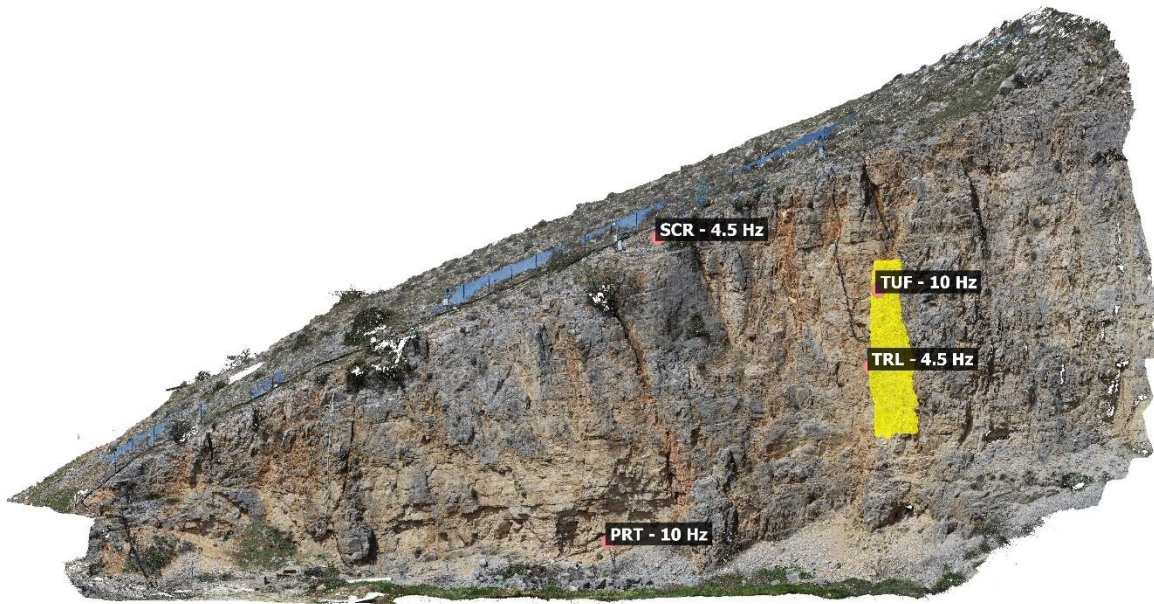


Figure 4.2 AcutoFieldLab 3D point cloud and accelerometers' locations.

4.2 Analysis of the monitoring results

The analysis of the seismic parameters from ambient seismic noise processing was conducted using the data acquired by the stations TUF10 and PRT10 over the period from July 1, 2022, to July 31, 2022. The 10 Hz stations were selected as they exhibited less susceptibility to aliasing phenomena than the 4.5 Hz stations.

The Power Spectral Density (PSD) curves have been calculated for the three spatial directions, encompassing the average PSD over the observation period along with the 10th and 90th percentiles (Figure 4.3). The analysis reveals that the V (vertical) component exhibits a markedly lower responsiveness compared to the horizontal components and is occasionally influenced by spikes (Figure 4.3c).

In the case of the E (East) component (Figure 4.3a), distinct peaks are observed within the frequency ranges of 5-10 Hz and 20-30 Hz, with a particularly sharp peak emerging around 100 Hz. This 100 Hz peak is accompanied by a series of minor peaks located on its ascending left coda, likely indicating the presence of additional local amplifications in the lower frequency bands. Similarly, the N (North) component demonstrates comparable behavior (Figure 4.3b), displaying major peaks within the same frequency ranges as the E component. However, the ascending left coda of the 100 Hz peak in the N component is notably smoother than that observed in the E component.

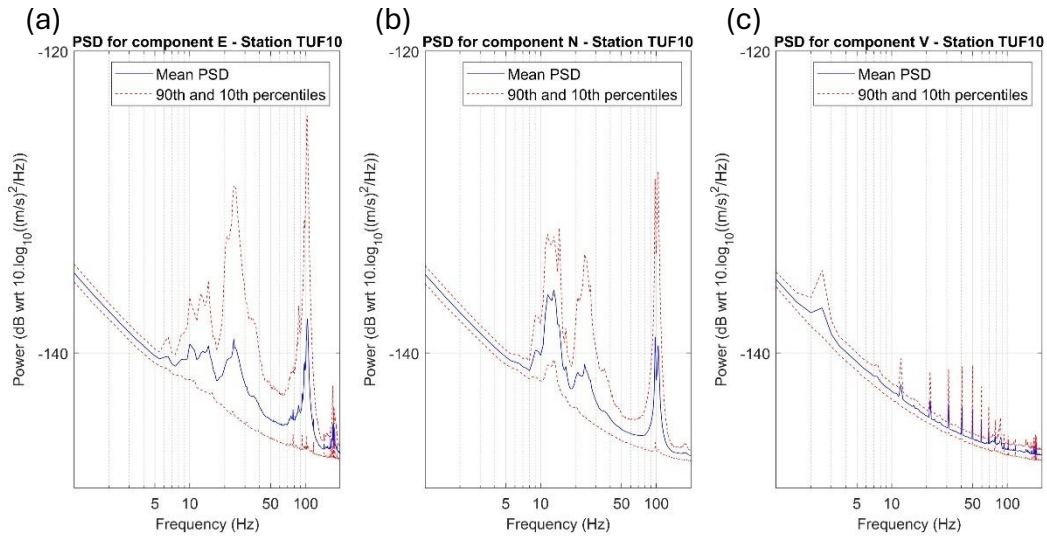


Figure 4.3 Station TUF10 – Power Spectral Density (PSD) curves for component E, N, and V.

Time-frequency spectrograms have been computed for all three components (Figure 4.4). The white areas in the spectrograms indicate the absence of data. Notable reversible variations were observed in the 70-90 Hz range in both the E (Figure 4.4a) and V (Figure 4.4c) components. The observed variations exhibit an oscillatory trend with a daily periodicity.

The horizontal components also exhibit regular daily peaks at approximately 100 Hz. These features are discrete rather than continuous, suggesting that they are unlikely to represent a natural resonance frequency, which is an intrinsic property of the rock mass and therefore continuous in nature. These variations are more likely to be attributable to microseismic-induced microcracks, which are discrete events resulting from thermal expansion due to daily temperature cycles. In addition, the possibility of these bumps being caused by systematic external factors at the monitoring site is ruled out, as they do not appear on the vertical component of TUF10 or on any components of the stable compartment (see Figure 4.10).

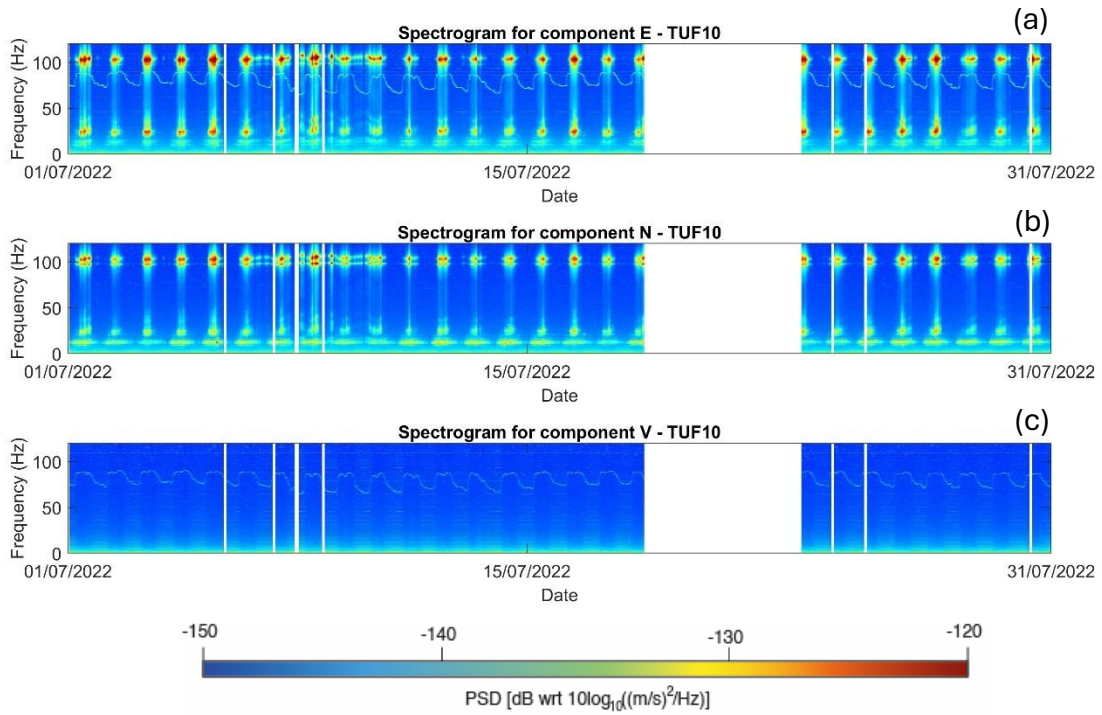


Figure 4.4 Station TUF10 – Spectrograms (E, N, V).

A focused analysis of the spectrogram in the 55-95 Hz range (Figure 4.5) provides a clearer view of the continuous oscillation, which is interpreted as potentially representing the first resonance frequency. It is notable that this first resonance frequency is considerably higher than those reported in the literature for other rock slopes. This discrepancy, however, could be attributable to the relatively limited volume of the unstable sector in comparison to other monitored study sites.

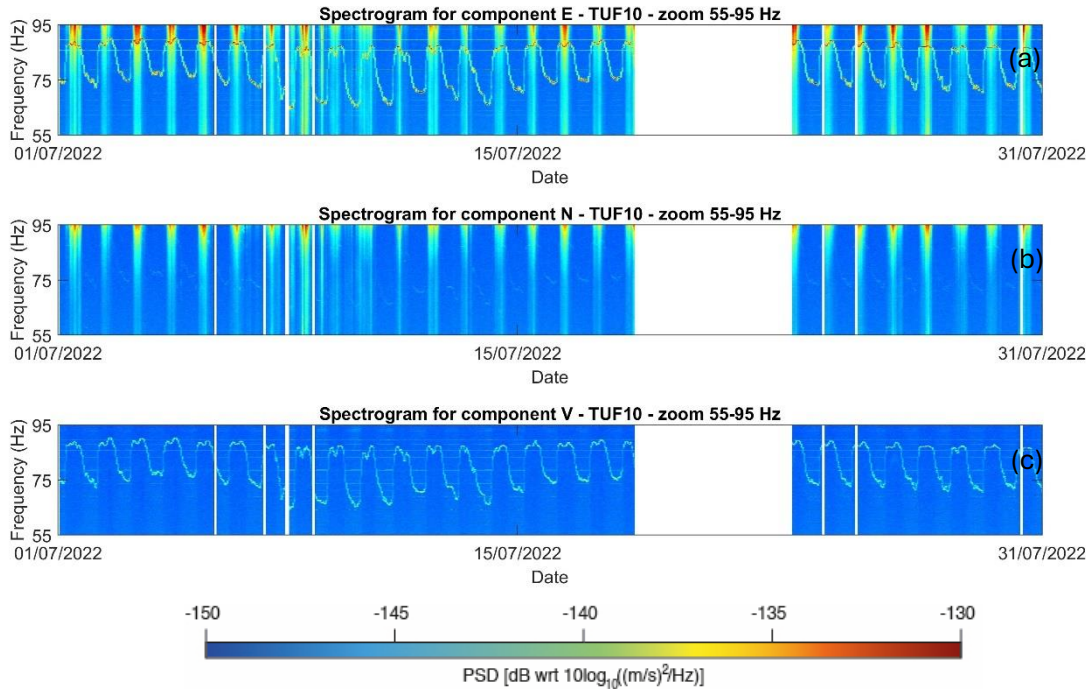


Figure 4.5 Station TUF10 – Spectrograms (E, N, V) zoomed 55-95 Hz

The proposed interpretation of the oscillatory feature detected in the spectrograms as the resonance frequency of the unstable compartment is further substantiated through a comparison with surface rock temperature and microstrain time series (Figure 4.6).

The temperature and microstrains of the rock exhibit an inverse phase relationship (Figure 4.6b). As the temperature rises, the thermal expansion of the rock mass and the closure of microcracks occur, followed by contraction and microcracks opening when the temperature falls.

The frequency oscillation (Figure 4.6a) is perfectly in phase with the rock temperature and in direct opposition to microstrains, with nearly zero lag time. This observation is consistent with expectations derived from the literature, specifically the so-called *fracture effect* and *surface effect*, which describe a positive correlation between temperature and resonance frequency. The thermal expansion of the unstable sector leads to increased contact stiffness, while the differential expansion between the surface and the bulk of the rock increases internal stresses which act

as a confining pressure, enhancing the bulk stiffness of the rock. These mechanisms appear to be more influential than the *bulk effect*, which is characterized by an inverse correlation between temperature and resonance frequency. Although previous studies have indicated that the *bulk effect* typically occurs in smaller volumes, the short period of daily temperature oscillation in this case may prevent the temperature front from penetrating the entire depth of the rock mass.

The in-phase behavior of the frequency oscillation with temperature provides further evidence that the observed oscillation could be interpreted as a reversible variation of the natural resonance frequency of the rock block induced by external factors.

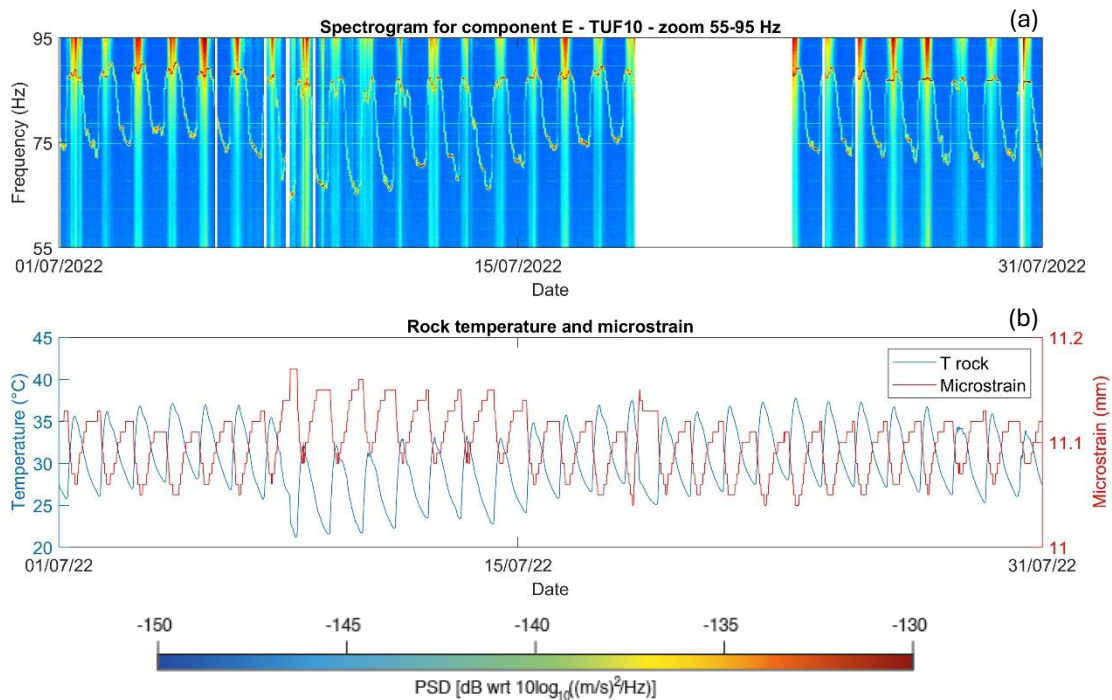


Figure 4.6 Station TUF10 – Spectrogram E zoomed 55-95 Hz and rock temperature/microstrain time series.

The H/V spectrogram is influenced by narrow bands (Figure 4.7), which may obscure the true behavior. Nevertheless, oscillatory behavior, both daily and seasonal, can still be discerned in the spectrograms. However, the considerable

amount of missing data presents a challenge to the accurate interpretation and tracking of these variations.

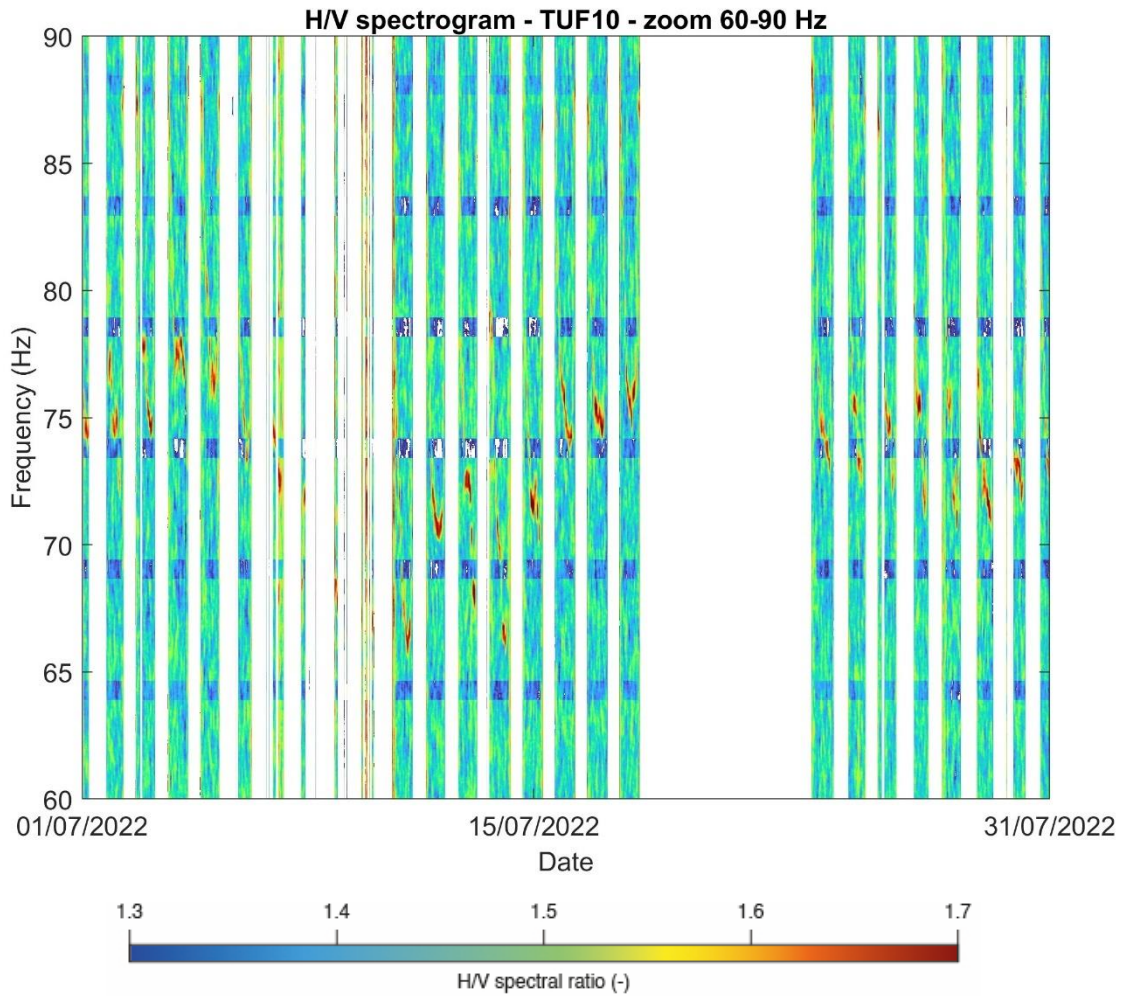


Figure 4.7 Station TUF10 – H/V spectrogram zoomed 60-90 Hz.

Figure 4.8a presents the polar plot computed for TUF10 on the first hour of recording. The radius of the circle indicates frequency (0-90 Hz), while the color bar represents the normalized spectral amplitude. The arrow marks the average azimuth of the maximum average amplitude. A significant maximum is observed at approximately 75 Hz, which is likely indicative of the first eigenfrequency (f_1) of the unstable block. The observed average azimuth is approximately 155° , which

corresponds to the exposure direction of the rock wall, therefore indicating a bending mode perpendicular to the fracture.

Figure 4.8b depicts the azimuth value as a function of frequency. There is a notable densification of points between 150° and 160°, corresponding to the maximum average amplitude at about 75 Hz. Figure 4.8c illustrates the variation of the azimuth of the first detected frequency over the analysis period, showing a pattern that seems to follow the daily reversible oscillation of f_1 .

The perpendicular orientation of the azimuth relative to the fracture plane indicates that this fracture likely governs the behavior of the unstable volume, resulting in a bending mode perpendicular to the fracture. However, the observed frequency fluctuation over time suggests that additional factors influence the resonance behavior. The vibration mode is not purely bending, and it does not occur consistently in the same direction. The observed variation in azimuth is likely the result of the fracture undergoing cyclic opening and closing due to thermal expansion and contraction, which causes shifts in the angle that mirror these cyclic changes. This behavior indicates a slight torsional movement of the tower, which is influenced by the degree to which the fracture is closed at the top.

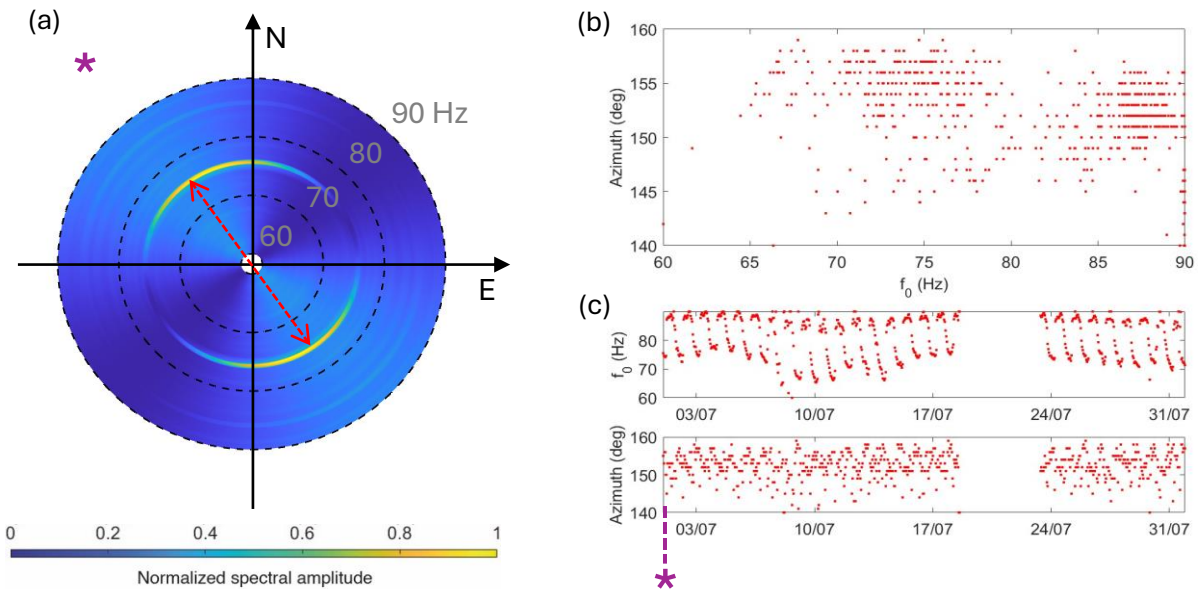


Figure 4.8 Polar plot and azimuth analysis for TUF10.

Analysis of the average PSD of the stable compartment (PRT10) reveals several key observations (Figure 4.9):

- In general, the stable sector exhibits a lower level of responsiveness than the unstable sector across all three components.
- The stable sector exhibits greater responsiveness in the lower part of the spectrum (< 20 Hz) in comparison to the unstable sector.
- Furthermore, the E component appears to be slightly more responsive than the other components.

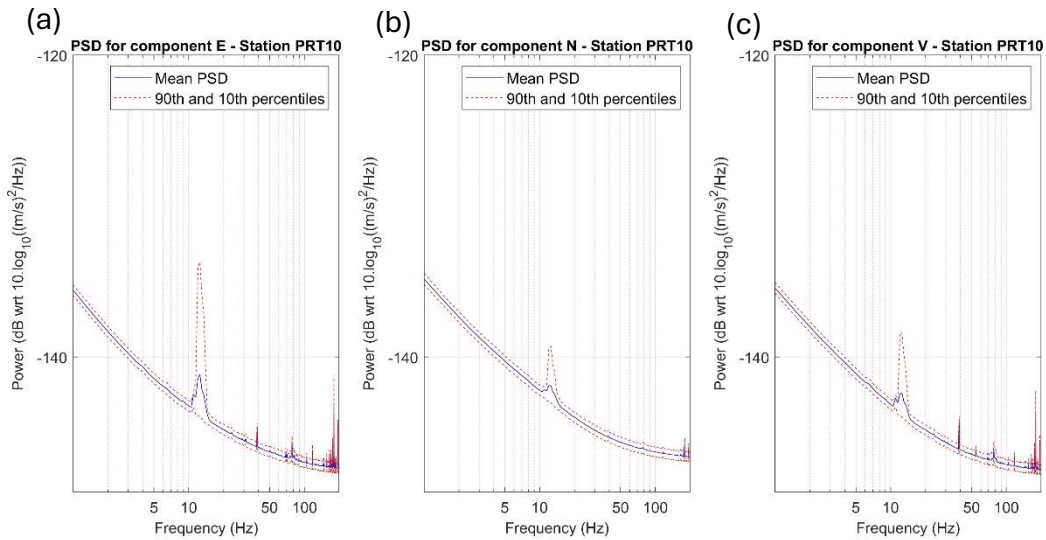


Figure 4.9 Station PRT10 – Power Spectral Density (PSD) curves for component E, N, and V.

The time-frequency spectrograms of PRT10 computed on the 0-120 Hz range (Figure 4.10) appear to provide limited information on the resonant response of the block, in comparison to previous spectrograms. However, a focused analysis within the 55-95 Hz range reveals an oscillatory behavior in both the E (Figure 4.11a) and V (Figure 4.11c) components. This oscillatory behavior is similar to that observed at the TUF10 station, though with significantly lower intensity.

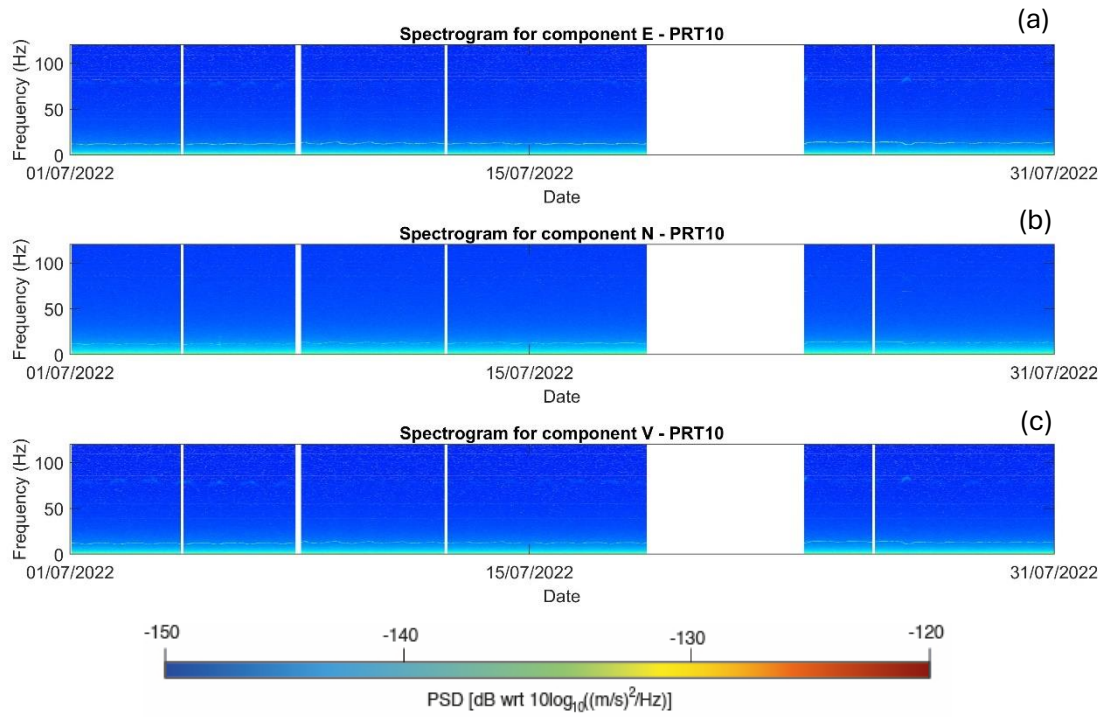


Figure 4.10 Station PRT10 – Spectrograms (E, N, V).

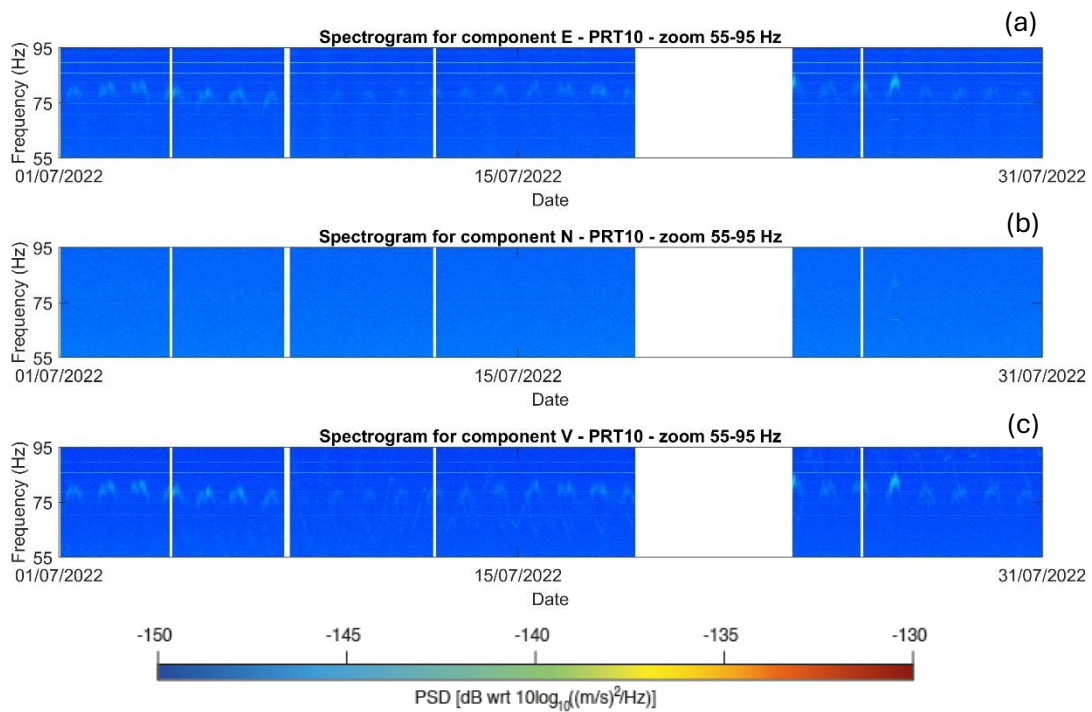


Figure 4.11 Station PRT10 – Spectrograms (E, N, V) zoomed 55-95 Hz.

A more interesting analysis emerges when zooming in on the lower part of the spectrum (Figure 4.12), where the mean PSD suggested a greater response could be found. In this region, a clear, continuous oscillatory behavior can be tracked in the 10-15 Hz range. The continuous and reversible nature of this curve suggests it could be interpreted as the natural resonance frequency of the stable sector. The markedly lower values in comparison to the unstable compartment are in accordance with Eq. 2.1, given that the volume involved is considerably larger than that of the unstable mass.

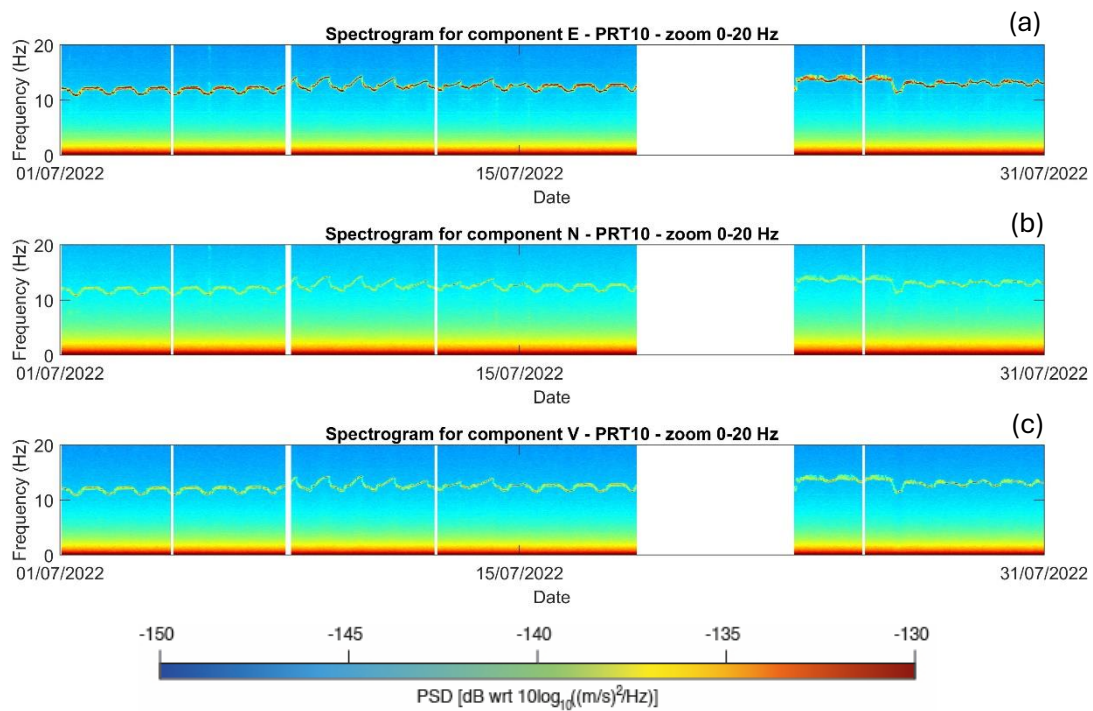


Figure 4.12 Station PRT10 – Spectrograms (E, N, V) zoomed 0-20 Hz.

Further comparison of the oscillation observed at PRT10 with the rock temperature and microstrain time series (Figure 4.13) reaffirms consistency with the theoretical framework, particularly in two aspects: (1) in-phase oscillation with the rock temperature, and (2) opposition of phase with the microstrain.

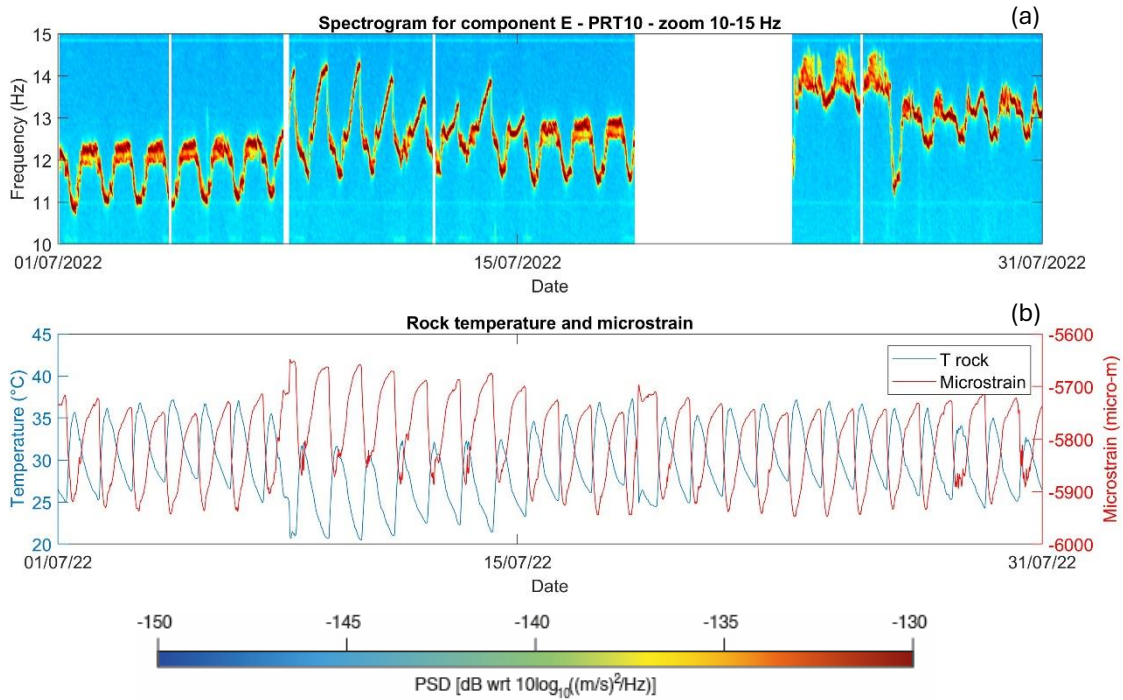


Figure 4.13 Station PRT10 – Spectrogram E zoomed 10-15 Hz and rock temperature/microstrain time series.

The H/V spectrogram for PRT10 has been computed again in the 60-90 Hz range (Figure 4.14), as for TUF10. The following observations can be made:

- An oscillatory phenomenon emerges but, interestingly, with lower H/V values.
- It is possible to observe some aliasing phenomena, with features mirroring the curve, being reflected in a specular way.

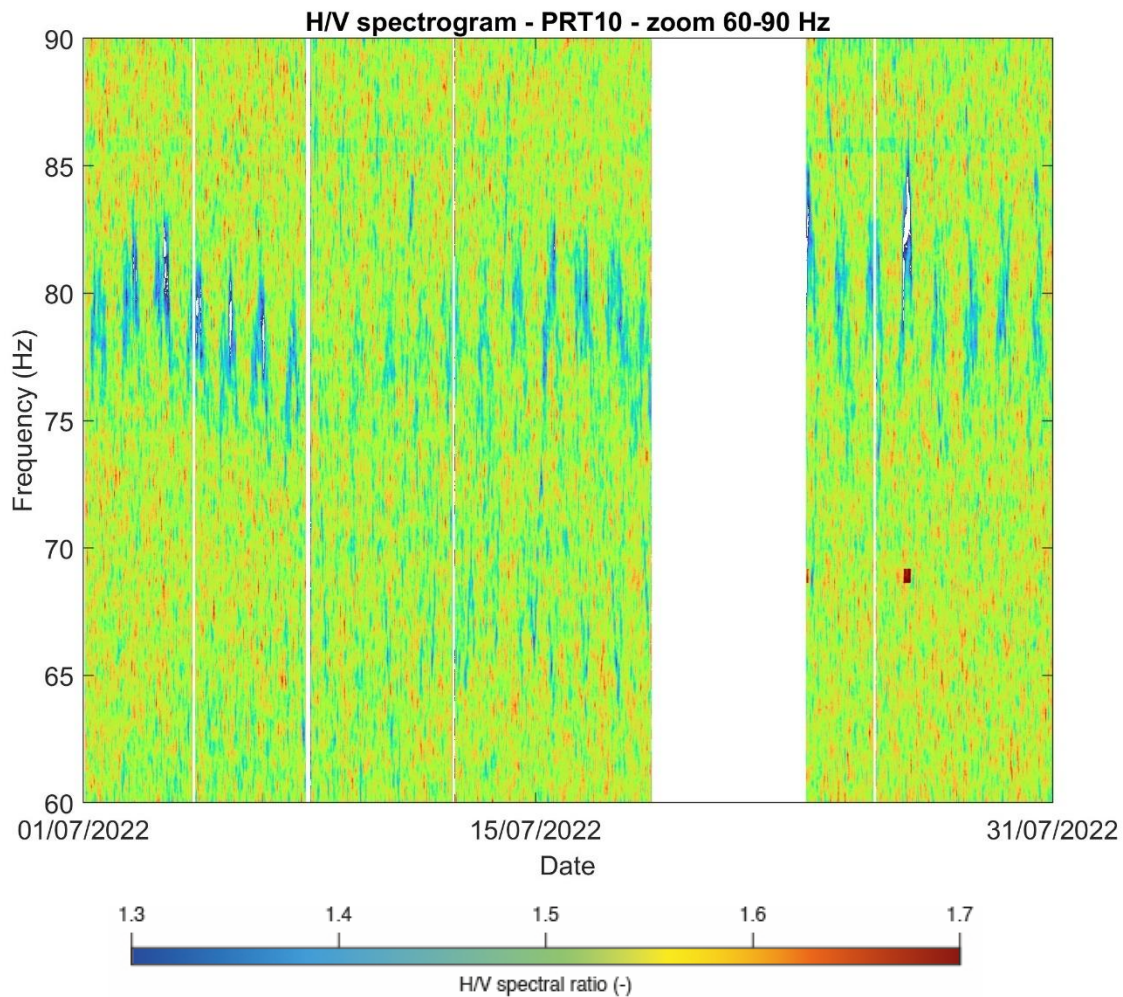


Figure 4.14 Station TUF10 – H/V spectrogram zoomed 60-90 Hz.

Figure 4.15a presents the polar plot computed for PRT10, indicating that the maximum normalized spectral amplitude occurs at approximately 12.5 Hz. This result aligns perfectly with the peak observed in the time-frequency spectrogram for PRT10. Figure 4.15b shows a uniform distribution of azimuths across the analyzed frequency range, without the accumulation observed for TUF10. Additionally, the azimuths span the range of 130-140 Hz, which is slightly lower than the range observed for TUF10. With regard to the temporal behavior of the azimuth, the values for PRT10 remain constant and do not exhibit any cyclic oscillation, as shown in Figure 4.15c. The disparate azimuth values observed for PRT10 in comparison to

TUF10, along with the absence of reversible fluctuations, imply that the protruding block exhibits a distinctive resonant behavior that is separate from that of the surrounding rock wall. This suggests that the resonance behavior of the protruding block is influenced by external factors, particularly temperature, whereas the resonance behavior of the remaining rock wall remains unaffected by these external drivers.

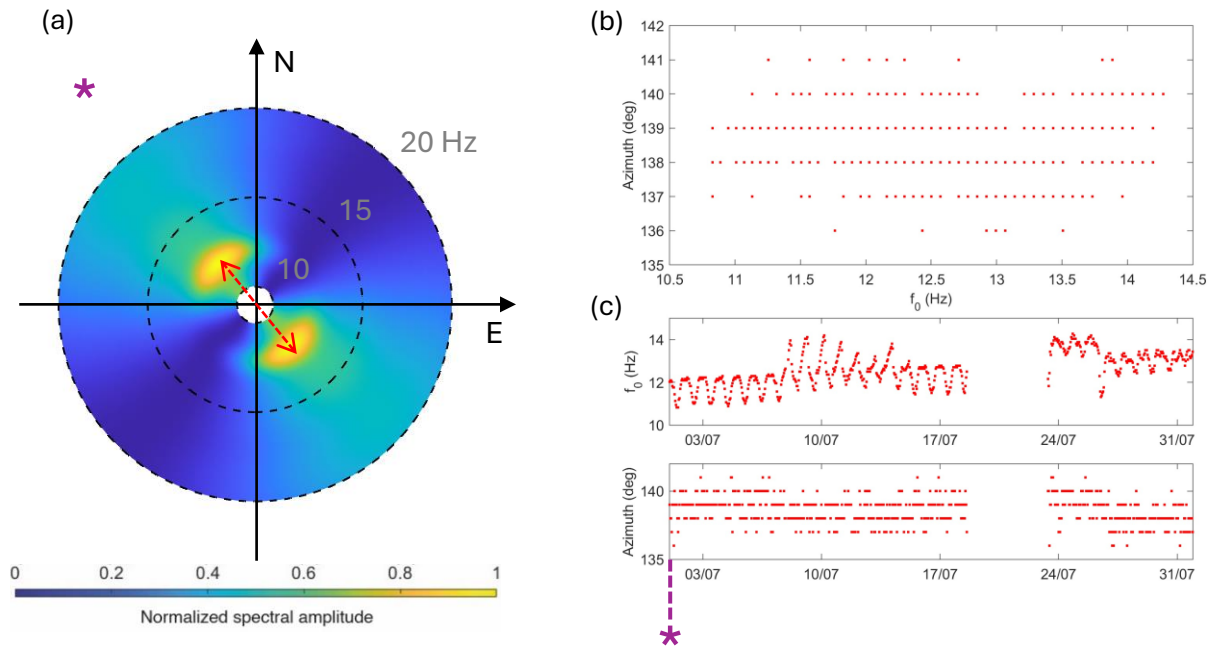


Figure 4.15 Polar plot and azimuth analysis for PRT10.

The results of the cross-correlation analysis of ambient seismic noise and the detection of relative velocity ranges (dV/V) yielded somewhat disappointing findings. Primarily, it is too unstable to compute correlograms within the frequency range of interest, where the first resonance frequency falls (70-90 Hz), while cross-correlation is generally suitable in a cross-correlation range lower than 20 Hz. A correlogram computed within this range would therefore not provide meaningful information due to the significant lack of correlation between sensors situated far apart and would resemble a continuous patch without discernible patterns. Consequently, the cross-

correlogram has been computed within the lower parts of the spectrum, ranging from zero to 20 Hz, divided into 2-Hz windows. Within the 18-20 Hz window, some semblance of coherent oscillatory behavior in the alignment of cross-correlogram peaks and pits becomes discernible over time (Figure 4.16). In addition, the shape of the average cross-correlogram becomes quite symmetrical, as proof of equally distributed noise sources in this frequency range.

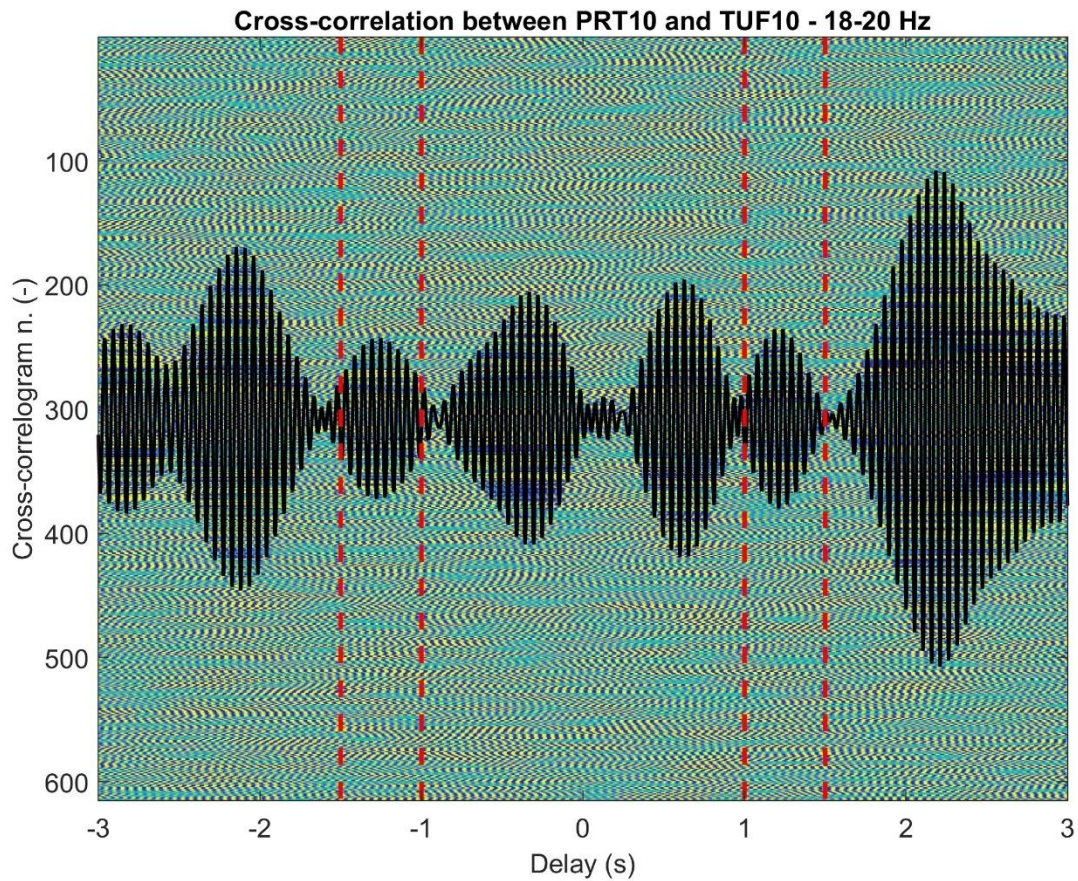


Figure 4.16 Cross-correlogram between PRT10 and TUF10 – 18-20 Hz window.

Following the computation of dV/V values from the cross-correlogram, as elaborated in Section 2.3, it becomes apparent that there is no discernible and coherent oscillatory behavior of the dV/V values corresponding to the daily cycles of rock temperature and microstrain (Figure 4.17). These poor-quality results might be

the effect of the frequency band in which data are analyzed, the long distance between the two stations and the noisy seismic records. In this specific field configuration, the seismic monitoring parameter providing better potential to be tracked over time is therefore the resonance frequency of the unstable tower.

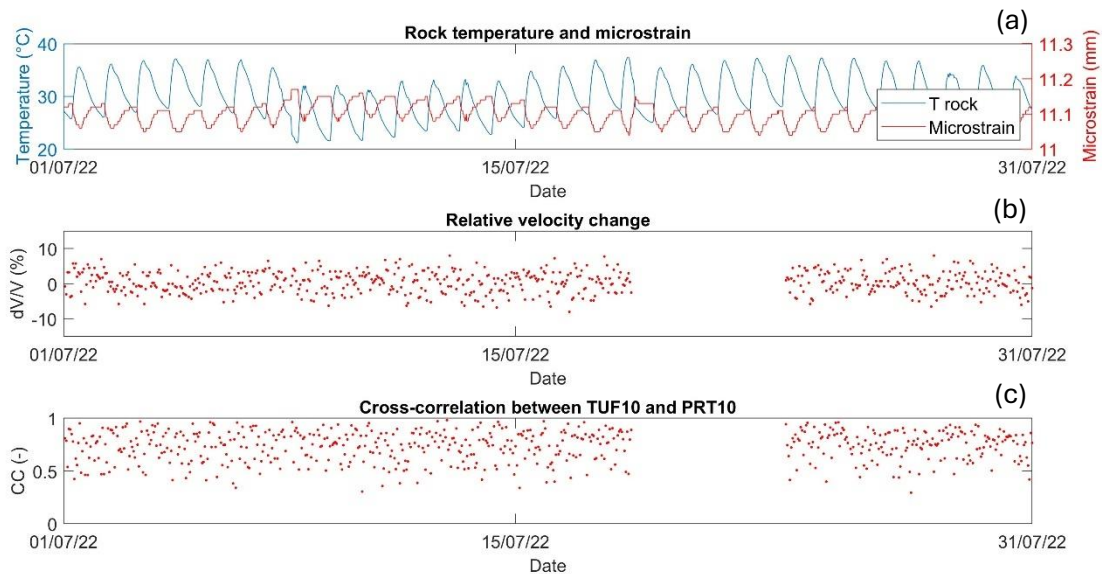


Figure 4.17 Rock temperature and microstrain time series, relative velocity change, and cross-correlation values between PRT10 and TUF10.

A more detailed examination of the data from July 13th to July 18th (Figure 4.18) reveals that, even if a slight cyclical pattern can be discerned, it is extremely challenging to track it accurately and to identify clear similarities with temperature oscillations (Figure 4.19), likely due to the quality of the input data. Consequently, these results further indicate that the pursuit of tracking this seismic parameter should be abandoned, and efforts should be redirected towards analyzing resonance frequency, which have demonstrated more promising results for monitoring objectives.

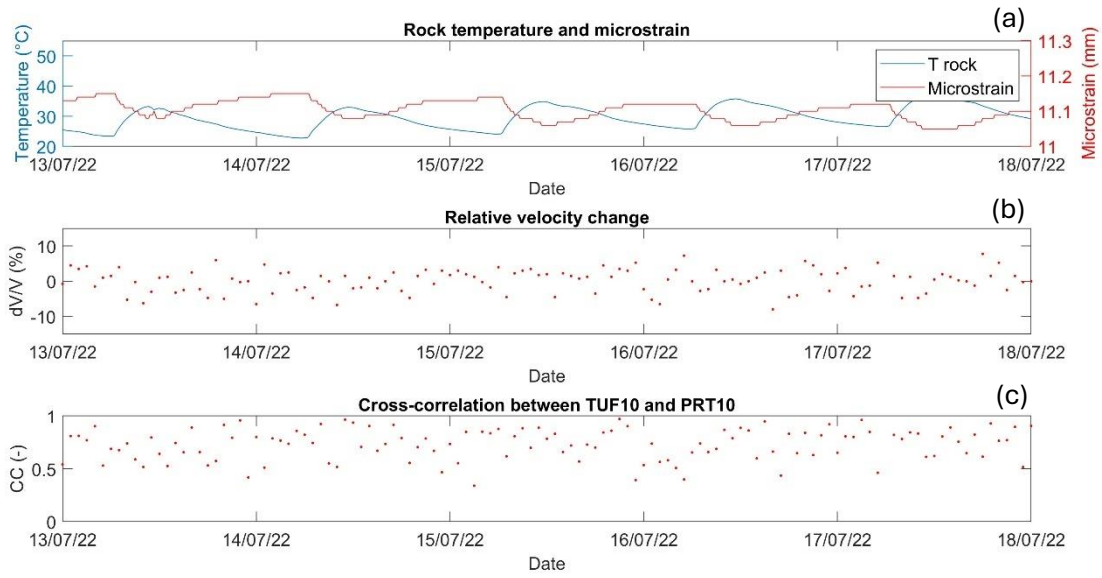


Figure 4.18 Rock temperature and microstrain time series, relative velocity change, and cross-correlation values between PRT10 and TUF10 (zoom 13/07/2022 to 18/07/2022).

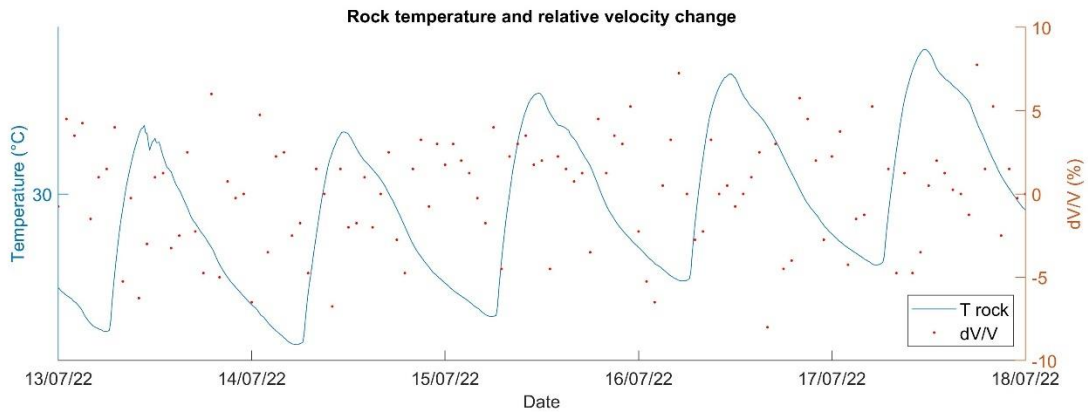


Figure 4.19 Overlap of rock temperature time series and relative velocity change values (zoom 13/07/2022 to 18/07/2022).

4.3 FEM eigenfrequency analysis at the AcutoFieldLab

Following the analysis of field-collected ambient seismic noise data, a finite element method (FEM) eigenfrequency simulation was conducted using GTS NX. This was done to evaluate the feasibility of studying complex geometries through FEM and to compare these results with in-situ measurements.

The Acuto monitoring site was modelled using a point cloud, which was simplified for the purposes of computational efficiency. At the outset, the point cloud of the protruding block was isolated from the remainder of the quarry wall. Subsequently, the surfaces of both the block and the wall were created as discrete entities and extruded to form solid models, resulting in a volume of approximately 62 cubic meters for the unstable protruding tower. For the purposes of this analysis, the Young modulus was set equal to 2 GPa.

The initial simulation attempted an eigenfrequency analysis on the entire rock front geometry. The outcomes were unsatisfactory, exhibiting exceedingly low eigenfrequency values in comparison to those derived from spectral analysis. The software's computation of the resonance frequencies of the entire block presents a challenge, as it makes it impossible to focus solely on the local response of the protruding block. In contrast, site monitoring using accelerometers is based on local acceleration values. Therefore, higher modes were required in this simulation to observe displacements that were solely related to the unstable block, which corresponded to approximately 25 Hz (Figure 4.20).

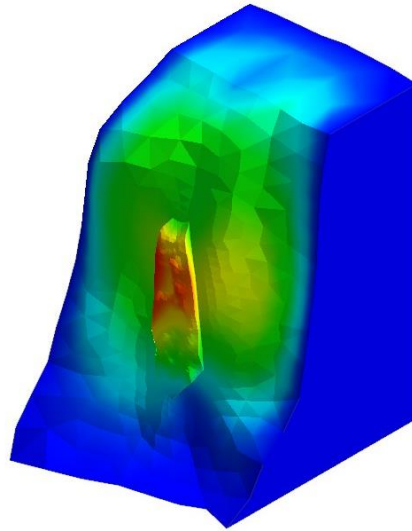


Figure 4.20 Eigenfrequency analysis result for the entire rock wall.

Subsequent simulations were conducted with the isolated protruding block as the sole focus geometry. Initially, a maximum constraint condition was applied, fixing the rear surface to simulate its connection to the rock wall. This resulted in extremely high resonance frequencies, indicating that the actual constraint conditions of the rock portion are significantly weaker than assumed, consistent with prior site characterization identifying a rear subvertical fracture.

A simplified approach was then employed to reproduce the effect of the actual fracture configuration of the unstable block on its resonance response. In this approach, the joint configuration was modeled with a single plane. This entailed progressively isolating larger portions of the block, allowing them to oscillate freely from the remainder of the wall along the rear surface, thereby reducing the fixedly constrained portion.

A simulation conducted with a constrained depth of approximately 11 meters yielded a first resonance frequency of 70 Hz (Figure 4.21), closely matching the value observed in the spectral analysis of monitoring data measured at TUF10. The first resonance mode identified is a bending motion perpendicular to the fracture, in accordance with the azimuth indicated by the polar plot computation (Figure 4.8).



Figure 4.21 Eigenfrequency analysis result for the unstable block only.

5 CONCLUSION

The primary objective of this study has been to enhance the comprehension of the resonance response of unstable rock masses at various scales using passive seismic techniques. This knowledge is intended to facilitate the development of an integrated multisensory system for monitoring and early warning applications as part of a PRIN initiative involving different Italian universities, geographical regions, and fields of expertise.

A notable advancement of this research was the endeavor to apply passive seismic analysis from the field scale to the laboratory scale and to assess the viability of transferring insights acquired at one scale to the other. This approach is of particular importance for the study of the effects of external physical drivers, such as temperature, precipitation, and freeze-thaw cycles, on the mechanical properties and seismic response of rock masses. This is because the laboratory setting environment can potentially allow for more straightforward and controlled experiments. Furthermore, the research investigated the integration of numerical analysis with passive seismic monitoring techniques, with the objective of gaining deeper insights into rock mass behavior, validating experimental results, and guiding the design of laboratory tests.

The methodologies employed in this research included the setup and feasibility study of triaxial seismic recordings on rock samples at the lab scale, spectral analysis of ambient seismic noise collected at field sites, and finite element (FEM) eigenfrequency analysis. The seismic parameters investigated were the natural resonance frequency at both laboratory and field scales and relative velocity change exclusively at the field scale.

Laboratory testing was conducted on two rock specimens of different shapes and materials: a granite column (Specimen A) and a marble slab (Specimen B). The

elastic parameters of the specimens were characterized through the use of ultrasonic pulse velocity (UPV) testing, and photogrammetric techniques were employed for the generation of three-dimensional models for the purpose of volume retrieval.

The laboratory samples were initially modelled using two distinct FEM simulation software packages, GTS NX and COMSOL Multiphysics, and subjected to eigenfrequency analysis. The two software packages yielded comparable results in both eigenfrequency values (with discrepancies as low as 4.2%) and eigenmodes. Specimen A exhibited f_1 values of 480 Hz on GTS NX and 478 Hz on COMSOL Multiphysics, while Specimen B exhibited considerably higher f_1 values, reaching up to 2310 Hz (GTS NX) and 2316 Hz (COMSOL Multiphysics). The first three vibration modes were identified as bending perpendicular to the longer side, bending perpendicular to the shorter side, and torsion around the vertical axis, respectively. The simulation results were processed to obtain the simulated H/V spectral ratio for both specimens, which were measured on the upper face. Both simulations demonstrated an H/V maximum corresponding to the simulated f_1 value. However, the H/V maximum value for Specimen A was approximately twice that of Specimen B, indicating that a column-shaped rock block exhibits a higher resonance response and a more easily discernible resonance frequency.

The simulated eigenfrequency values were employed as references to facilitate the interpretation of the lab seismic recordings. A total of 68 tests of seismic recording at the lab scale were conducted, comprising both active and passive trials with a variety of sensor configurations. The amplitude spectrum and H/V plot analyses identified a consistent noise phenomenon in the frequency ranges of 1900-2400 Hz and 3900-4400 Hz across all tests. Following several attempts to identify the cause of these artifacts, it was concluded that they were most likely due to instrumental noise. Replacing the BNC cables did not eliminate the systematic noise, but it did standardize the noise level across the three components, eliminating any peaks or dips in the H/V plots. However, the interpretation of tests conducted on

Specimen B was significantly affected by the fact that its simulated f_1 value fell within the noise range. In the case of Specimen A, the triaxial seismic recordings demonstrated the difficulty of correctly identifying potential resonance frequencies due to the presence of other relative maxima in the H/V plot. Nevertheless, some tests exhibited a discernible maximum around the anticipated simulated f_1 . In conclusion, the lab triaxial seismic tests on Specimens A and B, in conjunction with numerical simulations, indicate that a column-like rock sample of approximately the dimensions of Specimen A is preferable for tracking eigenfrequency at the laboratory scale due to its enhanced resonant behavior and positioning outside the noise range. Moreover, they suggest that the analysis should be limited to the first eigenfrequency, while higher modes do not show any possibility of being investigated, at least at the laboratory scale.

The second phase of the numerical modeling activity at the laboratory scale examined the impact of a cut in a rock sample on its resonance behavior. Two initial intact geometries were selected for analysis: a column and a slab, both with two sides of equal length. The specimens were designated as Specimen C (10x10x30 cm³) and Specimen D (40x10x30 cm³), respectively. This configuration permitted the implementation of a systematic methodology, enabling the application of a 5 mm thick section inclined at 30° with increasing length while consistently isolating the same unstable volume for both specimens. Four cut lengths and two constraint modes were subjected to testing using GTS NX. The eigenfrequency results showed that as the cut length increased, the discrepancy in frequency values between the two specimens decreased. This trend can be attributed to the resonance behavior increasingly focusing on the unstable section, which remained identical for both specimens, thereby minimizing the influence of their differing overall geometries. Moreover, the frequency values demonstrate a consistent inverse proportionality to the oscillating volume, in accordance with the theoretical framework of the simple oscillator. Furthermore, the study indicated that higher constraint conditions were associated with markedly elevated frequency values. These findings were

instrumental in informing the design of rock samples for future investigations within the PRIN project. Specimen C, with a maximum cut length of 15.1 cm, was identified as the optimal specimen for further analysis and designated as Specimen C4. This specimen exhibited distinct bending (f_1) and torsion (f_4) modes exclusively within the unstable section, consistently producing frequency values well beyond the range of consistent instrumental noise identified in 3C seismic tests. Moreover, its smaller dimensions compared to Specimen D facilitated enhanced manageability and mobility in laboratory settings. Further validation of this identified design through eigenfrequency analyses using COMSOL Multiphysics indicated a minor discrepancy of 13.4% for f_1 between the software packages, while maintaining full consistency across simulated eigenmodes. H/V numerical simulations revealed a clear peak corresponding to the first bending mode but did not conclusively identify the torsion mode (f_4).

The research activity at the field scale involved spectral analyses of the ambient seismic noise recorded at the AcutoFieldLab, where two monitoring stations were considered: TUF10, located on the unstable block, and PRT10, located on the stable block.

Spectrograms for TUF10 showed a distinct peak in the 70-90 Hz range, with a clear daily oscillation in phase with temperature. This peak likely represents the first natural frequency of the unstable block, and its in-phase behavior with temperature suggests that the *fracture effect* is the primary driving mechanism. The polar plot for TUF10 showed an average azimuth of approximately 155° corresponding to the 75 Hz peak, indicating a bending mode perpendicular to the posterior fracture plane. In addition, the azimuth values showed oscillatory behavior in phase with temperature, suggesting that thermal expansion-induced fracture opening and closing affects both frequency and vibration direction.

For PRT10, the spectrograms showed a primary peak around 12.5 Hz with a cyclic trend in phase with temperature. The lower f_1 value compared to TUF10 is consistent with the larger volume of the stable rock wall. The vibration direction for

PRT10, coupled with the absence of reversible azimuth variation, confirmed that the protruding unstable block exhibits a distinct resonant behavior influenced by the fracture and external temperature cycles. Cross-correlation analysis did not provide useful information regarding the effect of external drivers due to the complexity and difficulty in interpreting the results.

Field-scale numerical analyses, especially simulations of the entire rock block, were unsatisfactory due to the difficulty of studying the local resonance behavior of the unstable section. However, modeling only the protruding block and the fracture configuration using a simplified approach - consisting of a single fracture allowing a portion of the block to vibrate freely - yielded f_1 values that closely matched the observed values.

In conclusion, the research showed that further extensive passive seismic monitoring and testing is needed to develop an effective approach for this type of analysis. The natural resonance frequency demonstrated its potential as a seismic monitoring parameter for rock mass failure at the field scale. However, further analysis over longer observation periods and different seasons is needed to confirm the hypothesis that the observed maximum is indeed the first resonance frequency of the block. Eigenfrequency analysis can therefore provide valuable insights into the specific local behavior of unstable blocks and the influence of external factors. However, current knowledge of the behavior of this parameter prior to failure is limited and requires further investigation through tests under controlled artificial conditions at both laboratory and field scales. The potential of numerical modeling to simulate thermo-mechanical and hydro-mechanical mechanisms should be further explored.

6 LIST OF REFERENCES

- Bajni, Greta, Corrado A.S. Camera, and Tiziana Apuani. 2021. “Deciphering Meteorological Influencing Factors for Alpine Rockfalls: A Case Study in Aosta Valley.” *Landslides* 18 (10): 3279–98. <https://doi.org/10.1007/s10346-021-01697-3>.
- Barla, Giovanni. 2019. “Impact of Rock Falls on Inhabited Areas.” Paper presented at the *53rd US Rock Mechanics/Geomechanics Symposium, New York, June 23-26, 2019*. <https://www.researchgate.net/publication/332780630>.
- Bottelin, Pierre, Denis Jongmans, Laurent Baillet, Thomas Lebourg, Didier Hantz, Clara Lévy, Olivier Le Roux, et al. 2013. “Spectral Analysis of Prone-to-Fall Rock Compartments Using Ambient Vibrations.” *Journal of Environmental and Engineering Geophysics* 18 (4): 205–17. <https://doi.org/10.2113/JEEG18.4.205>.
- Burjánek, Jan, Valentin Gischig, Jeffrey R. Moore, and Donat Fäh. 2018. “Ambient Vibration Characterization and Monitoring of a Rock Slope Close to Collapse.” *Geophysical Journal International* 212 (1): 297–310. <https://doi.org/10.1093/gji/ggx424>.
- Colombero, Chiara, Laurent Baillet, Cesare Comina, Denis Jongmans, Eric Larose, Johann Valentin, and Sergio Vinciguerra. 2018. “Integration of Ambient Seismic Noise Monitoring, Displacement and Meteorological Measurements to Infer the Temperature-Controlled Long-Term Evolution of a Complex Prone-to-Fall Cliff.” *Geophysical Journal International* 213 (3): 1876–97. <https://doi.org/10.1093/gji/ggy090>.
- Colombero, Chiara, Laurent Baillet, Cesare Comina, Denis Jongmans, and Sergio Vinciguerra. 2017. “Characterization of the 3-D Fracture Setting of an Unstable Rock Mass: From Surface and Seismic Investigations to Numerical Modeling.” *Journal of Geophysical Research: Solid Earth* 122 (8): 6346–66. <https://doi.org/10.1002/2017JB014111>.

- Colombero, Chiara, Cesare Comina, Sergio Vinciguerra, and Philip M. Benson. 2018. "Microseismicity of an Unstable Rock Mass: From Field Monitoring to Laboratory Testing." *Journal of Geophysical Research: Solid Earth* 123 (2): 1673–93. <https://doi.org/10.1002/2017JB014612>.
- Colombero, Chiara, Denis Jongmans, Sylvain Fiolleau, Johann Valentin, Laurent Baillet, and Grégory Bièvre. 2021. "Seismic Noise Parameters as Indicators of Reversible Modifications in Slope Stability: A Review." *Surveys in Geophysics*. Springer Science and Business Media B.V. <https://doi.org/10.1007/s10712-021-09632-w>.
- D'Angiò, Danilo, Andrea Fantini, Matteo Fiorucci, Roberto Iannucci, Luca Lenti, Gian Marco Marmoni, and Salvatore Martino. 2021. "Environmental Forcings and Micro-Seismic Monitoring in a Rock Wall Prone to Fall during the 2018 Buran Winter Storm." *Natural Hazards* 106 (3): 2599–2617. <https://doi.org/10.1007/s11069-021-04556-5>.
- Fiorucci, Matteo, Salvatore Martino, Francesca Bozzano, and Alberto Prestininzi. 2020. "Comparison of Approaches for Data Analysis of Multi-Parametric Monitoring Systems: Insights from the Acuto Test-Site (Central Italy)." *Applied Sciences (Switzerland)* 10 (21): 1–25. <https://doi.org/10.3390/app10217658>.
- Garia, Siddharth, Arnab Kumar Pal, Archana M. Nair, and Karangat Ravi. 2021. "Ultrasonic P Wave Velocity Measurement of Sedimentary Rocks in Laboratory and Its Dependency on Different Parameters by Using Multivariate Regression Analysis." In *Lecture Notes in Civil Engineering*, 116 LNCE:337–49. Springer Science and Business Media Deutschland GmbH. https://doi.org/10.1007/978-981-15-9976-7_30.
- Grechi, Guglielmo, Matteo Fiorucci, Gian Marco Marmoni, and Salvatore Martino. 2021. "3d Thermal Monitoring of Jointed Rock Masses through Infrared Thermography and Photogrammetry." *Remote Sensing* 13 (5): 1–25. <https://doi.org/10.3390/rs13050957>.
- Knoflach, Bettina, Hannah Tussetschläger, Rudolf Sailer, Gertraud Meißl, and Johann Stötter. 2021. "High Mountain Rockfall Dynamics: Rockfall Activity and Runout Assessment under the Aspect of a Changing Cryosphere." *Geografiska Annaler, Series A: Physical Geography* 103 (1): 83–102. <https://doi.org/10.1080/04353676.2020.1864947>.

- Larose, Eric, Simon Carrière, Christophe Voisin, Pierre Bottelin, Laurent Baillet, Philippe Guéguen, Fabian Walter, et al. 2015. "Environmental Seismology: What Can We Learn on Earth Surface Processes with Ambient Noise?" *Journal of Applied Geophysics*. Elsevier. <https://doi.org/10.1016/j.jappgeo.2015.02.001>.
- Lévy, Clara, Laurent Baillet, Denis Jongmans, Philippe Mourot, and Didier Hantz. 2010. "Dynamic Response of the Chamousset Rock Column (Western Alps, France)." *Journal of Geophysical Research: Earth Surface* 115 (4). <https://doi.org/10.1029/2009JF001606>.
- Potts, David M., Lidija Zdravković. 1999. *Finite element analysis in geotechnical engineering, Theory*. London: Thomas Telford.
- Poupinet, Georges, William L. Ellsworth, Julien Fréchet. 1984. "Monitoring velocity variations in the crust using earthquake doublets: an application to the Calaveras fault, California." *Journal of Geophysical Research: Earth Surface* 89 (B7): 5719-31. <https://doi.org/10.1029/JB089iB07p05719>.
- Stoffel, Markus, Daniel G. Trappmann, Mattias I. Coullie, Juan A. Ballesteros Cánovas, and Christophe Corona. 2024. "Rockfall from an Increasingly Unstable Mountain Slope Driven by Climate Warming." *Nature Geoscience* 17 (3): 249-54. <https://doi.org/10.1038/s41561-024-01390-9>.
- Trigila, Alessandro, Carla Iadanza, Barbara Lastoria, Martina Bussetini, and Angela Barbano. 2021. "Dissesto Idrogeologico in Italia: Perciolarità e Indicatori Di Rischio."
- Valentin, Johann, Alexandre Capron, Denis Jongmans, Laurent Baillet, Pierre Bottelin, Frédéric Donze, Eric Larose, and Anne Mangeney. 2017. "The Dynamic Response of Prone-to-Fall Columns to Ambient Vibrations: Comparison between Measurements and Numerical Modelling." *Geophysical Journal International* 208 (2): 1058-76. <https://doi.org/10.1093/gji/ggw440>.
- Xia, Yong, You Lin Xu, Ze Long Wei, Hong Ping Zhu, and Xiao Qing Zhou. 2011. "Variation of Structural Vibration Characteristics versus Non-Uniform Temperature Distribution." *Engineering Structures* 33 (1): 146-53. <https://doi.org/10.1016/j.engstruct.2010.09.027>.